

Universiteit
Leiden
The Netherlands

Force sensing and transmission in human induced pluripotent stem-cell-derived pericytes

Iendaltseva, O.

Citation

Iendaltseva, O. (2022, November 15). *Force sensing and transmission in human induced pluripotent stem-cell-derived pericytes*. *Casimir PhD Series*. Retrieved from https://hdl.handle.net/1887/3485923

Version:	Publisher's Version
License:	Licence agreement concerning inclusion of doctoral thesis in the Institutional Repository of the University of Leiden
Downloaded from:	https://hdl.handle.net/1887/3485923

Note: To cite this publication please use the final published version (if applicable).

Force sensing and transmission in human induced pluripotent stem-cell-derived pericytes

PROEFSCHRIFT

ter verkrijging van
de graad van doctor aan de Universiteit Leiden,
op gezag van rector magnificus prof.dr.ir. H.Bijl,
volgens besluit van het college voor promoties
te verdedigen op dinsdag 15 november 2022
klokke 16.15 uur

door

Olga Iendaltseva

geboren te Kharkiv, Oekraine
in 1990

Promotores: Prof. dr. T. Schmidt
Prof. dr. E.H.J. Danen

Promotiecommissie: Prof. dr. E. M. Hol (University Medical Center Utrecht)
Dr. V. V. Orlova (Leiden University Medical Center)
Prof. dr. E. R. Eliel
Prof. dr. B. van de Water
Prof. dr. J. Aarts

©2022 Olga Iendaltseva. All rights reserved.
Cover: Kindly offered artwork of Michael Antonov referring to figure 2.3c of this thesis.

Casimir PhD Series, Delft-Leiden, 2022-29
ISBN 978-90-8593-539-1
An electronic version of this thesis can be found at
https://openaccess.leidenuniv.nl

Het onderzoek beschreven in dit proefschrift is onderdeel van het wetenschappelijke programma van de Nederlandse organisatie voor Wetenschappelijk Onderzoek (NWO).

For Iryna, Alexandr, Pavel, Michael and Leo

Contents

1 Introduction **1**
- 1.1 Pericytes and their functions . . . 2
  - 1.1.1 Morphology of pericytes and location in blood vessels 2
  - 1.1.2 Identification of pericytes . . . 2
  - 1.1.3 Pericyte abundance and functions . . . 3
- 1.2 Pericytes and mechanobiology . . . 4
- 1.3 Pericytes and pathology . . . 7
- 1.4 Outline of this thesis . . . 8

2 Towards capillary basement membrane *in vitro* modeling **15**
- 2.1 Introduction . . . 16
- 2.2 Methods . . . 20
  - 2.2.1 Generation of PDMS flat substrates . . . 20
  - 2.2.2 Patterning of PDMS flat substrates . . . 20
  - 2.2.3 Generation of hPAA hydrogel . . . 22
  - 2.2.4 Generation of PDMS gel . . . 22
  - 2.2.5 hPAA hydrogel and PDMS gel patterning . . . 22
  - 2.2.6 hPAA hydrogel and PDMS gel imaging . . . 23
- 2.3 Results . . . 24
  - 2.3.1 PDMS surface micropatterning . . . 24
  - 2.3.2 PDMS gels micropatterning . . . 25
  - 2.3.3 hPAA gels micropatterning . . . 27
- 2.4 Discussion . . . 29
- 2.5 Appendix . . . 31

3 FN patches as anchoring points for force sensing and transmission in hiPSC-derived PCs **39**
- 3.1 Introduction . . . 41
- 3.2 Methods . . . 42

3.2.1 Cell culture . . . 42
3.2.2 Immunostaining . . . 43
3.2.3 PDMS surface patterning with FN and LM . . . 43
3.2.4 PDMS micropillar array preparation . . . 44
3.2.5 Hydroxy-PAAm gel preparation . . . 44
3.2.6 Microscopy . . . 45
3.2.7 Image analysis . . . 45
3.2.8 Statistical analysis . . . 46
3.3 Results . . . 46
3.3.1 Preferred binding of PCs to FN patches on multilayered substrates. . . . 46
3.3.2 Highest PC spreading is accompanied by lowest force application on FN substrates of intermediate stiffness. . . . 49
3.3.3 A switch in PC cytoskeletal organization on stiff substrates. . . . 52
3.3.4 Suppression of PC spreading on 2D patterned FN substrates of high and low stiffness . . . 54
3.4 Discussion . . . 59
3.5 Apendix . . . 63

4 Insights into the regulation of α-SMA expression in pericytes 75
4.1 Introduction . . . 77
4.2 Methods . . . 79
4.2.1 Cell culture . . . 79
4.2.2 Immunostaining . . . 79
4.2.3 Microscopy . . . 79
4.2.4 Image analysis . . . 80
4.2.5 Statistical analysis . . . 82
4.3 Results . . . 82
4.3.1 α-SMA expression and recruitment to stress fibers quantified by orientation analysis. . . . 82
4.3.2 Changes in α-SMA recruitment to stress fibers of PCs driven by growth factors. . . . 85
4.3.3 Inhibition of the time dependent increase in the α-SMA expression and recruitment to stress fibers in PCs on patterned FN substrates. . . . 89
4.4 Discussion . . . 96

5 Pericyte forces in *in vitro* Hypoxia and Ischemia conditions 103
5.1 Introduction . . . 105
5.2 Methods . . . 107
5.2.1 Cell culture . . . 107
5.2.2 PDMS micropillar array preparation . . . 108
5.2.3 Immunostaining . . . 108
5.2.4 Microscopy . . . 109
5.2.5 Image analysis . . . 109
5.2.6 Preparation of flow channels with encapsulated PDMS micropillar arrays . . . 109
5.2.7 Seeding cells on top of PDMS micropillar arrays inside flow channels . . . 110
5.3 Results . . . 111
5.3.1 Pericyte force generation and spreading in starvation, Hypoxia and Ischemia conditions . . . 111
5.3.2 Micropillar array technology does not allow fast liquid exchange in the area with cells . . . 113
5.3.3 Design of a microfluidic channel to track cellular response in rapidly changing conditions . . . 114
5.3.4 Channel preparation . . . 115
5.3.5 Fluid flow in a microchannel with pillars . . . 119
5.4 Discussion . . . 122
5.5 Apendix . . . 126

General Summary and Discussion 131

Samenvatting 138

Publications 143

Curriculum Vitae 144

Chapter 1

Introduction

abstract

Pericytes, the mural cells of blood microvessels, are important regulators of vascular morphogenesis and function that have been postulated to mechanically control microvascular diameter through as yet unknown mechanisms. Their disfunction has been implicated in several pathologies, including cerebral ischemia, Alzheimer's disease and diabetic retinopathy.

To reveal mechanisms used by pericytes for mechanical interactions within microvessels we designed models bringing human induced pluripotent stem cell (hiPSC)-derived pericytes in contact with various micropatterned substrates representing the microvascular basement membrane organization. Our findings shed light on how pericytes can mechanically regulate microvascular morphogenesis and function, and open possibilities for testing therapeutic strategies.

1.1 Pericytes and their functions

In 1873 the French scientist Charles-Marie Benjamin Rouget described a subset of contractile cells surrounding microvessels [1]. These cells were called "Rouget cells" until Zimmerman introduced the term "pericytes" in 1923 to connect to their close location to the endothelial cells (ECs) that form vessel tubes [2]. The “close location” and more precisely “embedment within the capillary basement membrane (BM)” is currently an accepted definition of mature pericytes [3]. Nevertheless, this definition is efficient only for fully developed vasculature and not applicable during angiogenesis or in some pathologic cases when pericytes tend to separate from capillaries and penetrate the tissue.

1.1.1 Morphology of pericytes and location in blood vessels

In a capillary bed, which consists of arterioles, capillaries and venules, pericytes have been found to be located mainly on pre-capillaries, mid-capillaries and post-capillaries. The morphology of the pericytes depends on their location. Mid-capillary pericytes have long cytoplasmic processes that bridge several endothelial cells. Perpendicularly to these primary branches extend thin, secondary arms that partially encircle the vessel. In contrast, pre- and post-capillary pericytes have a more stellate shape with many branches (Fig. 1.1a) [2, 4].

Pericytes are not just “embedded” within the capillary BM, they make a variety of mechanical and biochemical interconnections with ECs. Among them are: peg-and-socket contacts for direct cell signaling and communication, cell-to-cell adhesions by N-cadherins, and integrin-mediated binding of pericytes and ECs to the BM of capillaries, as featured in chapter 2 and chapter 3 (Fig. 1.1b) [5–8].

1.1.2 Identification of pericytes

So far, no single pericyte-specific molecular marker have been identified. Markers that are currently used to identify pericytes are also expressed by other cell types and/or can change their expression levels depending on external factors such as: pathological conditions, development and *in vitro* culturing [5, 10, 11]. Among validated pericyte markers are: PDGFR-β (platelet-derived growth factor receptor-beta), NG2 (chondroitin sulfate proteoglycan 4), CD13 (alanyl (membrane)

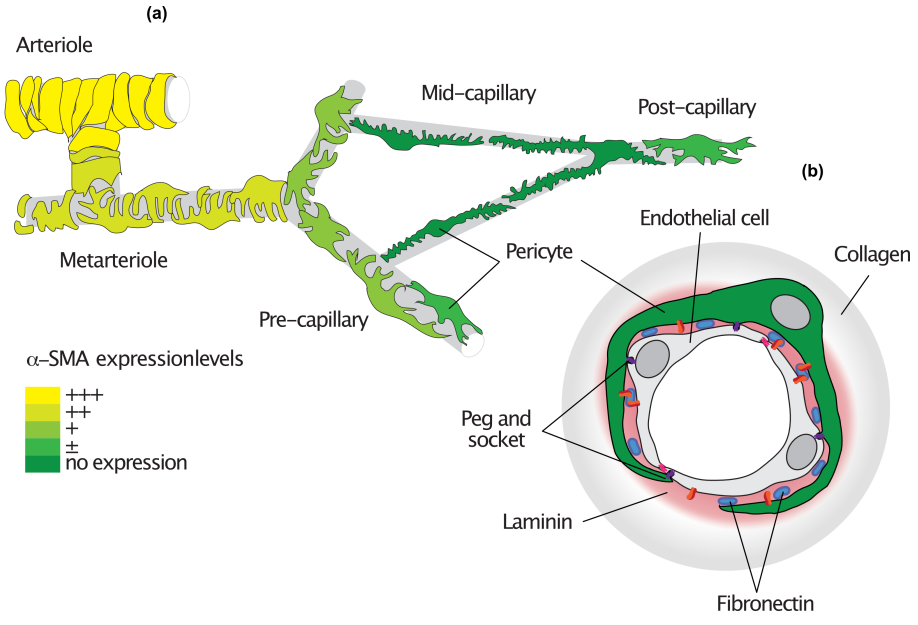


Figure 1.1: Schematic representation of the capillary basement membrane (BM). Laminin-411/511 and Collagen IV are main components that form two layers [9]. Fibronectin deposits are embedded into the Laminin part of the BM and situated in the pericyte-endothelial cell interstitia.

aminopeptidase), αSMA (alpha-smooth muscle actin), Desmin [4, 5, 10, 12].

Pericytes are frequently confused with their close neighbors – vascular smooth muscle cells (vSMCs). These also feature periendothelial location and share a vast majority of molecular markers with pericytes. Absence of specific markers, morphological heterogeneity of pericytes and a smooth transition from the pericyte phenotype to vSMCs, discussed in chapter 4, adds to the challenge of pericyte identification [4, 10, 13]. Currently, pericyte identification depends on a combination of a few factors: location on the capillary tree, morphology, two or more pericyte markers and their ability to support angiogenesis [5, 10, 14].

1.1.3 Pericyte abundance and functions

The density of pericytes and their coverage on capillaries varies across the human body. In normal tissue, the EC-to-pericyte ratio is between

1:1 to 10:1 and pericytes can cover from 10% to up to 70% of the endothelial abluminal surface [3]. It was observed that the density of pericytes depends on endothelial barrier properties, showing highest pericyte coverage in brain, then in lungs and muscle; and on orthostatic blood pressure with increased pericyte coverage in the lower body parts. Additionally, areas with high EC turnover feature lower pericyte densities.

The distribution of pericytes across the body reflects their functions. In the central nervous system (CNS) pericytes play a critical role in the development, regulation and maintenance of the blood-brain barrier (BBB). During embryo development and angiogenesis they regulate the formation and stability of newly formed microvessels, contribute to and control extracellular matrix protein expression and deposition of BM by ECs. In the mature CNS vasculature, pericytes regulate BBB-specific gene expression in ECs to maintain a high number of tight and adherens junctions between cells, and consequently establish the low level of bulk-flow transcytosis of brain ECs. Pericytes also have been reported to induce polarization and mediate proper attachment of the end-feet of astrocytes surrounding CNS capillaries [12, 15, 16]. Taken together, this explains why in the CNS the highest pericyte coverage has been found among all tissue. The barrier function of pericytes causes their lower concentration in the gas-exchange (lungs), filtration (kidney) and nutrient transport regions of the body [11]. The presence of proteins like actin, the high concentration of myosin, tropomyosin and other motors makes pericytes highly contractile cells [17–20]. In combination with their tendency to position themselves around EC junctions and to cover gaps between ECs, pericytes may provide a mechanical support for microvessel walls, preventing excessive dilation. This correlates directly with an increased concentration of pericytes in regions of high or rapidly-changing [21] blood pressure.

1.2 Pericytes and mechanobiology

Despite extensive studies of pericytes there are still many important unsolved questions regarding their mechanobiology [25]. To start with, pericytes have two states: active and mature. These two states are different in the way pericytes migrate. In their active state, pericyte migration is reminiscent of “escaping” from the vasculature and penetrating the tissue [11, 26] sometimes serving as a leading "tip-cell" for a new

Function	Organ/Process	Details	References
BBB integrity control	CNS	Regulation of tight and adherens junctions & bulk fluid flow transcytosis	[12, 15]
Astrocyte end-feet polarization	CNS	pericytes induce polarization and mediate proper attachment of the astrocyte end-feet surrounding CNS capillaries	[15]
Blood flow regulation and vascular tone maintenance	CNS, mature vasculature	pericytes may dilate and constrict capillaries in response to vasoactive substances and neurotransmitters	[11, 21–23]
Vessel stabilization	Angiogenesis, embryonic vascular development, mature vasculature	Contacts between pericytes and ECs promote EC survival, regulate EC migration, proliferation, differentiation and branching	[10, 12, 24]
Basement membrane (BM) synthesis and deposition	Angiogenesis, embryonic vascular development, mature vasculature	pericytes together with ECs produce and deposit extracellular matrix (ECM) proteins necessary for vascular BM formation	[5]
Participation in immunologic defense	CNS, mature vasculature	pericytes have macrophage-like properties and/or can convert into macrophages. They act as antigen-presenting cells for primed T-lymphocytes and are the first line of defense in the brain	[11, 12]
Contribution to tissue regeneration	Vascular niche	pericytes may represent mesenchymal stem cells, white adipocyte progenitors, muscle stem cells and neural stem cells. They were shown to promote tissue regeneration	[10, 11]

Table 1.1: General functions of pericytes

vessel branch. In that state they retract processes, degrade the BM and penetrate the tissue. This active state is specific for tissue healing and generation. In the mature state, pericytes are tightly located around the vessel, stably built-in to the vessel BM, and develop numerous contacts with ECs. Migration in the mature state is described as "sliding" along the vessel, and spreading across newly formed vessels. Both states can be simultaneously observed during active angiogenesis.

The ECs of protruding vasculature release the protein PDGF-B, attracting PDGFRβ positive pericytes [27–30]. When cells are in close proximity, an initial cell-to-cell contact leads to protein EphrinB2 engagement by EphB membrane receptors. Subsequent EphrinB2 phosphorylation starts a reverse-signaling program promoting cell-to-cell adhesion formation [31, 32].

Let us take a closer look at the cell-to-cell adhesion types that may allow mechanical communication between pericytes and ECs. One of them is mediated by N-cadherins [7]. N-cadherins directly link the cytoskeleton of pericytes with that of ECs, promoting direct mechanotransduction between these two cell types [33]. Yet, it has been shown that with vessel maturation and the formation of a BM, the expression of N-cadherins by ECs is downregulated in favour of VE-cadherin binding between the ECs [34, 35]. The next mechanical type of coupling is represented by peg-and-socket contacts. They are known to contain gap-junctions for direct communication and signaling between pericytes and the ECs [6]. The structure of these insets of pericytes into the cytoplasm of ECs is reminiscent of mechanical hooks, that potentially are established to pull on the ECs [36, 37]. Another type of adhesion dominates in mature vasculature. It involves integrin binding of both cell types to the extracellular matrix of the BM [8]. Pericytes are located within a layered BM between collagen type IV on the outer side and laminin (LM)-411/511 on the pericyte-EC interstitium [9, 38]. Electron microscopy analysis shows that the laminin layer also contains small deposits of fibronectin (FN). These FN deposits are $0.2 - 2\mu m$ wide and occur only between pericytes and ECs. The vast majority of focal adhesions, for both cell types, are formed on top of these FN deposits, suggesting that those FN deposits are the points of mechanotransduction between pericytes and ECs. Nevertheless, mechanotransduction pathways between pericytes and ECs are not fully discovered by now.

One of the most interesting topics related to the mechanobiology of

pericytes is their ability to control vascular blood flow [22, 23, 39–41]. Pericytes have many features that would allow them to fulfill this function. They express contractile proteins that allow them to apply forces on the vessel tube [17–20]. The actin fibers of pericytes are oriented axially in the primary processes and circumferentially in the secondary processes. Taking into account that fiber orientation reflects the main direction of cellular force application, circumferential orientation of the fibers in the secondary processes suits to the idea of a role of pericytes in capillary diameter modulation [42]. Additionally, pericytes are often located at capillary branching points – an ideal place for control and redirection of the blood flow, thus working as a switch [43]. In the CNS pericytes have been shown to be capable to react on neuronal activity, resulting in active relaxation and thereby capillary dilation [39, 41]. How pericytes decrease or increase a vessel lumen by constriction through normal forces, general wall stiffening or thinning by tangential contraction or deformation of the underlying ECs, however remains to be discovered [25].

1.3 Pericytes and pathology

Pericytes play an important role in the microvasculature and, thus, are involved in many pathological conditions [44]. The role of pericytes in pathology shall be divided between pathologies: that are caused by deficient pericytes, and those that are caused by impairment of the functions of healthy pericytes due to other factors.

The first group is relatively small, as deficient pericytes usually result in death already during embryo development due to deficient vessels and hemorrhages [12]. The second group includes, for instance, diabetic retinopathy, diabetic nephropathy, diabetic neuropathy and diabetes related erectile dysfunction. These diseases are partially caused by pericytes vulnerability to uncontrolled, high glucose levels in patients suffering from diabetes [44].

Another example of pericytes involvement in the pathophysiology is that of ischemia. Myocardial or renal ischemia promote pericytes to contribute to fibrosis and scar formation in heart and kidneys [45, 46]. In cerebral ischemia, pericytes have been shown to enhance brain damage by actively blocking capillaries in response to prior lack of oxygen and glucose supply [39].

Alzheimer disease (AD), one of the main reasons of cognitive decay in elder humans, appears to induce pericyte contraction, followed by the small vessel disease and cerebral blood flow reduction. The conditions of AD further lead to a decreased pericyte vessel coverage and final BBB breakdown. Combination of both factors further accelerates AD progression and dramatic neurodegeneration [47, 48].

In cancer, pericytes are considered to be progenitors of glomus tumor and myopericytoma [49]. Yet, all tumors lead to impaired functions of pericytes and ECs in general, in particular in the tumor proximity. Various conditions may alter the recruitment of pericytes to newly formed tumor vessels, resulting in high or low pericyte coverage of the tumor microvasculature. Both settings lead to either nourishing the cancer cells resulting in aggressive tumor growth, or in intravasation of cancer cells into the bloodstream and formation of metastasis [44].

All together, during the past decade pericytes have been recognized as important players in pathobiology. An accurate identification of the general role of pericytes, their respective signaling programs and their mechanobiology is needed to understand the mechanisms that pericytes play in pathology. Such novel insight may lead to a more on-target treatment in a diverse range of disease.

1.4 Outline of this thesis

To allow the study of pericyte mechanobiology I focused on *in vitro* modelling of the capillary basement membrane (BM) in **chapter 2**. The part of BM in between pericytes and endothelial cells (ECs) supposedly acts as a mediator of the mechanical interaction between these two cell types. To mimic the BM I developed a technique using microcontact printing (μCP) of proteins on surfaces of largely varying stiffness. Thereby I reproduced the BM rigidity-range and it's unique spatial organization of the two main ECM components in the pericyte-endothelium cell interstitium – laminin (LM)-411/511 and fibronectin (FN).

In **chapter 3** I then used the *in vitro* BM-model together with human induced pluripotent stem cell (hiPSC)-derived pericytes on flexible PDMS micropillar arrays. I showed that mid-capillary pericytes indeed preferred FN-plaques, and I was able to demonstrate that these plaques indeed act as sites for exquisite stiffness sensing and regulation of contractile forces and cell spreading. My findings will open opportunities

for testing therapeutic strategies that target the mechanical properties of capillaries in disease.

In **chapter 4** I assessed the mechanical signals that potentially influence α-SMA expression in pericytes. I used the *in vitro* BM-model approach to investigate vessel diameter, BM composition and the effect of stiffness on the α-SMA recruitment to stress fibers in hiPSC-derived pericytes and compared my findings to those for human smooth muscle cells (SMCs). To quantify the results I developed an automatic image analysis. I showed that α-SMA recruitment was mainly affected by the spatial organization of FN and LM, and to a lesser extend to the stiffness or the ECM contact area. Those findings for pericytes significantly differ to those of SMCs, which were more affected by the rigidity and spreading area, rather than by the protein arrangement in the BM.

In **chapter 5** I investigated the opportunity to study the behaviour of pericytes in pathological conditions *in vitro*. I integrated flexible PDMS micropillar arrays into fluid-flow channels to examine mechanoresponse of pericytes to compromised oxygen and/or glucose supply that permits to mimic pathological conditions like hypoxia and ischemia *in vitro*. My approach will allow us to monitor cellular forces simultaneously with morphological changes, and dynamic protein behaviour in rapidly changing conditions of the microenvironment. Such instrumentation will have a broad applicability for potential *in vitro* testing of drugs or treatment strategies in pathological conditions.

Bibliography

[1] Charles Rouget. « Memoire sur le developpement, la structure et les proprietes physiologiques des capillaires sanguins ». In: *Archives Physiol Normale Pathol* 5 (1873), pp. 603–61.

[2] K.W. Zimmermann. « Der feinere bau der blutcapillares ». In: *Z. Anat. Entwickl.* 68 (1923), pp. 3–109.

[3] David E. Sims. « The pericyte–A review ». In: *Tissue and Cell* 18.2 (1986), pp. 153–174. ISSN: 0040-8166.

[4] V Nehls and D Drenckhahn. « Heterogeneity of microvascular pericytes for smooth muscle type alpha-actin. » In: *JCB* 113.1 (1991), pp. 147–154. ISSN: 0021-9525.

[5] Annika Armulik, Alexandra Abramsson and Christer Betsholtz. « Endothelial-pericyte interactions. » In: *Circ. Res.* 97.6 (2005), pp. 512–23. ISSN: 0009-7330.

[6] Katsukuni Fujimoto. « Pericyte-endothelial gap junctions in developing rat cerebral capillaries: A fine structural study ». In: *Anatomical Rec* 242.4 (1995), pp. 562–565. ISSN: 1097-0185.

[7] Emmanuelle Tillet et al. « N-cadherin deficiency impairs pericyte recruitment, and not endothelial differentiation or sprouting, in embryonic stem cell-derived angiogenesis. » In: 310.2 (2005), pp. 392–400. ISSN: 0014-4827.

[8] Amber N Stratman et al. « Pericyte recruitment during vasculogenic tube assembly stimulates endothelial basement membrane matrix formation. » In: *Blood* 114.24 (2009), pp. 5091–101. ISSN: 0006-4971.

[9] Willi Halfter et al. « The bi-functional organization of human basement membranes. » In: *PLoS ONE* 8.7 (2013), e67660. ISSN: 1932-6203.

[10] Annika Armulik, Guillem Genové and Christer Betsholtz. « Pericytes: developmental, physiological, and pathological perspectives, problems, and promises. » In: *Dev. Cell* 21.2 (2011), pp. 193–215. ISSN: 1534-5807.

[11] L Díaz-Flores et al. « Pericytes. Morphofunction, interactions and pathology in a quiescent and activated mesenchymal cell niche. » In: *Histology and histopathology* 24.7 (2009), pp. 909–69. ISSN: 0213-3911.

[12] Ethan A Winkler, Robert D Bell and Berislav V Zlokovic. « Central nervous system pericytes in health and disease ». In: *Nature Neuroscience* 14.11 (2011), pp. 1398–1405. ISSN: 1097-6256.

[13] Roger Grant et al. « Organizational hierarchy and structural diversity of microvascular pericytes in adult mouse cortex ». In: *J Cereb Blood Flow Metabolism* 39.3 (2017), pp. 411–425. ISSN: 0271-678X.

[14] Akhilesh Kumar et al. « Specification and Diversification of Pericytes and Smooth Muscle Cells from Mesenchymoangioblasts ». In: *Cell Reports* 19.9 (2017), pp. 1902–1916. ISSN: 2211-1247.

[15] Annika Armulik et al. « Pericytes regulate the blood-brain barrier. » In: *Nature* 468.7323 (2010), pp. 557–61. ISSN: 0028-0836.

[16] Robert D Bell et al. « Pericytes control key neurovascular functions and neuronal phenotype in the adult brain and during brain aging. » In: *Neuron* 68.3 (2010), pp. 409–27. ISSN: 0896-6273.

[17] YJ Le Beux and J Willemot. « Actin- and myosin-like filaments in rat brain pericytes. » In: *Anat. Rec.* 190.4 (1978), pp. 811–26. ISSN: 0003-276X.

[18] IH Wallow and B Burnside. « Actin filaments in retinal pericytes and endothelial cells. » In: *Invest. Ophthalmol. Vis. Sci.* 19.12 (1980), pp. 1433–41. ISSN: 0146-0404.

[19] NC Joyce, MF Haire and GE Palade. « Contractile proteins in pericytes. I. Immunoperoxidase localization of tropomyosin. » In: *J. Cell Biol.* 100.5 (1985), pp. 1379–86. ISSN: 0021-9525.

[20] NC Joyce, MF Haire and GE Palade. « Contractile proteins in pericytes. II. Immunocytochemical evidence for the presence of two isomyosins in graded concentrations. » In: *J. Cell Biol.* 100.5 (1985), pp. 1387–95. ISSN: 0021-9525.

[21] Guo Yin et al. « The pericyte as a cellular regulator of penile erection and a novel therapeutic target for erectile dysfunction ». In: *Scientific Reports* 5 (2015), p. 10891.

[22] Nicola B Hamilton, David Attwell and Catherine N Hall. « Pericyte-mediated regulation of capillary diameter: a component of neurovascular coupling in health and disease ». In: *Frontiers in neuroenergetics* 2 (2010).

[23] Claire M Peppiatt et al. « Bidirectional control of CNS capillary diameter by pericytes. » In: *Nature* 443.7112 (2006), pp. 700–4. ISSN: 0028-0836.

[24] Konstantin Gaengel et al. « Endothelial-Mural Cell Signaling in Vascular Development and Angiogenesis ». In: *Arteriosclerosis, Thrombosis, and Vascular Biology* 29.5 (2009), pp. 630–638.

[25] Claire A. Dessalles, Avin Babataheri and Abdul I. Barakat. « Pericyte mechanics and mechanobiology ». In: *Journal of Cell Science* 134.6 (2021), jcs240226. ISSN: 0021-9533.

[26] Laura B. Payne et al. « The pericyte microenvironment during vascular development ». In: *Microcirculation* 26.8 (2019), e12554.

[27] M Hellstrom et al. « Role of PDGF-B and PDGFR-beta in recruitment of vascular smooth muscle cells and pericytes during embryonic blood vessel formation in the mouse ». In: *Development* 126.14 (1999), pp. 3047–3055. ISSN: 0950-1991.

[28] Alexandra Abramsson, Per Lindblom and Christer Betsholtz. « Endothelial and nonendothelial sources of PDGF-B regulate pericyte recruitment and influence vascular pattern formation in tumors ». In: *Journal of Clinical Investigation* 112.8 (2003), pp. 1142–1151. ISSN: 0021-9738.

[29] J A Rhodin and H Fujita. « Capillary growth in the mesentery of normal young rats. Intravital video and electron microscope analyses. » In: *Journal of submicroscopic cytology and pathology* 21.1 (1989), pp. 1–34. ISSN: 1122-9497.

[30] Karen K. Hirschi, Stephanie A. Rohovsky and Patricia A. D'Amore. « PDGF, TGF-β, and Heterotypic Cell-Cell Interactions Mediate Endothelial Cell-induced Recruitment of 10T1/2 Cells and Their Differentiation to a Smooth Muscle Fate ». In: *The Journal of Cell Biology* 141.3 (1998), pp. 805–814. ISSN: 0021-9525.

[31] Ombretta Salvucci et al. « EphrinB reverse signaling contributes to endothelial and mural cell assembly into vascular structures ». In: *Blood* 114.8 (2009), pp. 1707–1716. ISSN: 0006-4971.

[32] Ombretta Salvucci and Giovanna Tosato. *Essential Roles of EphB Receptors and EphrinB Ligands in Endothelial Cell Function and Angiogenesis*. Vol. 114. sciencedirect, 2012. ISBN: 9780123865038.

[33] Holger Gerhardt, Hartwig Wolburg and Christoph Redies. « N-cadherin mediates pericytic-endothelial interaction during brain angiogenesis in the chicken ». In: *Dev Dyn* 218.3 (2000), pp. 472–479. ISSN: 1097-0177.

[34] Deana M Ferreri et al. « N-cadherin levels in endothelial cells are regulated by monolayer maturity and p120 availability. » In: 15.4 (2008), pp. 333–49. ISSN: 1541-9061.

[35] H Gerhardt et al. « N-cadherin expression in endothelial cells during early angiogenesis in the eye and brain of the chicken: relation to blood-retina and blood-brain barrier development ». In: *Eur J Neurosci* 11.4 (1999), pp. 1191–1201. ISSN: 1460-9568.

[36] Irwin M Braverman, Jane Sibley and Agnes Keh. « Ultrastructural Analysis of the Endothelial-Pericyte Relationship in Diabetic Cutaneous Vessels ». In: *Journal of Investigative Dermatology* 95.2 (1990), pp. 147–153. ISSN: 0022-202X.

[37] R.A. Caruso et al. « Ultrastructural Descriptions of Pericyte/endothelium Peg-socket Interdigitations in the Microvasculature of Human Gastric Carcinomas ». In: *Anticancer Research* 29.1 (2009), pp. 449–453. ISSN: 0250-7005.

[38] Lema F Yousif, Jacopo Russo and Lydia Sorokin. « Laminin isoforms in endothelial and perivascular basement membranes ». In: 7.1 (2013), p. 101110. ISSN: 1933-6918.

[39] Catherine N Hall et al. « Capillary pericytes regulate cerebral blood flow in health and disease. » In: *Nature* 508.7494 (2014), pp. 55–60. ISSN: 0028-0836.

[40] Robert A Hill et al. « Regional Blood Flow in the Normal and Ischemic Brain Is Controlled by Arteriolar Smooth Muscle Cell Contractility and Not by Capillary Pericytes. » In: *Neuron* 87.1 (2015), pp. 95–110. ISSN: 0896-6273.

[41] Anusha Mishra et al. « Astrocytes mediate neurovascular signaling to capillary pericytes but not to arterioles. » In: *Nat. Neurosci.* 19.12 (2016), pp. 1619–1627. ISSN: 1097-6256.

[42] M. S. Forbes, M. L. Rennels and E. Nelson. « Ultrastructure of pericytes in mouse heart ». In: *American Journal of Anatomy* 149.1 (1977), pp. 47–69.

[43] Albert L. Gonzales et al. « Contractile pericytes determine the direction of blood flow at capillary junctions ». In: *Proceedings of the National Academy of Sciences* 117.43 (2020), pp. 27022–27033. ISSN: 0027-8424.

[44] David Ferland-McCollough et al. « Pericytes, an overlooked player in vascular pathobiology ». In: *Pharmacology & Therapeutics* 171 (2017), pp. 30–42. ISSN: 0163-7258.

[45] Chia-Jen Siao et al. « ProNGF, a cytokine induced after myocardial infarction in humans, targets pericytes to promote microvascular damage and activation ». In: *Journal of Experimental Medicine* 209.12 (Oct. 2012), pp. 2291–2305. ISSN: 0022-1007.

[46] Shuei-Liong Lin et al. « Pericytes and Perivascular Fibroblasts Are the Primary Source of Collagen-Producing Cells in Obstructive Fibrosis of the Kidney ». In: *The American Journal of Pathology* 173.6 (2008), pp. 1617–1627. ISSN: 0002-9440.

[47] Ethan A. Winkler, Abhay P. Sagare and Berislav V. Zlokovic. « The Pericyte: A Forgotten Cell Type with Important Implications for Alzheimer's Disease? » In: *Brain Pathology* 24.4 (2014), pp. 371–386.

[48] Maiko T. Uemura et al. « Brain Microvascular Pericytes in Vascular Cognitive Impairment and Dementia ». In: *Frontiers in Aging Neuroscience* 12 (2020), p. 80. ISSN: 1663-4365.

[49] Vickie Y. Jo and Christopher D.M. Fletcher. « WHO classification of soft tissue tumours: an update based on the 2013 (4th) edition ». In: *Pathology* 46.2 (2014), pp. 95–104. ISSN: 0031-3025.

Chapter 2

Towards capillary basement membrane *in vitro* modeling [1]

abstract

Basement membranes (BMs) represent thin layers of compact, spatially organized extracellular matrix (ECM) proteins that surround most tissues, and align epithelium and vascular endothelium in the body. *In vitro* reconstruction of any organ or tissue that comprises BMs, requires either inclusion of single ECM proteins, formation of the BM ECM scaffold, or development of a system resembling BM functions. Here, we focused on modeling of the capillary BM part that acts as a mediator of mechanical interaction between pericytes (PC) and endothelial cells (ECs). By using 2D ECM modeling techniques, such as protein microcontact printing (μCP) onto surfaces of different stiffness we could mimic the capillary BM rigidity range and unique spatial organization of two main ECM components – laminin (LM)-411/511 and fibronectin (FN). Our system is useful for studying interactions in the PC-EC interstitial layer of the capillary BM and can be expanded to the complete capillary BM model by adding the collagen-rich second layer.

1. This chapter is based on: O. Iendaltseva, V.V. Orlova, C.L. Mummery, E. H. J. Danen and T. Schmidt, Fibronectin Patches as Anchoring Points for Force Sensing and Transmission in Human Induced Pluripotent Stem Cell-Derived Pericytes, published in *Stem Cell Reports*, 2020

2.1 Introduction

Biochemical and spatial organization of extracellular matrix (ECM) proteins, as well as, matrix stiffness have implications for cell behavior [1–3]. It is important to combine all these factors in order to accurately reproduce the cell microenvironment *in vitro*. The capillary basement membrane(BM) has a unique organization of its three main components – collagen IV, laminin-411/511 and fibronectin that are used for attachment of cells in the capillary wall [4–7]. Endothelial cells attach mainly to laminin, for pericytes this is less well understood. Here ,we revised existing approaches in ECM modeling to develop an *in vitro* model of the BM that can be used to study the biochemical and mechanical interaction of vessel cells such as endothelial cells and pericytes with the BM.

There are many properties of a cell's physical environment that can be mimicked to study their influence on the cell's behavior. These include the biochemical composition, stiffness and geometry of the surrounding ECM. In addition, tissue-level mechanical signals such as tissue rigidity that depends on cell density and intercellular forces, or aspects such as shear stress or hydrostatic pressure in blood vessels, or dynamic mechanical loads such the beating heart [3].

Approaches to mimic ECM protein composition and stiffness of different tissues include 2D and 3D substrates and can be roughly divided into four major categories: decellularized matrices, nanofibrous scaffolds, biomimicking gels and arrays of micro- and nano-posts (Table. 2.1) [20]. Here we will briefly describe the main principles.

Tissue decellularization allows obtaining a natural, cell-assembled matrix, which includes all tissue-specific ECM components in a physiologically correct arrangement that cannot be reached by using just pure proteins or synthetic materials [8]. However, composition of such matrices, as well as their stiffness, is not fully known and varies from donor to donor, restricting their usefulness as a preclinical model.

Nanofiber fabrication [9] is focused on the use of only essential ECM components such as collagen, laminin, fibronectin and other fibrous proteins. These proteins can be used directly to create nanofibrous scaffolds or blended with synthetic (usually biodegradable) polymers to compensate for their rapid degradation and low mechanical strength. Electrospinning [10], phase separation [11], self-assembly [12] and other techniques were developed to obtain 2D or 3D nanofibrous scaffolds with a set

Category	Dimen-tions	Strengths	Limitations	Referen-ces
Decellularized matrices	3D	Natural, cell-assembled matrix. Includes all tissue-specific ECM components in a correct arrangement	Composition and mechanical properties are not fully known and vary from donor to donor	[8]
Nanofibrous scaffolds	2D, 3D	ECM scaffolds with defined protein composition, fiber diameter, alignment, length and crosslinking density. Allows obtaining scaffolds of different stiffness	Impossibility to fine tune the spatial organization of ECM proteins. Nanofiber scaffold stiffness dependence on its protein composition and density	[9–12]
Biomimicking gels	2D, 3D	Decouple the effect of ECM stiffness from it's biochemical composition; cell TFM	Gel porosity, which depends on concentration of crosslinker, showing increase in the pore size with decrease in the gel stiffness	[13–16]
Arrays of micro- and nano-posts	2D, 3D	TFM on substrates of different rigidity, independently from substrates-coupled ECM feedback	3D geometry of the array surface or restricted, by the post diameter, cell FAs size	[17–19]

Table 2.1: ECM mimicking approaches

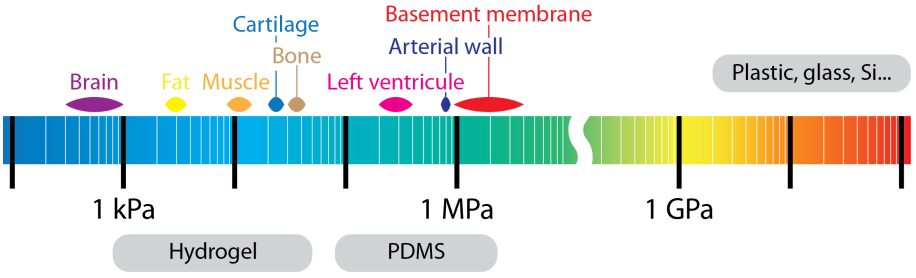


Figure 2.1: Biological rigidity range

fiber diameter, length and crosslinking density that ultimately define the scaffold's resulting stiffness. The main limitations of this approach are the impossibility to fine-tune the spatial organization of ECM proteins and the dependence of the scaffold stiffness on its protein composition and density.

ECM proteins can also be coated on synthetic polymer gels of a certain stiffness to decouple the effect of the biochemical composition and protein density from the matrix stiffness. Polyacrylamide (PAA) [13], hydroxy-polyacrylamide (hPAA)[14] and polydimethylsiloxane (PDMS) [15] gels suit well and are widely used as biomimicking gels for 2D setups. Adding a defined volume of crosslinker while keeping the amount of base polymer unchanged allows to control the rigidity of such gels. PAA and hPAA hydrogels can be prepared in the stiffness range starting from 0.1 kPA, while PDMS gels are mostly used for the higher stiffness like 100 kPA – 1 MPa. Combined use of such polymers embraces the biologically relevant rigidity range of ∼50 Pa – ∼4 GPa (Fig.2.1). Blending marker beads into these gels also allows performing cell traction force microscopy (TFM) [16]. The drawback of such an approach is gel porosity, which depends on the concentration of crosslinker, showing an increase in the pore size with a decrease in the gel stiffness. This influences mechanical feedback from the substrate-coupled ECM in addition to the change in total bulk stiffness of the gel [21].

As an alternative, arrays of Silicone (Si)/PDMS nano- [17, 18] or PDMS micro- [19] posts can be used to measure cell traction forces on substrates of different rigidity, independently from substrate-coupled ECM feedback. Changing the geometry of the posts, but not the amount of crosslinker in the polymer, controls the stiffness of such arrays. Longer posts yield lower rigidity. ECM proteins can be coated on top of the

posts or in between them, depending on the experiment goal, and the rest of the surface is passivated to prevent unspecific cell binding. Nevertheless, this system also has some disadvantages like 3D geometry of the array surface or the restricted cell-ECM attachment area due to the small diameter of the individual posts.

Taken together, all existing systems have their advantages and disadvantages and the experimental approach should be carefully chosen, depending on the cellular process of interest and effects that can be neglected.

As aforementioned, ECM matrix has not only certain mechanical properties and biochemical composition, but in many cases, also a defined spatial organization of proteins. For instance, in the vessel BM, laminin and collagen – it's main components – are not mixed , but located in layers [22]. On the other hand, fibronectin in the BM is located in small patches. To mimic such organiztion, placing proteins in a pattern on top of 2D substrates can serve as a scaffold or a guide for cell shaping and alignment [23].

While micro-scale substrate patterning can shape cells, nano-scale patterning can spatially control subcellular structures. For instance, nano-patterning ECM allows to control the distance between individual ECM-binding receptors such as integrins. This, in turn, affects cell substrate adhesion formation, cell spreading area, and cell proliferation [24].

By combining controlled substrate stiffness and spatial organization of proteins, the various aspects of the BM can be mimicked. Here, we are mainly interested in the impact of the ECM at the cellular scale (i.e. not the nano-scale), and we focus on micro-scale patterning techniques.

Microcontact printing (μCP) was first introduced by George M. Whitesides and Amit Kumar in 1993 [25]. Initially it was developed to obtain patterns of self-assembled monolayers (SAM) on top of a gold film, which with a subsequent selective etching would yield well-defined micrometer sized features of gold. At the base of the technique was an elastomer stamp containing a desired pattern surface texture, covered with SAM and pressed onto a Si wafer with a film of gold on it. This resulted in a transferred pattern of SAM on top of the gold film in places were the surface of gold came in contact with the prominent parts of the stamp. The Si wafer was then etched to produce the desired features. The main advantage of this method was a fast production of gold patterns without clean room or photolithographic equipment.

Further, this principle was adopted for cell biology studies to create patterns of ECM proteins on top of different substrates [23, 26, 27]. In the most utilized approach, an elastomer stamp (mainly made of PDMS) would be covered by a protein of interest and then used to "print" a protein micropattern on top of the activated substrate like PDMS gels, Si wafers, glass, polystyrene dishes or PDMS micropillar arrays of a controlled stiffness [28].

To solve some major problems of μCP, when printing of small, far scattered forms is required, a "stamp-off" method was first applied in the group of Christopher Chen [29]. This method represents an extension of the conventional μCP technique. The difference with convenstional μCP is that the PDMS stamp carrying a patterned surface texture, rather than adding a protein layer to a surface, now is used to remove proteins from the flat surface covered with a protein monolayer at places of contact. This leaves the protein only at areas untouched by the PDMS stamp.

Here, we have combined conventional and stamp-off μCP with PDMS- and hPAA-based substrates of controlled stiffness, to mimic the capillary BM ECM composition, spatial organization, and mechanical properties. The models can be used to study the biochemical and mechanical interaction of vascular cells such as endothelial cells and pericytes with the BM.

2.2 Methods

2.2.1 Generation of PDMS flat substrates

PDMS flat substrates were preparead as following. 20g of PDMS elastomer was mixed in the 1:10 crosslinker:prepolymer ratio, degassed for 1h at 150 pressure and spread onto silanized Si blank wafer. This wafer with PDMS on it was degassed again for 15' and curred at 65°C for 16 hours. After polymerization, PDMS was detached from the Si wafer and cut into 10×10 mm pieces.

2.2.2 Patterning of PDMS flat substrates

PDMS micropillar arrays for stamping were prepared as was described before [30] [31]. Briefly, SI mold was made by two-step Deep Reactive Ion Etching (DRIE) process. This yielded a 10×10 mm hexagonal

array of 2 μm diameter holes with 2 μm spacing and varying depth, flanked by two 50 μm deep 10×2 mm tranches. After mold passivation with trichloro silane (Sigma), PDMS 1:10 was poured over it and cured for 20 hours at 110°C. The peeled off PDMS had a negative of the mold shape with micropillar array and 50 μm spacers on the sides. 50 μm spacers were further cut off to ensure a good contact between the flat surface and pillar array.

A FN-dot pattern on top of PDMS substrates was obtained by using a "microcontact printing" method. First, flat PDMS (Sylgard 184,Dow Corning) 1:30 (crosslinker:prepolymer ratio, cured 16 hours at 65°C) stamps were incubated 60' with a 40 μl drop of 50 μg/ml FN plus 10 μg/ml Alexa405-FN in milliQ, washed ones in milliQ and dried under laminar flow. Then, aforementioned PDMS (Sylgard 184,Dow Corning) 1:10 (crosslinker:prepolymer ratio, cured 20 hours at 110°C) micropillar arrays with spacers cut off were 10' UV-ozone activated and inverted on top of the PDMS stamp for 10'. Further, micropillar arrays with FN on them were pressed onto the UV-ozone activated PDMS substrates surface for 10'. Before removing PDMS micropillar arrays, everything was immersed with 100% Ethanol. After PDMS micropillar arrays were gently detached from the PDMS substrates, 100% Ethanol was replaced, first, with 70% Ethanol and then with 1% BSA 60'at room temperature to block the rest of the surface.

A grid of crossing FN and LM lines pattern on top of the PDMS substrates was obtained by combining "stamp-off" and "microcontact printing" methods [32]. First, two PDMS 1:10 molds with 5 μm high lines of different width were produced by using replica-molding from a silicon wafer. After UV-ozone activation 10', they were pushed onto PDMS 1:30 stamps with a protein layer dried on them. Followed by 10' incubation and removal, this molds left a negative of the pattern in the protein layer on top of the PDMS stamps. Further, PDMS stamps were inverted on top of the UV-ozone activated PDMS 1:10 surface, creating a pattern of crossing LM and FN lines on it (Fig. 2.3a). As a last step, everything was immersed with 100% Ethanol, then 100% Ethanol was replaced, first, with 70% Ethanol and then with 1% BSA for 60' at room temperature to block the rest of the suface.

A pattern on top of PDMS flat 1:10 (crosslinker:prepolymer ratio, cured 16 hours at 65°C) substrates, where LM would surround FN spots or the inverse organization, was produced by combining "stamp-off" and

"microcontact printing" methods [32]. Two flat PDMS (Sylgard 184,Dow Corning) 1:30 (crosslinker:prepolymer ratio, cured 16 hours at 65°C) stamps were separately incubated for 60' with LM-111 (Sigma, l2020) and mixture of Alexa405-labeled and unlabeled FN (Sigma, f1141), washed with milliQ and dried under laminar flow. With a help of UV-ozone activated PDMS 1:10 micropillar arrays, were obtained holes in one of the layers. Further, two stamps were inverted one by one on top of the UV-ozone activated PDMS 1:10 surface and incubated for 10' each, to get previously modified protein sheet on top of the uninterrupted layer of – second (Fig. 2.2a, b).

PDMS surfaces with FN lines under a layer of LM with holes were printed by using PDMS stamps with LM and FN layers modified as aforementioned. A PDMS micropillar array was used to make holes in the dry LM monolayer and PDMS mold with lines – to create a line pattern in FN. Further, this stamps were loaded for 10' each on top of the UV-ozone activated PDMS surface, with FN stamp going first (Fig. 2.3b). Finally, all patterned PDMS surfaces were washed with 100% Ethanol, followed by 70% Ethanol and blocked by using 1% BSA 60'.

2.2.3 Generation of hPAA hydrogel

hPAAm hydrogels were made following a previously described method [14]. Gels stiffer then 40 kPa were obtained following the same procedure as suggested in [33] and [34] by increasing polyacrylamide mono-mer concentration with a fixed monomer/crosslinker ratio of 29:1.

2.2.4 Generation of PDMS gel

PDMS gels were generated similar to the procedure described before. First, 13 mm glass coverslips were cleaned in milliQ and ethanol, dried and treated 10' in the UV-ozone chamber. Then, PDMS (Sylgard 184, Dow Corning) prepolymer was mixed with the crossliker in different ratios from 10:1 to 100:1, degasssed and spread on top of the glass coverslips, followed by curring at 65°C for 16 hours.

2.2.5 hPAA hydrogel and PDMS gel patterning

A pattern on top of hPAA hydrogels and PDMS gels, where LM would surround FN spots was produced by combining "stamp-off" and

"microcontact printing" methods [32]. First, stamps were prepared in the same way for both types of gels. A 40 µl drop of 50 µg/ml LM-111 in milliQ water was incubated for 60' on top of the 10 × 10 mm PDMS (Sylgard 184,Dow Corning) 1:30 (crosslinker:prepolymer ratio, cured 16 hours at 65°C) stamp, followed by washing and drying under laminar flow. Then OV-ozone activated PDMS micropillar array was pushed onto the dry LM-111 monolayer to obtain holes in the places of micropillar-LM-111 contacts. After 10' incubation the array was removed and a second 40 µl drop of 50 µg/ml FN plus 10 µg/ml Alexa405-FN in milliQ was gently spread onto the first layer for 60'. Finally, the stamp was washed and dried under laminar flow.

Hydroxy-PAAm hydrogels were dried using nitrogen flow and incubated with the stamp for 60' (Fig. 2.6a), following blocking with 1% BSA in PBS o/n and washing with PBS.

PDMS gels were 8' OV-ozone activated and incubated with a stamp for 10', following blocking with 1% BSA in PBS or 0.2% Pluronic (F-127, Sigma) in PBS for 60' and washing with PBS.

2.2.6 hPAA hydrogel and PDMS gel imaging

Confocal imaging was performed on a home-built setup based on an Axiovert200 microscope body (Zeiss), spinning disk unit (CSU-X1, Yokogawa) and an emCCD camera (iXon 897, Andor). IQ-software enabled setup-control and data acquisition. Lasers of 405 nm (CrystaLaser), 488 nm (Coherent), 514 nm, 561 nm (Cobolt) and 642 nm (Spectra Physics) wavelength were coupled into the CSU via polarization maintaining single-mode fiber. For PDMS and hPAA 2D assays parafilm spacers were made directly on top of the glass coverslips.This approach ensured reproducible cell observation within the limited working distance of a high-NA objective on an inverted microscope.

2.3 Results

2.3.1 PDMS surface micropatterning

First, to generate a pattern of micron sized spots of FN on a flat surface, which would resemble FN deposits in the capillary BM, we used PDMS micropillar arrays as a stamp for FN dots and several test substrates following microcontact printing technique. Test substrates included PDMS flat surface prepared in the ratio 1:10 crosslinker:base and cured in a polystyrene dish, PDMS flat surface 1:10 cured on a Si blank wafer and glass coverslips. PDMS micropillars had 2 μm diameter, hexagonal order and 2 μm spacing. Stamping was tested using pillar arrays of two different stiffness – 47.2 kPA and 137 kPa. After test surfaces were cleaned and activeted with UV-ozone, micropillar arrays having FN on top of the pillars were pressed into them. Alexa647 FN labeling prior to experiment allowed to examine stamping results with confocal microscope (Supplementary Fig. 2.7). Stamping a PDMS flat surface prepared on a blank Si wafer with 137 kPa stiff micropillar array yielded the most homogeneous and reproducible pattern of FN dots (Supplementary Fig. 2.7e) and this combination was chosen for further experiments. Next, we tested two surface passivation ways to prevent unspecific binding of cells. Stamped PDMS surfaces were incubated for 1 hour with either 1%BSA in PBS or 0.2%Pluronic in PBS, washed and seeded with cells. After 4 hours incubation cells were fixed, stained for F-actin and the average cell spreading area was determined (Supplementary Fig. 2.8). Both approaches showed effective passivation with no difference in effect on cell spreading behavior.

To further introduce LM into the system, a PDMS suface patterned with FN dots was coated or stamped with a thin layer of LM-111 or matrigel. Cells readily attached to substrates, but were not able to sense FN dots (data not shown). To solve this issue a reverse approach was taken. Following "stamp-off" method principles, a PDMS micropillar array was used to make holes in the LM layer, which was further transferred onto a PDMS flat surface stamped with a FN monolayer (Fig. 2.2a). This approach yielded a pattern were FN was exposed through hexagonally ordered 2 μm wide holes in the LM layer (Fig. 2.2c). For the cell adhesion assays an inverse pattern was additionally generated (Fig. 2.2d) where LM was exposed through holes in a FN layer (Fig. 2.2b). Besides this, a pattern of crossing LM and FN lines (Fig. 2.3a, 2.3c) together

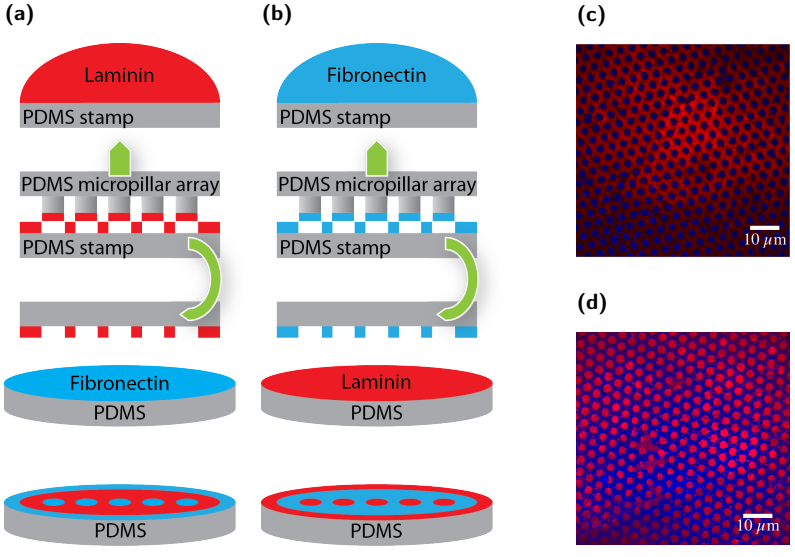


Figure 2.2: (a and b) "micro contact printing" schemes for patterns with: (c) FN spots surrounded by LM-111, (d) LM-111 spots surrounded by FN

with FN lines exposed through holes in LM layer (Fig. 2.3b, 2.3d) were developed using microcontact printing and "stamp-off" techniques.

To investigate whether gel stiffness influences precision of the gel surface patterning and accuracy of patterned features, a pattern steepness was assessed for PDMS and hPAA gels of different rigidity. Pattern steepness of the LM layer with holes and FN/LM lines was determined from an intensity profile (Fig. 2.4). The intensity profile (Fig. 2.4b) was read from the cross section set manually by the line (Fig. 2.4a) and a distance from the 20% peak hight and 80% was determined as pattern steepness Δx (Fig. 2.4b). Pattern containing microholes showed higher steepness than FN/LM crossing lines (Fig. 2.5).

2.3.2 PDMS gels micropatterning

Subsequently, to introduce stiffness into our model we generated PDMS gels of different rigidities by varying the base:crosslinker ratio according to a technology described earlier [21]. Base:crosslinker ratios were taken from 1:10 to 1:100 yielding PDMS gels in a ~2300 kPa –

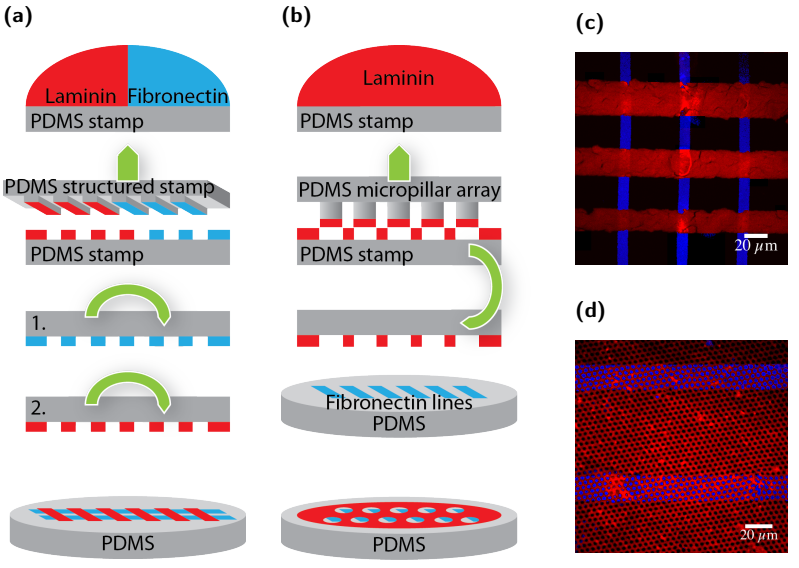


Figure 2.3: (a – b) "micro contact printing" schemes for patterns with: (c) a grid of crossing LM-111 and FN lines, (d). FN lines stamped under a layer of LM-111 with holes.

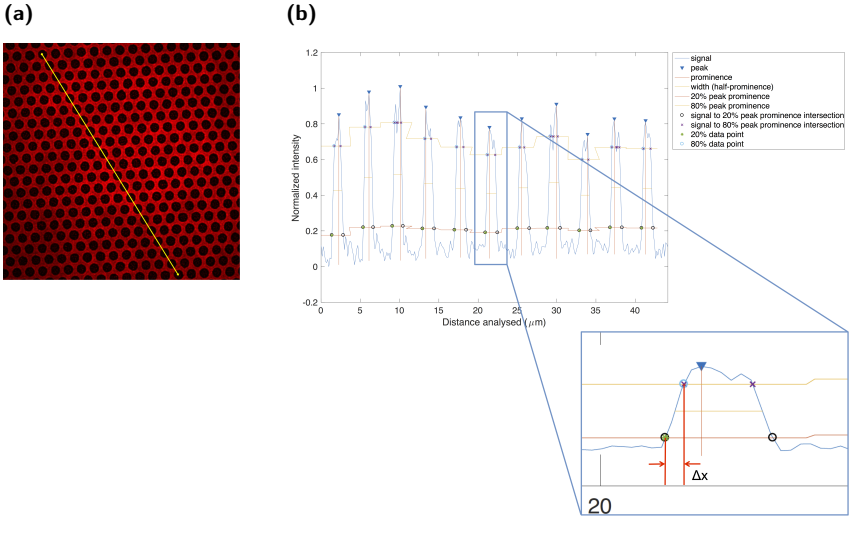


Figure 2.4: Determining pattern steepness. (a) Manually set with a line cross section of intensity profile. (b) Pattern intensity profile and magnified image of the peak steepness Δx detection on 20% and 80% height

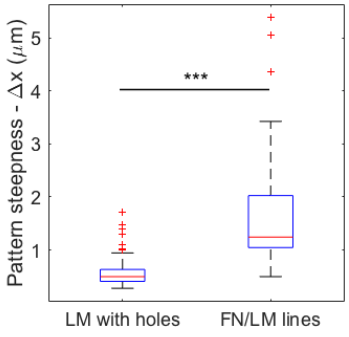


Figure 2.5: LM with holes and FN/LM crossing line pattern steepness on PDMS, determined from the intensity profile. NS, P>0.05; *P<0.05; **P<0.005; ***P<0.0005 according to Mann - Whitney test

0.1 kPa stiffness range accordingly. However gel exposure to UV-ozone enabling protein binding resulted in surface wrinkling for gels with rigidities below 40 kPa. Such an effect can be explained by the formation of a silica (SiO_2)-like stiffer layer on the PDMS surface caused by the formation of new Si-O-Si bonds under plasma oxidation [35, 36]. By decreasing the time of UV-ozone treatment from 10 min to 5 min we could prevent wrinkle formation, but surface patterning became impossible due to stickyness of the gel caused by insufficient crosslinking.

2.3.3 hPAA gels micropatterning

As an alternative, we used hPAA hydrogels that were reported to provide the same flexibility in substrate micropatterning as PDMS gels, but remain polyacrylamide hydrogel precision in controlling stiffness [14]. Authors utilized this method to obtain pattern structures $> 10\ \mu m$ in size, while our FN spots required to go down to $2\ \mu m$ scale.

First, we tested two stamping approaches that as aforementioned showed good results for PDMS flat surface stamping: i)direct patterning with micropillar arrays of 137 kPa stiffness and ii) two step stamping of FN monolayer with hole patterned LM layer on top (Fig. 2.2a). The first approach appeared to be not suitable due to the uneven surface of the gel, which did not allow to obtain sharp, homogeneous patterns of the dots on top of the gel surface (Supplementary Fig. 2.9a). Furthermore, stiff thin pillars would create micropits in the gel surface under certain

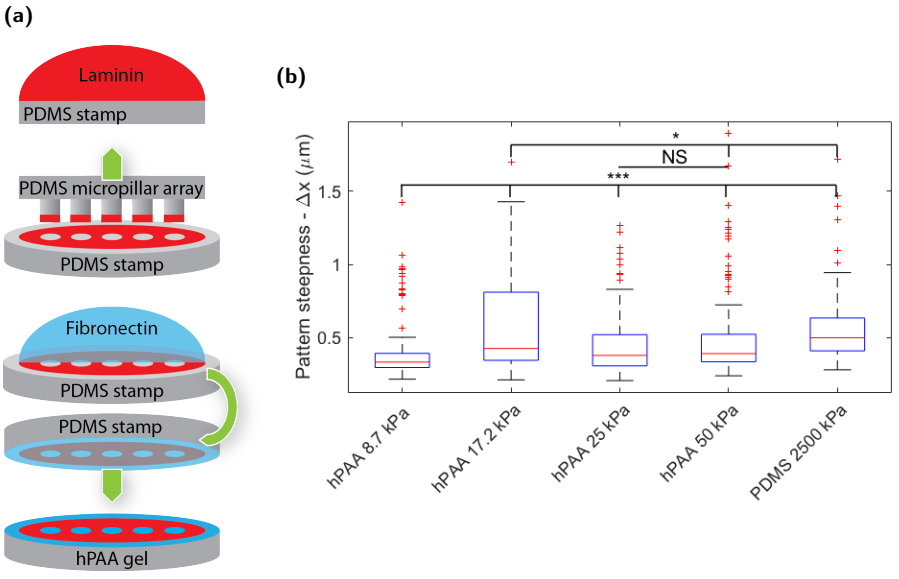


Figure 2.6: hPAA hydrogels patterning. (a) "micro contact printing" scheme for hPAAm hydrogels with FN spots surrounded by LM-111. (b) Pattern steepness on hPAA gels of several stiffness compared to the one on PDMS flat surface. NS, P>0.05; *P<0.05; **P<0.005; ***P<0.0005 according to Mann - Whitney test

pressure on the micropillar array stamp. In the second case we discovered that the LM layer simply didn't bind on top of FN to the surface of the gel (Supplementary Fig. 2.9b).

To obtain a desirable pattern of FN dots surrounded by LM on top of the hPAA hydrogels we developed an approach based on the technique mentioned in [29]. In this paper authors used "re-inking" of the PDMS stamp after modification of the first protein layer via "stamp-off" approach. Hence, in our new microcontact printing sequence a PDMS stamp was first covered by LM-111, then the UV-ozone activated PDMS micropillar array was pressed into the dried LM layer to create holes in it, followed by PDMS stamp "re-inking" with FN, drying and inverting onto the dried hPAA gel for 1 hour. The resulting pattern resembled the earlier obtained on top of the flat PDMS surface (2.2c) and had good reproducibility. Pattern sharpness quantification showed steepness values within 1 μm for layer of LM with holes on top of hPAA gels of different stiffness (Fig. 2.6b)

2.4 Discussion

BMs are spatially organized into a thin sheet of ECM underlying every epithelium and vascular endothelium [37–39], mainly built from collagen type IV, LM and proteoglycans. Although BMs are extensively studied, their *in vitro* mimicking is challenging and commonly limited to 2D coating to replicate the BM biochemical composition, ECM protein functionalization of gels or micro/nano post arrays to resemble the BM mechanical properties or designs that allow investigating the BM functionality, like PDMS porous thin films or nanofibrous scaffolds [40–42]. Recent findings revealed that LM and type IV collagen are not organized into one homogeneous network, but form two layers, allowing fibroblasts to interact with collagen on one side and epthelial cells or EC to interact with LM on the other [22]. Moreover, deposits of FN are found by EM in the LM-rich layer in vivo [4, 7, 43]. Here, we focussed on designing an *in vitro* model of the PC-EC interaction environment of the capilarry BM (Fig. 1.1).

The BM itself is on average 200-400 nm thick [44, 45] and requires 3D ECM modeling, while the PC-EC interstitial layer is much thinner and allowed us to use 2D ECM modeling approaches, such as protein μCP on top of substrates of controlled rigidity. This approach was chosen to mimic LM and FN spatial organization in the BM and its overall stiffness. Our first attempt to obtain FN dots on top of PDMS gels of different stiffness, prepared according to the protocol used in [21], revealed unwanted wrinkle formation on the gel surfaces with stiffness lower 40 kPa after exposure to the UV-ozone. This effect has been shown by other studies [35, 36] to be related to the stiffer silica (SiO_2)-like layer formation on the PDMS surface under UV-ozone treatment. While on stiff PDMS gels this effect is not directly visible, on the soft ones it results in surface wrinkling. Although such a phenomenon is extensively used to obtain PDMS surfaces with grooves of a controlled geometry [46–48], for our model it is not acceptable, making the stiffness of PDMS gels unreliable.

We observe that μCP on top of hPAA hydrogels represents a better system in comparison to μCP on PDMS gels, to obtain spatially organized proteins on top of matrices of low stiffness in a range that is biologically relevant for microvessels [49, 50]. The presence of N-hydroxyethylacrylami-de (HEA) in these gels results in a constant availability of hydroxyl groups on the gel surface enabling hydrogen protein

bonding without the need of surface hydroxylation with oxygen plasma, piranha, HF, UV-ozone etc., as is needed in case of glass, Si or PDMS substrates [51]. We also find that the size of μCP pattern features can be lowered from $> 10\ \mu m$ to $2\ \mu m$ by combining hPAA gels with a "stamp-off" protein printing approach that previously was mainly used for micropatterning on a PDMS flat surface or PDMS micropillar arrays. Importantly, pattern steepness on hPAA hydrogels is not lower than the one on PDMS flat surface and does not depend on the gel stiffness. A possible explanation for the last observation is that hPAA gel stamping is preceeded by dehydration of the gel μCP and followed by gel rehydration when stamping is finished. Hence, at the moment of protein printing all gels have highly similar stiffnesses allowing for identical pattern qualities. This makes our system easy to reproduce and use.

Taken together, our model represents the PC-EC interstitial layer of the capillary BM, including the LM layer and the FN deposits. Our combinations of stamping approaches will be of general applicability to create heterogenous patterned surfaces resembling other biological structures. The combination of stamping techniques and hydrogels of variable stiffness allows investigating responses of cells to altered substrate stiffness. Our design does not include analysis of the inverse process: cellular forces applied to the BM. This can be made possible for instance by adding marker beads for traction force microscopy [16]. In addition, our model can be further expanded to represent the complete capillary BM by including proteogycans and adding a seperate layer rich in type IV collagen.

2.5 Appendix

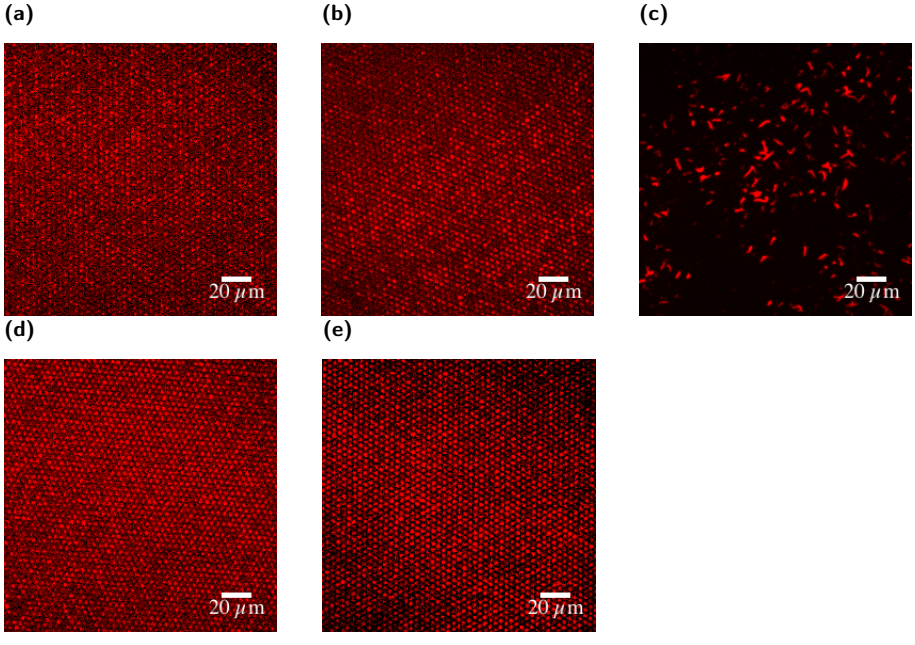


Figure 2.7: FN dots stamping test on top of (a, d) PDMS 1:10 prepared in a polystyrene dish; (b, e) PDMS 1:10 prepared on a Si blank wafer and (c) glass coverslip. Stapming was done with PDMS micropillar arrays of 42.7 kPa (a-c) and 137 kPa (d, e) stiffness

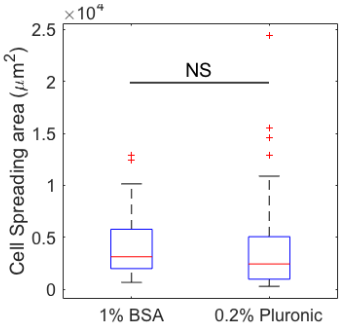


Figure 2.8: Pericyte (CD31-(Dif31) cell line) spreading area after 4 hours incubation on PDMS flat surface stamped with FN dots and blocked with 1% BSA or 0.2% Pluronic. NS, P>0.05; *P<0.05; **P<0.005; ***P<0.0005 according to Mann - Whitney test

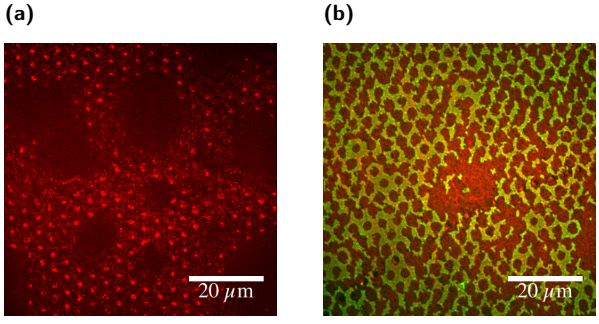


Figure 2.9: FN (red) and LM (green) pattern stamping results on top of the hPAA gels, obtained with PDMS micropillar arrays (a) and "stamp-off" double step protein μCP (b)

Bibliography

[1] Richard O Hynes. « The extracellular matrix: not just pretty fibrils ». In: *Science* 326.5957 (2009), pp. 1216–1219.

[2] Fiona M Watt and Wilhelm TS Huck. « Role of the extracellular matrix in regulating stem cell fate. » In: *Nature Reviews* 14.8 (2013), pp. 467–73. ISSN: 1471-0072.

[3] Christian Frantz, Kathleen M Stewart and Valerie M Weaver. « The extracellular matrix at a glance. » In: *J. Cell. Sci.* 123.Pt 24 (2010), pp. 4195–200. ISSN: 0021-9533.

[4] Annika Armulik, Alexandra Abramsson and Christer Betsholtz. « Endothelial-pericyte interactions. » In: *Circ. Res.* 97.6 (2005), pp. 512–23. ISSN: 0009-7330.

[5] Raghu Kalluri. « Basement membranes: structure, assembly and role in tumour angiogenesis ». In: *Nature Reviews Cancer* 3.6 (2003), pp. 422–433. ISSN: 1474-175X.

[6] Rupert Hallmann et al. « Expression and Function of Laminins in the Embryonic and Mature Vasculature ». In: *Physiol Rev.* 85.3 (2005), pp. 979–1000. ISSN: 0031-9333.

[7] PJ Courtoy and J Boyles. « Fibronectin in the microvasculature: localization in the pericyte-endothelial interstitium. » In: *J. Ultrastruct. Res.* 83.3 (1983), pp. 258–73. ISSN: 0022-5320.

[8] Greg M Harris, Irene Raitman and Jean E Schwarzbauer. « Cell-derived decellularized extracellular matrices. » In: *Methods Cell Biol.* 143 (2018), pp. 97–114. ISSN: 0091-679X.

[9] Rajesh Vasita and Dhirendra S Katti. « Nanofibers and their applications in tissue engineering. » In: *Int J Nanomedicine* 1.1 (2006), pp. 15–30. ISSN: 1176-9114.

[10] Quynh P Pham, Upma Sharma and Antonios G Mikos. « Electrospinning of polymeric nanofibers for tissue engineering applications: a review. » In: *Tissue Eng.* 12.5 (2006), pp. 1197–211. ISSN: 1076-3279.

[11] PX Ma and R Zhang. « Synthetic nano-scale fibrous extracellular matrix. » In: *J. Biomed. Mater. Res.* 46.1 (1999), pp. 60–72. ISSN: 0021-9304.

[12] Peter Berndt, Gregg B Fields and Matthew Tirrell. « Synthetic lipidation of peptides and amino acids: monolayer structure and properties. » In: *Journal of the American Chemical Society* 117.37 (1995), pp. 9515–9522. ISSN: 0002-7863.

[13] RJ Pelham and Yl Wang. « Cell locomotion and focal adhesions are regulated by substrate flexibility. » In: *Proc. Natl. Acad. Sci. U.S.A.* 94.25 (1997), pp. 13661–5. ISSN: 0027-8424.

[14] Thomas Grevesse et al. « A simple route to functionalize polyacrylamide hydrogels for the independent tuning of mechanotransduction cues. » In: *Lab on a Chip* 13.5 (2013), pp. 777–80. ISSN: 1473-0189.

[15] Rachelle N Palchesko et al. « Development of Polydimethylsiloxane Substrates with Tunable Elastic Modulus to Study Cell Mechanobiology in Muscle and Nerve ». In: *PLoS ONE* 7.12 (2012).

[16] Ulrich Schwarz and Jérôme Soiné. « Traction force microscopy on soft elastic substrates: A guide to recent computational advances ». In: *Biochimica Et Biophysica Acta Bba - Mol Cell Res* 1853.11 (2015), pp. 3095–3104. ISSN: 0167-4889.

[17] Zhou Li et al. « Quantifying the traction force of a single cell by aligned silicon nanowire array. » In: *Nano Lett.* 9.10 (2009), pp. 3575–80. ISSN: 1530-6984.

[18] Jau-Ye Shiu et al. « Nanopillar force measurements reveal actin-cap-mediated YAP mechanotransduction ». In: *Nat Cell Biol* 20.3 (2018), pp. 262–271. ISSN: 1465-7392.

[19] John L Tan et al. « Cells lying on a bed of microneedles: an approach to isolate mechanical force. » In: *Proc. Natl. Acad. Sci. U.S.A.* 100.4 (2003), pp. 1484–9. ISSN: 0027-8424.

[20] Dhwani Jhala and Rajesh Vasita. « A Review on Extracellular Matrix Mimicking Strategies for an Artificial Stem Cell Niche ». In: *Polymer Reviews* 55.4 (2015), pp. 561–595. ISSN: 1558-3724.

[21] Britta Trappmann et al. « Extracellular-matrix tethering regulates stem-cell fate. » In: *Nat Mater* 11.7 (2012), pp. 642–9. ISSN: 1476-1122.

[22] Willi Halfter et al. « The bi-functional organization of human basement membranes. » In: *PLoS ONE* 8.7 (2013), e67660. ISSN: 1932-6203.

[23] R Singhvi et al. « Engineering cell shape and function ». In: *Science* (1994). ISSN: 0036-8075.

[24] Jinghuan Huang et al. « Impact of order and disorder in RGD nanopatterns on cell adhesion. » In: *Nano Lett.* 9.3 (2009), pp. 1111–6. ISSN: 1530-6984.

[25] Amit Kumar and George M Whitesides. « Features of gold having micrometer to centimeter dimensions can be formed through a combination of stamping with an elastomeric stamp and an alkanethiol "ink" followed by chemical etching ». In: *Appl Phys Lett* 63.14 (1993), pp. 2002–2004. ISSN: 0003-6951.

[26] A Bernard et al. « Printing patterns of proteins ». In: *Langmuir* (1998). ISSN: 0743-7463.

[27] CD James et al. « Patterned protein layers on solid substrates by thin stamp microcontact printing ». In: *Langmuir* (1998). ISSN: 0743-7463.

[28] John L Tan et al. « Simple Approach to Micropattern Cells on Common Culture Substrates by Tuning Substrate Wettability ». In: *Tissue Eng* 10.5-6 (2004), pp. 865–872. ISSN: 1076-3279.

[29] Ravi A Desai et al. « Subcellular spatial segregation of integrin subtypes by patterned multicomponent surfaces. » In: *Integr Biol (Camb)* 3.5 (2011), pp. 560–7. ISSN: 1757-9694.

[30] Hedde van Hoorn et al. « The Nanoscale Architecture of Force-Bearing Focal Adhesions ». In: *Nano letters* 14 (2014), pp. 4257–4262.

[31] Olivia du Roure et al. « Force mapping in epithelial cell migration. » In: *Proc. Natl. Acad. Sci. U.S.A.* 102.7 (2005), pp. 2390–5. ISSN: 0027-8424.

[32] Ravi A Desai, Natalia M Rodriguez and Christopher S Chen. « Stamp-off" to micropattern sparse, multicomponent features. » In: *Methods in Cell Biology* 119 (2014), pp. 3–16. ISSN: 0091-679X.

[33] Xue Jiang et al. « Cell Growth in Response to Mechanical Stiffness is Affected by Neuron- Astroglia Interactions ». In: *The Open Neuroscience Journal* 1.1 (2007), pp. 7–14. ISSN: 1874-0820.

[34] Thomas Grevesse et al. « Opposite rheological properties of neuronal microcompartments predict axonal vulnerability in brain injury ». In: *Scientific Reports* 5 (2015), p. 9475.

[35] H. Hillborg et al. « Crosslinked polydimethylsiloxane exposed to oxygen plasma studied by neutron reflectometry and other surface specific techniques ». In: *Polymer* 41.18 (2000), pp. 6851–6863. ISSN: 0032-3861.

[36] G. Bar et al. « Investigation of the stiffness change in, the indentation force and the hydrophobic recovery of plasma-oxidized polydimethylsiloxane surfaces by tapping mode atomic force microscopy ». In: *Polymer* 42.8 (2001), pp. 3627–3632. ISSN: 0032-3861.

[37] Peter D Yurchenco and Bruce L Patton. « Developmental and patho-genic mechanisms of basement membrane assembly. » In: *Curr. Pharm. Des.* 15.12 (2009), pp. 1277–94. ISSN: 1381-6128.

[38] Ranjay Jayadev and David Sherwood. « Basement membranes ». In: *Curr Biol* 27.6 (2017), R207–R211. ISSN: 0960-9822.

[39] Lema F Yousif, Jacopo Russo and Lydia Sorokin. « Laminin isoforms in endothelial and perivascular basement membranes ». In: 7.1 (2013), p. 101110. ISSN: 1933-6918.

[40] Joana Bicker et al. « Blood-brain barrier models and their relevance for a successful development of CNS drug delivery systems. A review ». In: *Eur J Pharm Biopharm* 87.3 (2014), pp. 409–432. ISSN: 0939-6411.

[41] Dongeun Huh et al. « Reconstituting organ-level lung functions on a chip. » In: *Science* 328.5986 (2010), pp. 1662–8. ISSN: 0036-8075.

[42] Akihiro Nishiguchi et al. « Basement Membrane Mimics of Biofunctionalized Nanofibers for a Bipolar-Cultured Human Primary Alveolar-Capillary Barrier Model. » In: *Biomacromolecules* 18.3 (2017), pp. 719–727. ISSN: 1525-7797.

[43] Ethan A Winkler, Robert D Bell and Berislav V Zlokovic. « Central nervous system pericytes in health and disease ». In: *Nature Neuroscience* 14.11 (2011), pp. 1398–1405. ISSN: 1097-6256.

[44] Joseph Candiello et al. « Biomechanical properties of native basement membranes ». In: 274.11 (2007), pp. 2897–2908. ISSN: 1742-4658.

[45] Joseph Candiello, Gregory Cole and Willi Halfter. « Age-dependent changes in the structure, composition and biophysical properties of a human basement membrane ». In: *Matrix Biol* 29.5 (2010), pp. 402–410. ISSN: 0945-053X.

[46] Fabian Brau et al. « Multiple-length-scale elastic instability mimics parametric resonance of nonlinear oscillators ». In: *Nat Phys* 7.1 (2010), pp. 56–60. ISSN: 1745-2473.

[47] Jeong Lee et al. « A simple fabrication process for stepwise gradient wrinkle pattern with spatially-controlled wavelength based on sequential oxygen plasma treatment ». In: *Microelectron Eng* 176 (2017), pp. 101–105. ISSN: 0167-9317.

[48] Ned Bowden et al. « The controlled formation of ordered, sinusoidal structures by plasma oxidation of an elastomeric polymer ». In: *Appl Phys Lett* 75.17 (1999), pp. 2557–2559. ISSN: 0003-6951.

[49] Takayuki Okamoto et al. « Gap junction-mediated regulation of endothelial cellular stiffness ». In: *Sci Reports* 7.1 (2017), p. 6134. ISSN: 2045-2322.

[50] Zhongkui Hong et al. « Vascular Smooth Muscle Cell Stiffness and Adhesion to Collagen I Modified by Vasoactive Agonists ». In: *Plos One* 10.3 (2015), e0119533.

[51] Nick Glass et al. « Organosilane deposition for microfluidic applications. » In: *Biomicrofluidics* 5.3 (2011), pp. 36501–365017. ISSN: 1932-1058.

BIBLIOGRAPHY

Chapter 3

Fibronectin patches as anchoring points for force sensing and transmission in human induced pluripotent stem cell-derived pericytes [1]

abstract

Pericytes (PCs), the mural cells of blood microvessels, have emerged as important regulators of vascular morphogenesis and function. PCs have been reported to participate in the regulation of the capillary diameter and blood flow. Certain pathological conditions such as cerebral ischemia, Alzheimer's disease and diabetic retinopathy are associated with the increase of PC-contractility and overall PC-death. Nevertheless, the degree to which PCs contribute to the regulation of microvessel blood flow is still a matter of controversy. It has been suggested by electron-microscopy that PCs use small deposits of fibronectin (FN), within the laminin (LM) rich basement membrane (BM) aligning the endothelial cells (ECs), as anchoring points to the capillary. Here, we developed an *in vitro* model for PC adhesion plaques and investigated the mechanical aspects of human induced pluripotent stem cell (hiPSC)-derived PCs.

1. This chapter is based on: O. Iendaltseva, V.V. Orlova, C.L. Mummery, E. H. J. Danen and T. Schmidt, Fibronectin Patches as Anchoring Points for Force Sensing and Transmission in Human Induced Pluripotent Stem Cell-Derived Pericytes, published in *Stem Cell Reports*, 2020

Our results showed that PCs strongly prefer FN over LM for the formation of force-loaded adhesion plaques when interacting with a variety of FN/LM patterned substrates. Moreover, we found that PCs sense a preferred FN substrate stiffness in the range of ∼50 kPa on micropillar arrays and ∼25 kPa on continuous substrates. At both lower and higher substrate stiffness, PCs react by dramatically increasing traction force application, altered cytoskeletal organization and cell matrix adhesion distribution patterns in combination with decreased cell spreading behavior. Together, our findings reveal how FN deposits as observed in the BM of microvessels provide anchoring points for mechanical regulation of capillaries by PCs.

3.1 Introduction

Pericytes (PCs) cover the majority of all capillaries in the human body [1]. PCs express markers that are shared with mesenchymal stem cells and smooth muscle cells but, in mid-capillary regions lack smooth muscle actin (SMA) expression [2, 3]. PCs have been shown to promote regulation of vascular development, stabilization and maturation of vessels, and the maintenance of the blood-brain-barrier [4, 5]. Although PCs are essential for the development of the vascular tree [6] their precise role in the control of blood flow through capillaries is still highly debated [7, 8]. PCs are embedded in the capillary basement membrane (BM) and develop characteristic branched processes around microvessels [1, 2]. This morphology together with the presence of contractile proteins like actin, high concentration of myosin, tropomyosin and other [9–12] suggests their functional role in applying mechanical forces to strengthen the blood vessel wall, and their participation in the regulation of microvascular blood flow in particular in the brain [13, 14]. Notably, dysfunction or loss of PCs has been implicated in pathologies such as cerebral ischemia, Alzheimer's disease and diabetic retinopathy [15–18]. Thus, PC-endothelial cell (EC) mechanical interaction represents a potential target for therapy in such conditions.

PCs and ECs build-up a variety of mechanical and biochemical interconnections. They use peg-and-socket contacts that contain gap junctions [19] for direct communication and signaling, cell-to-cell adhesions by N-cadherins [20], and integrin-mediated binding of both cell types to the extracellular matrix of the BM of the capillaries [21]. A critical component of the PC/ECs proper assembly and vessel formation is EphrinB2 reverse signaling. Initial cell-to-cell contact during agiogenesis leads to EphrinB2 engagement by EphB membrane receptors and subsequent EphrinB2 phosphorylation. EphrinB2 phosphorylation, in turn, starts reverse signaling that promotes cell-to-cell adhesion formation [22, 23]. In particular, the integrins and N-cadherins provide two independent adhesion systems that allow PCs to apply forces to their environment and thereby affecting the blood flow in the capillary. It has been shown that PC-EC connections through N-cadherins occur mainly during angiogenesis, being lost with vessel maturation and BM generation [24, 25]. Hence, in mature resting vasculature the mechanical PC-EC connection is dominated by BM-mediated integrin adhesion. The BM in capillaries contains collagen type IV in the outer layer and laminin (LM)-411/511

in the inner layer close to the ECs [26, 27]. PCs are situated within the BM where they may bind collagen and LM. Yet, electron microscopical analysis further suggests a role for $0.2 - 2\ \mu m$ deposits of fibronectin (FN) as specific anchoring points [28–30] (Figure 1.1).

PCs may play an important role in mechanical regulation of the vasculature by providing additional mechanical strength to the endothelium or by regulating blood-flow by their contractility. How this is realized is poorly understood, yet understanding of this process might lead to novel concepts in treatment of pathological conditions, and to the identification of novel targets for therapy. Here we developed an in vitro model to investigate mechanical aspects of PC behavior. We utilized our previously described human induced pluripotent stem cell-derived PCs (hiPSC) with a close to mid-capillary PC phenotype, lacking smooth muscle actin (SMA) expression [31, 32]. Micropatterned surfaces of LM and FN, mimicking BM structures were generated on surfaces varying in mechanical stiffness and in topography. This allowed us to obtain quantitative information on cell morphology and cell contractility. Our results show that (i) PCs strongly prefer FN over LM for adhesion formation, (ii) PCs sense a preferred FN substrate stiffness for spreading, and (iii) PCs respond to either lower or higher stiffness with increased traction forces, altered cytoskeletal organization, and decreased cell spreading. Our results suggest that FN deposits, as observed in the endothelial BM by electron-microscopy, provide the anchoring points for mechanical regulation of capillaries by PCs.

3.2 Methods

3.2.1 Cell culture

CD31– (dif31 and dif43) and SV80 cell lines were cultured in Dulbecco's Modified Eagle's Medium (DMEM, Gibco|Thermo Fisher Scientific, USA) supplemented with 10% fetal bovine serum (HyClone, Etten-Leur, The Netherlands), 25 U/ml penicillin and 25 µg/ml streptomycin (Invitrogen/Fisher Scientific). NIH 3T3 cells were cultured in Dulbecco's Modified Eagle's Medium (DMEM, Sigma) supplemented with 10% calf serum (Thermo Scientific/Sigma), 2 mM glutamine, and 100 µg/ml penicillin/streptomycin. For all experiments cells were seeded at 20 000 cells per sample density directly on the patterned surface. After 4 hours

incubation they were fixed 10' in 4% paraformaldehyde in PBS for immunostaining.

3.2.2 Immunostaining

After cells were fixed, they were permeabilized for 10' with 0.1% Triton-X and blocked for 60' with 1% BSA (Sigma, a2153) in PBS. For cell matrix adhesion assays cells were prepared for staining according to the earlier described method [33]. Briefly, after 4 hours incubation, cells were washed in cytoskeleton buffer (CB), incubated 15" in 0.1-0.25% Triton-X, 0.4% paraformaldehyde and 1µg/mL phalloidin in CB, washed again with CB, and fixed for 10' with 4% paraformaldehyde in CB. In the end they were permeabilized for 10' with 0.5% Triton-X and blocked for 60' with 1% BSA in PBS. Immunostaining was done depending on the experiment, with Alexa532 phalloidin (Thermo Fisher Scientific, a22282), primary antibodies against paxillin (Thermo Fisher Scientific, aho0492), talin (Sigma, t3287), vinculin (Sigma, v9131), alpha-v integrin (Merck Millipore, mab1978), beta-1 integrin (Santa Cruz, sc-18887) and laminin-111 (Sigma, l9393), followed with Alexa532/647 conjugated secondary antibody against mouse IgG (Thermo Fisher Scientific, a11002/Jackson, 115-605-006 respectively) and Alexa647 conjugated secondary antibody against rabbit IgG (Thermo Fisher Scientific, a21244).

3.2.3 PDMS surface patterning with FN and LM

PDMS surface with a pattern, where LM would surround FN spots or inverse, was produced by combining "stamp-off" and "microcontact printing" methods [34]. Two flat PDMS (Sylgard 184,Dow Corning) 1:30 (crosslinker:prepolymer ratio, cured 16 hours at 65°C) stamps were separately incubated for 60' with a 40 µl drop of 50 µg/ml LM-111 (Sigma, l2020) in milliQ water and a 40 µl mixture of 50 µg/ml FN (Sigma, f1141) plus 10 µg/ml Alexa405-FN in milliQ, washed with milliQ and dried under laminar flow. With a help of UV-ozone activated PDMS 1:10 micropillar arrays, where 2 µm diameter pillars with 2 µm spacing and hexagonal order, were obtained holes in one of the layers. Further, two stamps were inverted one by one on top of the UV-ozone activated PDMS 1:10 surface and incubated for 10' each, to get previously modified protein sheet on top of the uninterrupted layer of the second (Fig. 2.2a, b).

PDMS surfaces with a grid of crossing FN and LM lines were obtained in a similar manner. First, two PDMS 1:10 molds with 5 μm high lines of different width were produced by using replica-molding from a silicon wafer. After UV-ozone activation 10', they were pushed onto PDMS 1:30 stamps with a protein layer dried on them. Followed by 10' incubation and removal, this molds left a negative of the pattern in the protein layer on top of the PDMS stamps. Further, PDMS stamps were inverted on top of the UV-ozone activated PDMS 1:10 surface, creating a pattern of crossing LM and FN lines on it (Fig. 2.3a).

PDMS surfaces with FN lines under a layer of LM with holes were printed by using PDMS stamps with LM and FN layers modified as aforementioned. PDMS micropillar array was used to make holes in the dry LM monolayer and PDMS mold with lines – to create a line pattern in FN. Further, this stamps were loaded on top of the UV-ozone activated PDMS surface, with FN stamp going first (Fig. 2.3b). Finally, all patterned PDMS surfaces were blocked by using 1% BSA 60'.

3.2.4 PDMS micropillar array preparation

PDMS micropillar arrays were prepared as was described before [35, 36]. Briefly, SI mold was made by two-step Deep Reactive Ion Etching (DRIE) process. This yielded a 10×10 mm hexagonal array of 2 μm diameter holes with 2 μm spacing and varying depth, flanked by two 50 μm deep 10×2 mm tranches. After mold passivation with trichloro silane (Sigma), PDMS 1:10 was poured over it and cured for 20 hours at 110°C. The peeled off PDMS had a negative of the mold shape with micropillar array and 50 μm high spacers on the sides of it. This array was functionalized with the help of PDMS 1:30 stamps and dried protein of interest on top of them. A 40 μl drop of FN or LM-111 mixture in water was incubated for 60' on the PDMS 1:30 stamp, then washed and dried under laminar flow. This stamp was then genly loaded onto UV-ozone activated PDMS micropillar array for 10'. Finally, stamped array was blocked with 0.2% Pluronic (F-127, Sigma) in PBS for 60' at room temperature and washed with PBS.

3.2.5 Hydroxy-PAAm gel preparation

Hydroxy-PAAm hydrogels were made following a previously described method [37]. Gels stiffer then 40 kPa were obtained following the same

procedure as suggested in [38] and [39] by increasing polyacrylamide monomer concentration with a fixed monomer/crosslinker ratio of 29:1. Further gels were stamped with LM&FN pattern where FN spots were surrounded by LM. This was achieved by using an adapted "stamp-off" and "micro-contact printing" approaches described in [34]. A 40 µl drop of 50 µg/ml LM-111 in milliQ water was incubated for 60' on top of the 10×10 mm PDMS 1:30 stamp, followed by washing and drying under laminar flow. Then OV-ozone activated PDMS micropillar array was pushed onto the dry LM-111 monolayer to obtain holes in the places of micropillar-LM-111 contacts. After 10' incubation the array was removed and a second 40 µl drop of 50 µg/ml FN plus 10 µg/ml Alexa405-FN in milliQ was gently spread onto the first layer for 60'. Finally, the stamp was washed and dried under laminar flow. Hydroxy-PAAm hydrogels were dried using nitrogen flow and incubated with the stamp for 60' (Fig. 2.6a), following blocking with 1% BSA in PBS o/n and washing with PBS.

3.2.6 Microscopy

Confocal imaging was performed on a home-built setup based on an Axiovert200 microscope body (Zeiss), spinning disk unit (CSU-X1, Yokogawa) and an emCCD camera (iXon 897, Andor). IQ-software enabled setup-control and data acquisition. Lasers of 405 nm (CrystaLaser), 488 nm (Coherent), 514 nm, 561 nm (Cobolt) and 642 nm (Spectra Physics) wavelength were coupled into the CSU via polarization maintaining single-mode fiber. Spacers on the sides of micropillar arrays allowed placing them upside down onto #0 coverslips (Menzel Glaser) with adhered cells facing down. This approach ensured reproducible cell observation within the limited working distance of a high-NA objective on an inverted microscope. For PDMS and hPAA 2D assays parafilm spacers were made directly on top of the glass coverslips.

3.2.7 Image analysis

Cell spreading area was quantified by using FIJI software. First the background was subtracted by adjusting threshold level, followed by the cell edge selection with a tracing tool. In the end the mean values for at least 30 cells per condition were calculated.

Cell traction forces were measured by using micropillar array technology [36, 40, 41] and quantified as previously described [35]. Micropillar tops were functionalized with fluorescently labeled FN or LM with further immunostaining. This allowed us to detect deflections with ∼30 nm accuracy that corresponded to 500 pN for soft and 2 nN for stiff pillars force precision by using a specifically designed Matlab script.

Cell-matrix adhesion area was determined as mentioned in [42]. Fluorescent images of cell-matrix adhesion proteins were passed through a Gaussian low pass filter, then – hole-filling algorithm and watershed segmentation. In the end all results were manually controlled to remove images with incorrect adhesion detection due to a low signal-to-noise ratio.

3.2.8 Statistical analysis

To assess significance of the difference between two conditions, the Wilcoxon rank sum test in the Matlab program was used. This test is an equivalent to a Mann-Whitney U test. Significance for the force application by PCs represented in the graph 3.3e was quantified by using ANOVA test comparing means of the mean values determined for at least three independent experiments per each stiffness.

3.3 Results

3.3.1 Preferred binding of PCs to FN patches on multilayered substrates.

We investigated whether PCs may preferentially use FN deposits for attachment onto capillaries. As a source for PCs, we used hiPSC line LUMC06iCTRL-derived PCs [32, 43]. As hallmarks for PCs, these cells lacked the endothelial marker CD31, they expressed the PC/mesenchymal stem cell markers PDGFRβ, NG2, CD146, CD44, CD73, CD105, they expressed very little to no smooth muscle actin (SMA), very little SMC markers such as (SM)22 and Calponin (CNN1), all distinguishing them from SMCs. Moreover, as we described earlier, these PCs promote vascular development in PC-EC co-cultures [31, 32].

We modeled LM and FN arrangements in the endothelium-PC interstitia, which has been described by electron microscopy previously [28]. In EM-studies it was shown that FN was arranged in the form

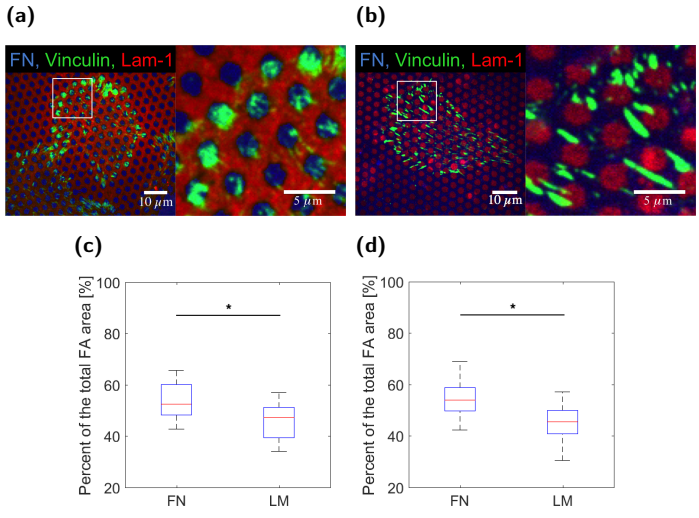


Figure 3.1: PCs placed on PDMS flat surfaces stamped with FN&LM-111. (a) Confocal immunofluorescence images of PCs (dif31) seeded on the type of pattern depicted in (2.2a) with vinculin labeled (green). Confocal immunofluorescence images of PCs (dif31) seeded on the type of pattern depicted in (2.2b) with vinculin labeled (green). (c) Percentage of PC (dif31) focal adhesions (FAs) located on FN and LM for (a). (d) Percentage of PC (dif31) focal adhesions (FAs) located on FN and LM for (b). (c) and (d) results are derived from three independent experiments performed in minimum two replicates. At least 10 images were analyzed from each sample. NS, P>0.05; *P<0.05; **P<0.005; ***P<0.0005 according to Mann - Whitney test. See also Figure 3.8.

of micrometer-sized patches surrounded by LM-411/511 within the BM of capillaries (Figure 1.1). To mimic the *in vivo* observations in our *in vitro* experiments we used a multilayer stamp-off method [34] (Figure 2.2). First, a PDMS micropillar array consisting of 2 μm wide pillars in a hexagonal arrangement of 2 μm spacing, activated in an UV-ozone cleaner was pressed onto and released from a LM monolayer deposited on a flat PDMS substrate. The procedure left a homogeneous LM layer with patterned holes on the flat PDMS stamp. Subsequently, this layer was transferred onto a second flat FN-coated PDMS surface. In the resulting multilayered surface, FN was accessible through the holes in the LM layer (Figure 2.2a). For visualization FN was mixed with a low amount (<1%) of Alexa-405 conjugated FN. LM-111 was visualized using an anti-LM-

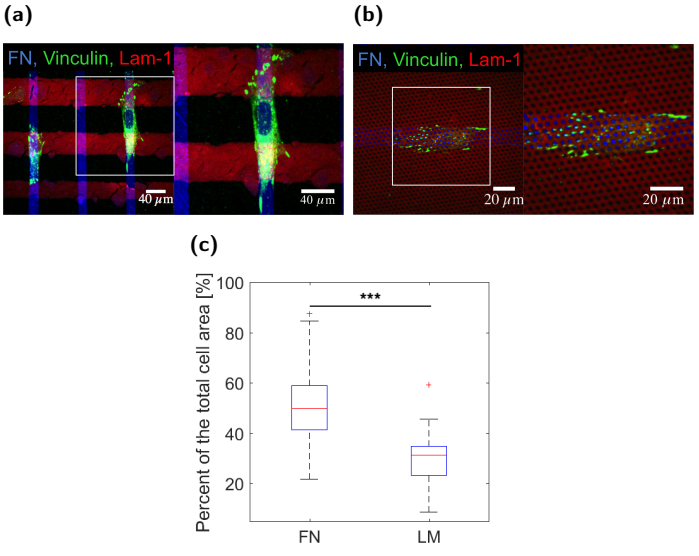


Figure 3.2: PCs placed on PDMS flat surfaces stamped with FN&LM-111. (a) Confocal immunofluorescence images of PCs (dif31) seeded on the type of pattern depicted in (2.3a) with vinculin labeled (green). (b) Confocal immunofluorescence images of PCs (dif31) seeded on the type of pattern depicted in (2.3b) with vinculin labeled (green). (c) Percentage of PC (dif31) focal adhesions (FAs) located on FN and LM for (a). In (c), the results are derived from three independent experiments performed in minimum two replicates. At least 10 images were analyzed from each sample. NS, $P>0.05$; *$P<0.05$; **$P<0.005$; ***$P<0.0005$ according to Mann - Whitney test

111 antibody followed by staining with an Alexa-647-coupled secondary antibody.

PCs were incubated for 4 hours on the patterned substrates, fixed, and stained for F-actin and cell-matrix adhesion proteins. PCs could readily attach and spread on substrates coated with either LM or FN monolayers. However, in the patterned combined protein model, cells strongly preferred to attach to FN patches and avoided areas covered by LM. Vinculin and α_v-integrin staining showed cell-matrix adhesions formed preferentially on FN patches, avoiding areas containing LM (Figure 3.1a, c, 3.8a).

To rule-out effects caused by the order in which FN and LM were stamped on the surface, an inverse approach was taken. First the stamp-off method was used to create holes in the FN monolayer, which was sub-

sequently transferred onto a flat PDMS surface coated with LM (Figure 2.2b). Again, vinculin staining revealed that PCs formed cell-matrix adhesions almost exclusively on the FN-coated area whereas LM-111-coated areas were avoided (Figure 3.1b,d).

We further generated substrates consisting of crossing stripes of LM and FN by stamping a PDMS surface with a grid of $20-60$ μm LM-111 and 20 μm FN lines (Figure 2.3a). Cells aligned on top of the FN-lines and avoided areas, which were stamped by LM. Vinculin staining showed that PCs developed cell-matrix contacts mainly on the vertical FN stripes, but not with the horizontal LM lines (Figure 3.2a, c). Finally, we combined the two micro-structuring techniques and generated surfaces in which 20 μm FN lines were placed under a layer of LM into which 2 μm diameter holes were incorporated (Figure 2.3b). Strikingly, PCs were able to sense the small regions where FN was exposed through the holes in the LM layer, localized adhesions at these spots, and fully aligned to the FN stripes (Figure 3.2b).

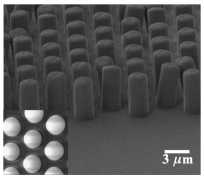
Together, our data showed that PCs adhered preferentially to FN, while avoiding LM areas when FN was present. This suggests that FN deposits in the PC-EC interstitia in capillaries, as previously identified by electron microscopy [28–30], may indeed serve as preferred points for PC attachment to capillaries in the capillary BM.

3.3.2 Highest PC spreading is accompanied by lowest force application on FN substrates of intermediate stiffness.

Next, we investigated whether FN deposits serve as mechanical anchoring points where PCs can sense and respond to variations in mechanical properties of capillaries and, *vice versa*, apply forces to mechanically modulate the extracellular matrix. As a model, PDMS micropillar arrays were generated using the same geometry as described above (Figure 3.3a). By varying the height of the pillars between $3-7$ μm the effective stiffness of the arrays was 11.6, 29.5, 47.2, and 137 kPa, respectively (Figure 3.3b). This range of stiffness resembles that reported for a variety of tissues [44, 45]. The pillar tops were functionalized with FN to which a low amount ($< 1\%$) of Alexa 405/647-labeled FN was added. Such fluorescence labeling allowed monitoring pillar deflections and calculation of cellular traction forces to an accuracy of 0.5 nN using a fluorescence microscope (Figure 3.3c) [35].

3.3 Results

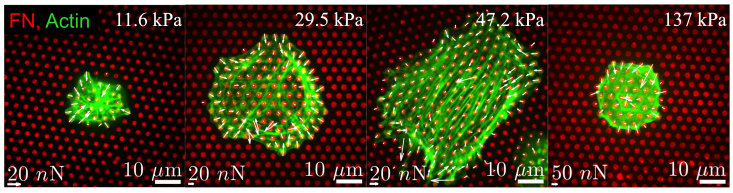
(a)



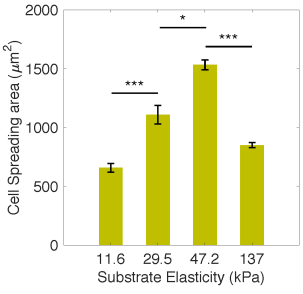
(b)

Stiffness (kPa)	Height (μm)	Diameter (μm)
11.6	6.9	2
29.5	6.1	2.1
47.2	4.1	1.9
137	3.2	2

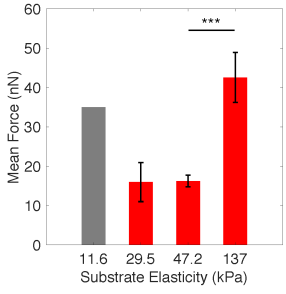
(c)



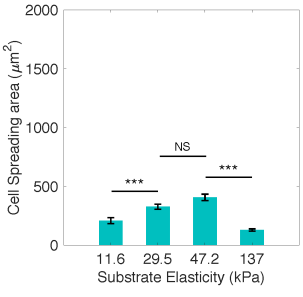
(d)



(e)



(f)



(g)

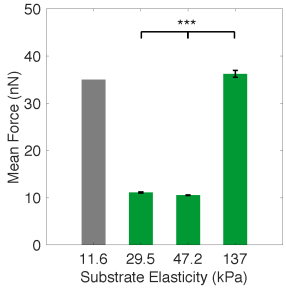


Figure 3.3: PCs placed on PDMS micropillar arrays of different stiffness stamped with FN. (a) An example SEM image of the micropillar array. (b) A table with pillar dimensions per stiffness used for experiments (c) Confocal immunofluorescence images showing PCs (dif31) (actin staining in green) seeded on PDMS micropillar arrays of four different stiffness (from left to right: 11.6, 29.5, 47.2, 137 kPa), functionalized with FN (red). Forces exerted on pillars are depicted with white arrows. (d, f) Average cell spreading area for two different PC lines (d PC dif31, f PC dif43) on PDMS micropillar arrays after 4 hours incubation. (e, g) Average force application for two different PC lines (e PC dif31, g PC dif43) measured after 4 hours incubation on PDMS micropillar arrays. Note that on 11.6 kPa micropillar arrays $\sim$ 25% pillars collapsed due to the apparent high forces, precluding deflection analysis. The gray bar represents the minimal force necessary for the pillar deflection equal to the interpillar distance. Actual average force may be higher. All error bars are s.e.m. derived from five for PC dif31 line and three for PC dif43 line independent experiments performed in minimum two replicates. At least 30 cells were analyzed from each sample. NS, $P>0.05$; *$P<0.05$; **$P<0.005$; ***$P<0.0005$ according to Mann - Whitney test (d, f, g) or ANOVA for (e). See also Figure 3.9.

PCs derived from two independent differentiations (dif31 and dif43) were seeded onto the pillar arrays, fixed after 4 hours and stained for F-actin. Previously we showed that fixation had negligible effect on the analysis of cell spreading and force measurements [42]. PC spreading and force exertion varied with variations in substrate stiffness between 12-137 kPa. Spreading was highest at an intermediate substrate stiffness between 30-47 kPa, resulting in a mean cell area of up to 1500 μm^2, for one PC (dif31) line and $\sim$ 500 μm^2 for another PC (dif43) line. Spreading significantly decreased at both lower and higher substrate stiffness to below 800 μm^2 for PC (dif31) line and $\sim$ 200 μm^2 for PC (dif43) line (Figure 3.3d f). The optimal spreading on intermediate substrate stiffness was paralleled by a low cellular force generation of 10 – 15 nN/pillar for both PC lines (Figure 3.3e,g). On pillars of either lower or higher stiffness, the decrease in spreading was accompanied by significantly higher force generation, reaching 35 – 40 nN/pillar for both PC lines (note: the high mean force value at the lowest substrate stiffness of 11.6 kPa refers to a lower limit since $\sim$ 25% of the pillars collapsed onto each other due to excessive forces under these conditions and could not be analyzed).

This behavior was different from the behavior of fibroblasts. For both SV80 (Figure 3.9a,3.9b) and NIH-3T3 (Figure 3.9c,3.9d) cellular forces gradually increased with substrate stiffness, in line with previous reports

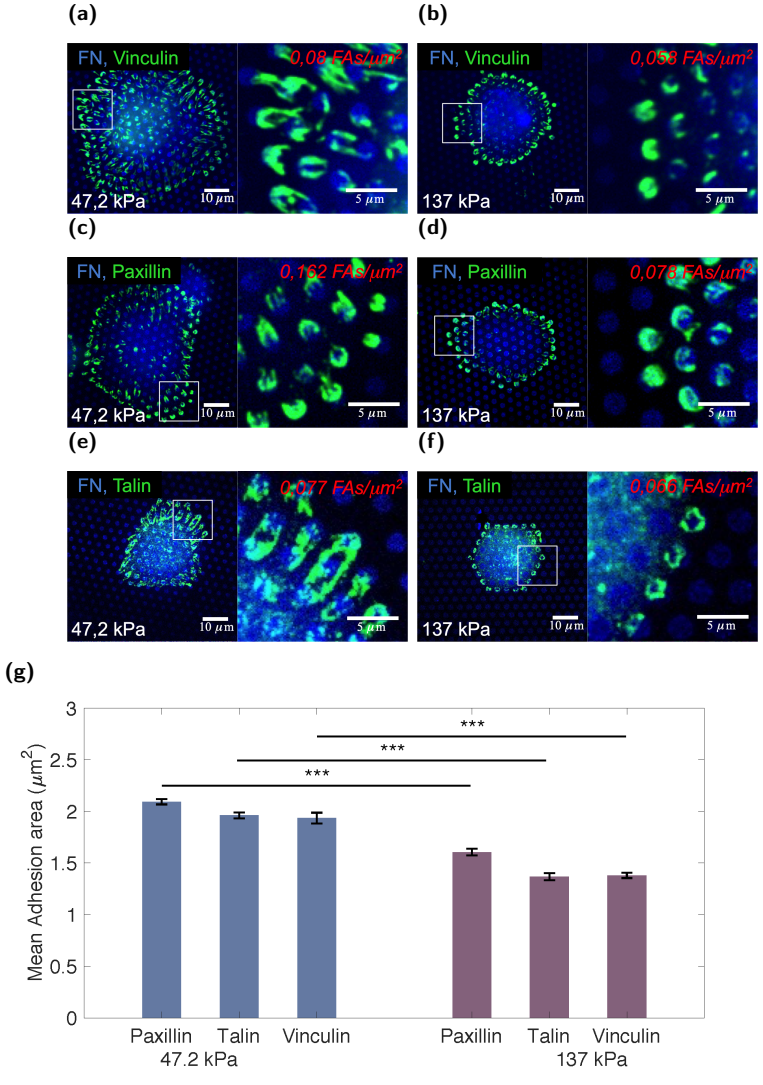
[46, 47]. Across this stiffness range, spreading was largely constant for both fibroblast lines.

We further analyzed how variations in substrate stiffness affected formation and properties of cell-matrix adhesions. Immunofluorescence staining was applied to detect the focal-adhesion proteins vinculin, paxillin and talin on top of the micropillars. As reported earlier, focal-adhesions developed solely on pillars at which cells applied a force [35]. The average cell-matrix adhesion area was determined (Figure 3.4). Remarkably, for all components analyzed the cell matrix adhesion area decreased from $\sim 2\ \mu m^2$ at intermediate stiffness substrates to $< 1.5\ \mu m^2$ at high stiffness substrates (Figure 3.4g). Surprisingly, the correlations between size of the cell-matrix adhesion, the applied cellular force, and the substrate stiffness, as reported for various fibroblast cell lines [35, 48, 49], did not hold for the hiPSC-derived PCs studied here.

Together our findings suggest that PCs bind specifically to FN-patches and sense and respond to changes in stiffness between 12 – 137 kPa. In contrast to fibroblasts for which we observed a continued increase in traction force with increasing substrate stiffness, PCs suppress traction forces and increase cell spreading within 30 – 50 kPa matrix stiffness range, while applying strong traction forces accompanied by limited cell spreading on both soft and stiff substrates.

3.3.3 A switch in PC cytoskeletal organization on stiff substrates.

To further examine what may underlie the increased force application at reduced focal-adhesion area on stiff micropillars, we analyzed the organization of the F-actin cytoskeleton (Figure 3.5a). F-actin was labeled by phalloidin and the 3D-structure of the actin skeleton was imaged for the various substrate stiffness. While straight, elongated F-actin stress fibers were visible on pillars of intermediate stiffness, on stiff micropillars PCs appeared to engulf the pillars and form ring-like F-actin structures that embraced multiple pillars. Notably, all array surfaces, excluding the upper pillar surface, were thoroughly passivated by Pluronic effectively preventing cell attachment. Indeed, the F-actin rings observed below the upper surface of stiff pillars were not supported by cell-matrix adhesions. A 3D-analysis of the location of the different components showed


(a)
(b)
FN, Vinculin
0,08 FAs/μm²
47,2 kPa
FN, Vinculin
0,058 FAs/μm²
137 kPa
10 μm
5 μm
(c)
(d)
FN, Paxillin
0,162 FAs/μm²
47,2 kPa
FN, Paxillin
0,074 FAs/μm²
137 kPa
(e)
(f)
FN, Talin
0,077 FAs/μm²
47,2 kPa
FN, Talin
0,060 FAs/μm²
137 kPa

(g)

Mean Adhesion area (μm²)
3
2.5
2
1.5
1
0.5
0
***
***
***
Paxillin
Talin
Vinculin
47.2 kPa
Paxillin
Talin
Vinculin
137 kPa

Figure 3.4: Cell matrix adhesion area of PCs (dif31) placed on PDMS micropillar arrays of high (137 kPa) and intermediate (47.2kPa) stiffness. (a – f) Confocal immunofluorescence images of PC (dif31) seeded on PDMS micropillar arrays of two different stiffness (137 kPa and 47.2 kPa), functionalized with FN (blue). Cells were stained for vinculin (a,b), paxillin (c,d) and talin (e, f) (green). (g) Average cell matrix adhesion area of PCs cells on PDMS micropillar arrays with 137 kPa stiffness (right) and – 47.2 kPa (left), after 4 hours incubation. All error bars are s.e.m. derived from two independent experiments performed in minimum two replicates. At least 30 cells were analyzed from each sample. NS, $P>0.05$; *$P<0.05$; **$P<0.005$; ***$P<0.0005$ according to Mann - Whitney test. See also Figure 3.10.

that on stiff pillar arrays actin fibers (green) were $\sim 1.5\ \mu m$ below the FN-coated (blue) pillar tops whereas cell matrix adhesion components (vinculin, red) were exclusively localized at the upper surface (Figure 3.5a). By contrast, on pillar arrays of intermediate stiffness, FN, vinculin and F-actin all coincided within $0.8\ \mu m$ at the upper pillar surface.

To analyze the role of cytoskeletal tension and cellular traction force application in relation to the switch in cytoskeletal organization on stiff substrates, PCs were treated with a low concentration ($0.5\ \mu M$) of the ROCK inhibitor Y-27632. ROCK inhibition led to an increased spreading area of PCs on soft as well as stiff substrates, while the cell area on pillars of intermediate stiffness was hardly affected (Figure 3.6a). This indicated that the spreading area was limited by strong cellular contractile forces on soft and stiff substrates. Indeed, traction forces on stiff micropillars, but not on pillars of intermediate stiffness were suppressed by a factor of ~ 1.2 in the presence of Y-27632 (Figure 3.6b). Moreover, the reduction of traction forces caused by ROCK inhibition was accompanied by loss of the ring-like structures surrounding pillars (Figure 3.6c) and reversal of PC cytoskeletal morphology to parallel F-actin stress fibers located on top of the pillar arrays (Figure 3.6d).

3.3.4 Suppression of PC spreading on 2D patterned FN substrates of high and low stiffness

We next investigated whether the switch in cytoskeletal organization and the suppression of cell spreading on stiff micropillars was determined by the 3D topography of the micropillar arrays. For this purpose, 2D micropatterned substrates were designed, which consisted of FN spots within a LM monolayer on a flat surface whose stiffness could be var-

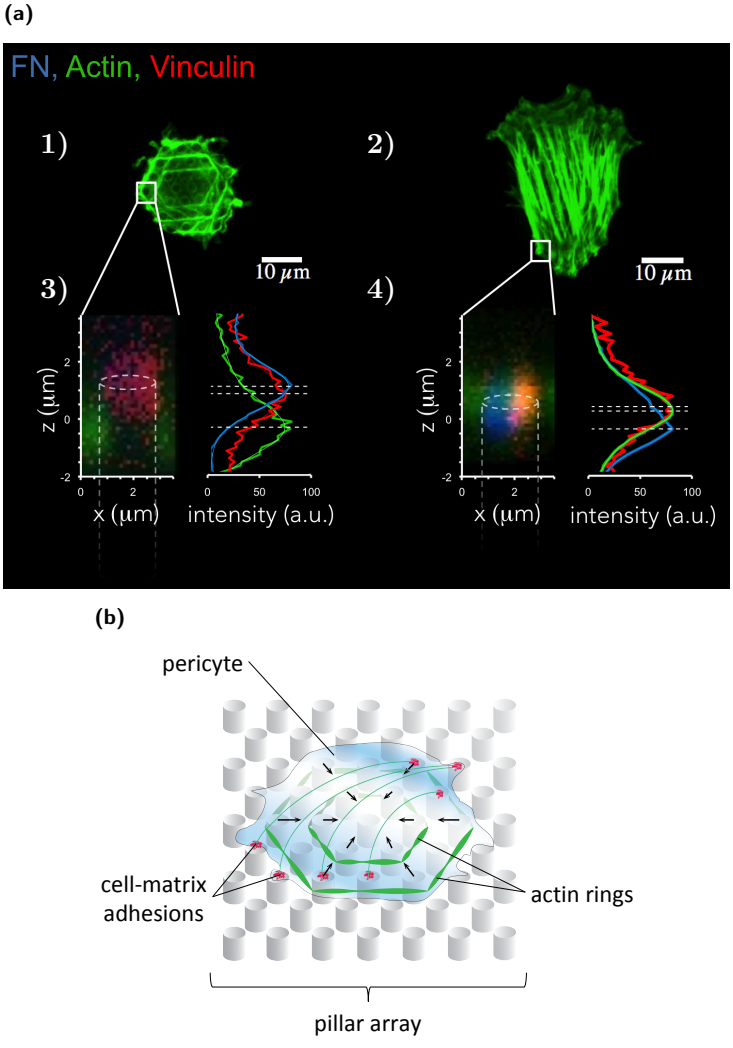
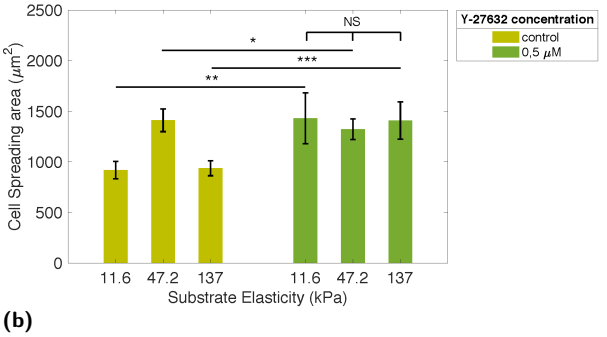
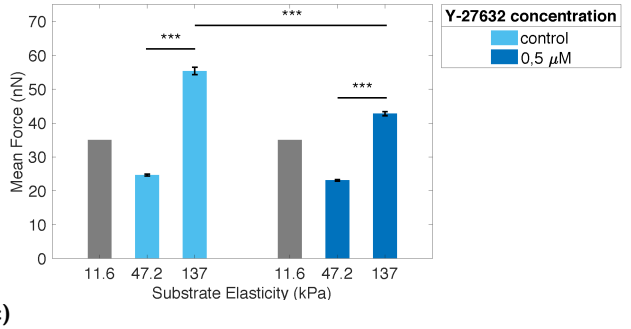


Figure 3.5: Differential actin cytoskeleton organization of PCs. (a) Confocal images of the PCs (dif31) actin cytoskeleton organization on 1) 137 kPa and 2) 47.2 kPa pillars. (a) 3) and 4) on the left – z-projections of the boxed area showing actin (green) and vinculin (red) localization relatively to FN (blue) coated micropillars; on the right – intensity profiles of the z – projections, normalized to 100. (b) Schematic representation of the PCs actin cytoskeleton organization on stiff micropillars. See also Figure 3.11.

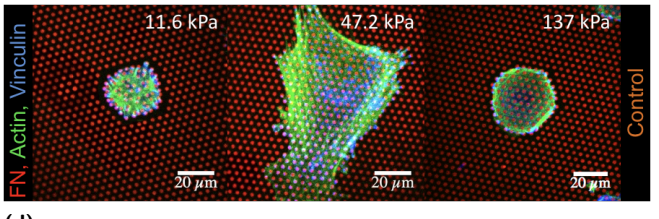
(a)


Cell Spreading area (μm^2)
2500
2000
1500
1000
500
0
NS
*
***
**
11.6
47.2
137
11.6
47.2
137
Substrate Elasticity (kPa)
Y-27632 concentration
control
0,5 μM

(b)


Mean Force (nN)
70
60
50
40
30
20
10
0
***
***
***
11.6
47.2
137
11.6
47.2
137
Substrate Elasticity (kPa)
Y-27632 concentration
control
0,5 μM

(c)


FN, Actin, Vinculin
11.6 kPa
47.2 kPa
137 kPa
Control
20 μm
20 μm
20 μm

(d)

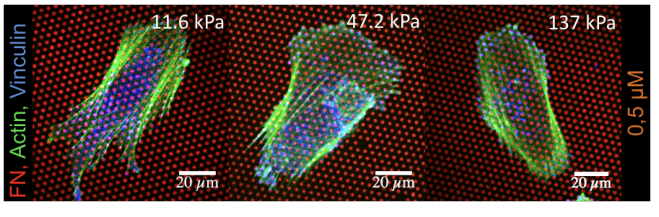

FN, Actin, Vinculin
11.6 kPa
47.2 kPa
137 kPa
0,5 µM
20 μm
20 μm
20 μm

Figure 3.6: Inhibition of ROCK alters PCs spreading on stiff (137 kPa) and soft (11.6 kPa) PDMS micropillar arrays. (a) Average PCs (dif31) spreading area without (left) and with (right) Y-27632 (0.5 μM) after 4 hours incubation. (b) Average PCs (dif31) forces respectively. (c – d) Representative immunofluorescence images of PCs (dif31) spreading and actin cytoskeleton organization (green) on PDMS micropillars (red) without Y-27632 (c) and with 0.5 μM Y-27632 (d) after 4 hours incubation. All error bars are s.e.m. derived from two independent experiments performed in minimum two replicates. At least 30 cells were analyzed from each sample. NS, $P>0.05$; *$P<0.05$; **$P<0.005$; ***$P<0.0005$ according to Mann - Whitney test.

ied, ranging from 3.6 kPa to 250 kPa. As surface we utilized hPAAm hydrogels that provide the same flexibility in substrate micropatterning as PDMS gels, but allow more precise stiffness modulation [37]. Flat PDMS stamps were generated and coated with a layer of LM-111 containing a hexagonal pattern of 2 μm-wide holes of 2 μm spacing, which was covered by a FN monolayer, creating a double layer of LM and FN. This stamp was subsequently inverted onto the hPAAm hydrogels of varying stiffness to print a pattern of FN spots embedded in LM similar to the geometry described in Figure 2.2a (Figure 3.7a). The stiffness of the hPAAm substrate was varied between 3.6 – 250 kPa, a stiffness range within what has been described for blood vessels [50–53].

PCs were seeded onto these flat micropatterned substrates and fixed after 4 hours of incubation. As observed for the pillar arrays the spreading area followed a bell-shaped curve with low spreading at low and high stiffness, and increased spreading at intermediate stiffness. The spreading area doubled to its maximum value at 25 kPa (1200 ± 60 μm^2 on 3.6 kPa *vs* 2500 ± 120 μm^2 on 25 kPa), and decreased at high stiffness (1600 ± 80 μm^2 on 40 kPa) (Figure 3.7c). The cell spreading area on micropatterned hPAAm gels up to 250 kPa was still significantly lower than that observed on a continuous substrate of non-physiological stiffness such as PDMS (1 MPa) and glass (1 GPa) (Figure 3.7d). The preference of PCs to attach to FN over LM was again seen on micropatterned hPAAm substrates. Areas covered with LM were less distorted than areas covered with FN indicating a preferential force application on FN-covered areas (Figure 3.7b). Furthermore, on gels with a stiffness >40kPa, the extracellular matrix coating was disrupted from the surface, further indicating the high forces applied by PCs at high substrate stiffness (Figure 3.7b).

3.3 Results

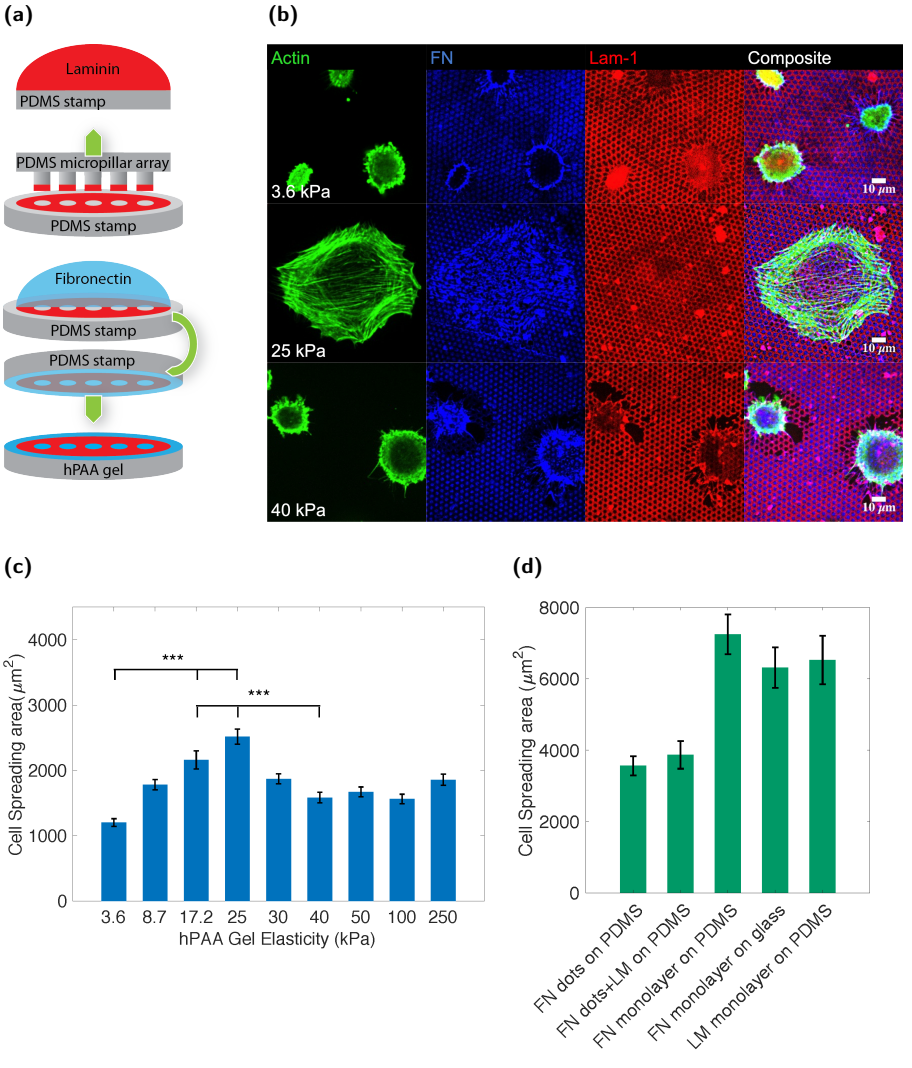

(a)
Laminin
PDMS stamp
PDMS micropillar array
PDMS stamp
Fibronectin
PDMS stamp
PDMS stamp
hPAA gel
(b)
Actin
FN
Lam-1
Composite
3.6 kPa
25 kPa
40 kPa
10 μm
(c)
Cell Spreading area(μm²)
4000
3000
2000
1000
0
***
***
3.6 8.7 17.2 25 30 40 50 100 250
hPAA Gel Elasticity (kPa)
(d)
Cell Spreading area (μm²)
8000
6000
4000
2000
0
FN dots on PDMS
FN dots+LM on PDMS
FN monolayer on PDMS
FN monolayer on glass
LM monolayer on PDMS

Figure 3.7: PCs (dif31) spreading on hydroxy-PAAm hydrogels of different stiffness. (a) "micro contact printing" scheme of hPAAm hydrogels with FN spots surrounded by LM-111. (b) Representative immunofluorescence images of PCs (dif31) seeded on hydroxy-PAAm hydrogels of 3.6, 25 and 40 kPa stiffness (from top to bottom) (c) Average PCs (dif31) spreading area on a palette of hydroxy-PAAm hydrogels with different stiffness and FN&LM stamping. (d) PCs (dif31) spreading on PDMS flat surfaces stamped with: 1) FN dots, 2) FN dots surrounded by LM-111, 3) FN monolayer, 4) LM-111 monolayer; and glass coated with FN monolayer. All surfaces were blocked with BSA 1%. All error bars are s.e.m. derived from three independent experiments performed in minimum two replicates. At least 30 cells were analyzed from each sample. NS, $P>0.05$; *$P<0.05$; **$P<0.005$; ***$P<0.0005$ according to Mann - Whitney test.

3.4 Discussion

PCs have been implicated in regulation of microvessel blood flow and capillary diameter in health and disease. Thus, the mechanical PC-endothelium interaction represents a potential target for therapy. However, it is not understood whether PCs actively and directly participate in control of the vascular diameter, nor is it understood how a putative mechanical connection between PCs and ECs is regulated. N-cadherin mediated binding of PCs to ECs is important during angiogenesis [6], yet N-cadherin expression by ECs is down-regulated with vessel maturation and BM formation [24, 25]. Therefore, adhesion to the BM represents the most likely connection between PCs and ECs in mature, resting capillaries. The BM has a complex composition. Earlier studies pointed to a particular role for small FN-deposits embedded in the LM-rich BM for PC adhesion [28].

Our results support the role of FN deposits in PC interaction with the BM. By modeling FN deposits and their mechanical properties in different ways, we show that PCs have a strong preference towards FN over LM. PCs organize their cell-matrix adhesions mainly on FN while avoiding LM. PCs are guided by thin stripes of FN dots embedded in a LM layer. Interestingly, in the BM of tumor capillaries, FN is frequently over-expressed and is not organized as small distributed patches, but as a thick homogeneous layer [54]. This has been shown to be accompanied by a loose association between PCs and ECs, the opening of spaces separating the two cell types, and the formation of long PC protrusions into the tumor parenchyma, all resulting in wide, leaky microvessels

[55]. Similar effects were reported in the complete absence of FN [21]. Nevertheless, PCs can also leave ECs in injury or normal development conditions and act as progenitor/stem cells [30, 56–58]. Notably, in PC-EC co-cultures, FN expression was found up-regulated in ECs, yet down-regulated in PCs [21], implying that FN in the capillary BM originates mainly from ECs. Hence, it is conceivable that a tight cross talk between ECs and PCs exists, which orchestrates the formation of a LM-rich BM containing small FN deposits. Altogether, our work and the previous findings point to a critical role for the organization of FN deposits in the LM-rich BM for PC adhesion and microvascular function.

Our data provide evidence that capillary FN deposits can serve as points for PC mechanosensing and mechanotransduction. PCs respond to the variation in FN-patterned substrate stiffness with changes in force application, spreading, and cell-matrix adhesions size. PCs show optimal spreading on intermediate (20 – 40 kPa) substrate stiffness, whereas the spreading area was suppressed on both soft and stiff, which is paralleled by an increased size of cell-matrix adhesions on intermediate stiffness substrates. Such mechanoresponsive behavior aligns with the "molecular-clutch hypothesis" [59], which assumes that a response to mechanical cues decreases below or above an optimal rigidity by an increase in the molecular unbinding rate. The increased unbinding would result in lower cell forces, smaller cell substrate adhesions and an ineffective cell spreading on very soft and very rigid matrices. The molecular-clutch model faithfully describes the mechanoresponse of neuronal growth-cones and glioma cells [59–61]. Remarkably, we find that forces applied by PCs on intermediate stiffness substrates are lower than on soft or stiff substrates, which differs from earlier observations with other, in particular fibroblastic, cell types [62][63]. Our own direct comparison with human and mouse fibroblasts where cellular traction forces gradually increase with increasing substrate stiffness corroborate those findings. Another prediction of the molecular-clutch model is the cellular response to suppression of myosin activity [59]. Indeed, we observe that mild ROCK inhibition, which would attenuate force generation, improves PC spreading on stiff and soft substrates.

The high forces and small spreading area observed for PCs on stiff micropillar arrays were accompanied by a dramatic change in cytoskeletal F-actin organization. In comparison to the linear organization of stress fibers on intermediate stiffness pillars, PCs formed circular F-actin rings

surrounding very stiff micropillar arrays. Cell-matrix adhesions assembled on the FN-coated surface of such pillar arrays, but the actin-ring structures encircled multiple pillars below the pillar tops. We hypothesize that such engulfing through ring-like F-actin cytoskeleton organization could represent a cell adaptation process towards the "frictional slippage" regime earlier described [64], allowing PCs to increase forces on substrates outside their optimal rigidity. In line with this hypothesis, we found that mild ROCK inhibition reversed the change in F-actin cytoskeletal organization back to an organization as observed on intermediate stiffness.

The use of flat hPAAm hydrogels instead of PDMS micropillars, allowed us to eliminate the effect of substrate topography while keeping the opportunity to tune the substrate stiffness. On flat 2D micropatterned surfaces the PC behavior was similar to that found on micropillar arrays: PCs showed optimal spreading on intermediate stiffness substrates. Yet, we noticed that the optimal stiffness for PC spreading differed on hPAAm hydrogels (25 kPa) to that on PDMS micropillar arrays (47 kPa). This small, yet significant, difference is likely due to the 2D versus 3D geometry of the substrates, the tightly restricted area for cell-matrix adhesions on the micropillar arrays, and/or the absence of LM in the micropillar model system. Interestingly, for micropatterned hydrogel substrates, the stiffness range of 15 – 25 kPa supporting optimal PC spreading was close to that determined by atomic-force microscopy for ECs and smooth muscle cells [44, 45], indicating that this stiffness range represents a response in a physiologically relevant stiffness regime. Behavior of PCs observed in this study may provide an insight on the way PCs distinguish deviations of the microvessel stiffness from the normal and react by increasing contractile forces. A limitation of this study is the unavailability of *ex vivo* isolated mid-capillary PCs. We derived CD31– PCs from a hiPSC line and used different differentiations. Robustness of PC behavior described here could be further increased using PCs derived from multiple independent hiPSC lines in future studies.

Taken together, our study shows that PCs strongly prefer FN over LM, that PCs recognize and align to FN dots within a LM substrate, that PCs apply forces to FN deposits, and that PCs are able to sense variations in mechanical properties of the FN deposits and respond to this by changing traction force, cell spreading area, and the size of cell matrix adhesions. Our findings also point to a mechanoresponsive beha-

vior of PCs that significantly differs from that observed for fibroblasts and other cell types. Our findings support a role for FN deposits in the BM as adhesion points for mechanoregulation of the microvasculature by PCs. Our *in vitro* model system of micropillar arrays/micropatterened hydrogels in combination with hiPSC derived-PCs described earlier [32, 65] can be a valuable test-bed to study the mechanisms of PC force regulation in physiology and pathology under well controlled conditions and may serve as a model for drug discovery efforts.

3.5 Apendix

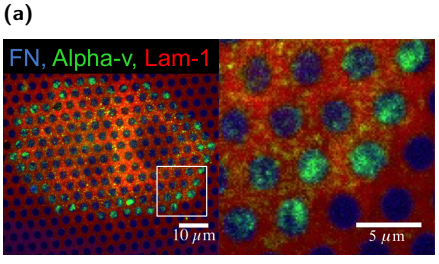


Figure 3.8: PCs (dif31) placed on a pattern of FN and LM-111 depicted in (Fig. 2.2a) with alpha-v integrin labeled (green). Related to Figure 3.1.

3.5 Apendix

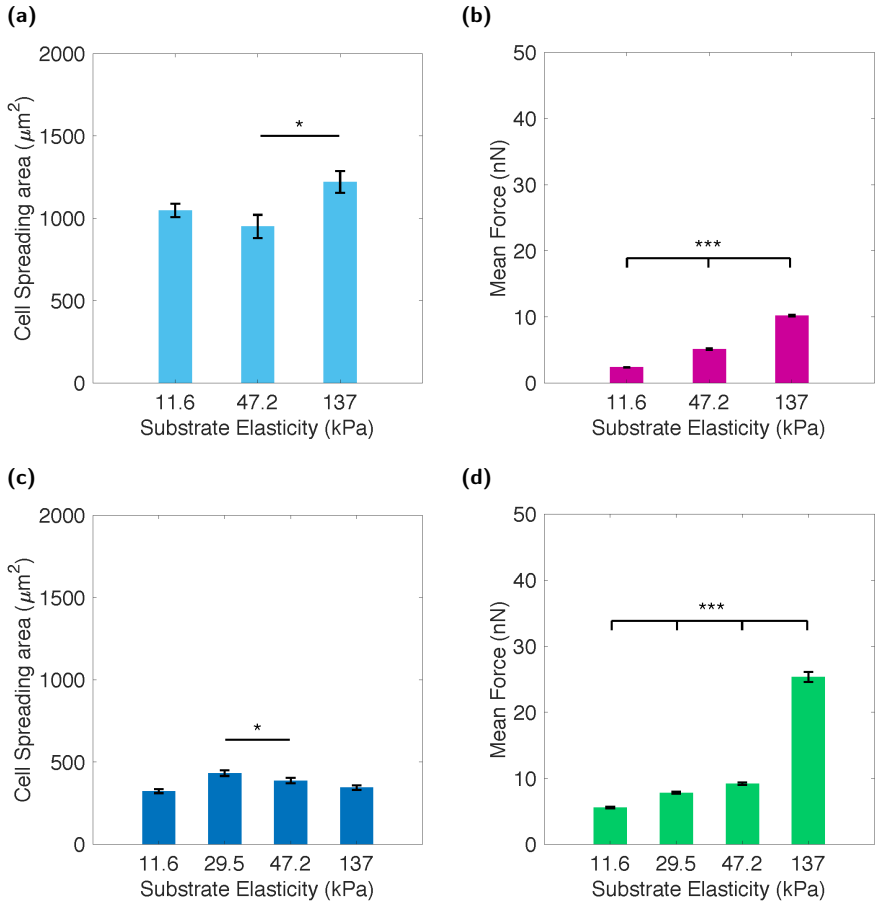


Figure 3.9: SV80 and 3T3 cells average spreading area and force application. (a) SV80 average cell spreading area on PDMS micropillar arrays after 4 hours incubation. (b) SV80 average force application measured after 4 hours incubation. (c) 3T3 average cell spreading area on PDMS micropillar arrays functionalized with FN after 4 hours incubation. (d) 3T3 average force application measured after 4 hours incubation. All error bars are s.e.m. derived from three independent experiments performed in minimum two replicates. At least 30 cells were analyzed from each sample. NS, $P>0.05$; *$P<0.05$; **$P<0.005$; ***$P<0.0005$ according to Mann - Whitney test. Related to Figure 3.3.

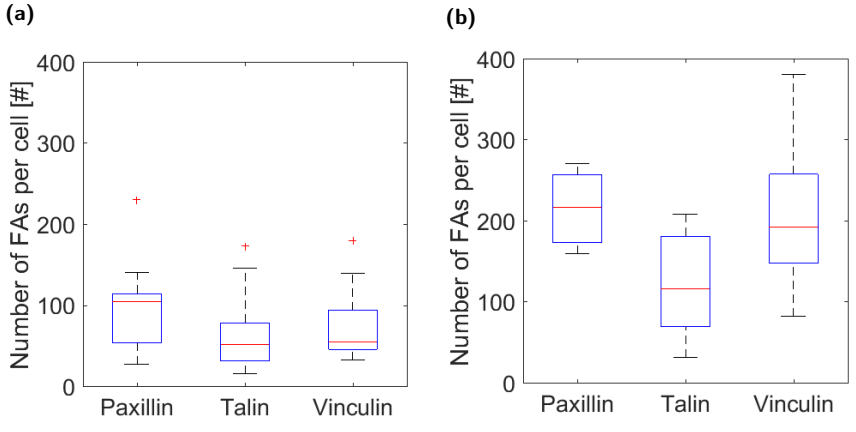


Figure 3.10: (a) Number of FAs per cell for PCs seeded on 137 kPA micropillar arrays stamped with FN. (b) Number of FAs per cell for PCs seeded on 47,2 kPA micropillar array stamped with FN. Results were obtained after 4 hours incubation from three independent experiments performed in minimum two replicates. At least 30 cells were analyzed from each sample. NS, $P>0.05$; *$P<0.05$; **$P<0.005$; ***$P<0.0005$ according to Mann - Whitney test. Related to Figure 3.4.

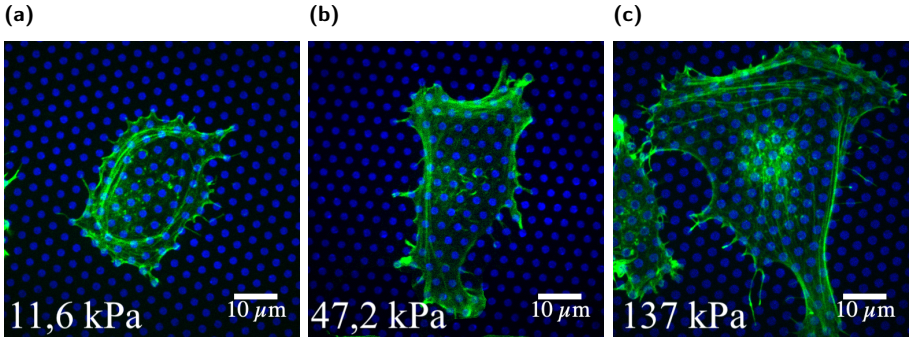


Figure 3.11: Representative images of the actin cytoskeleton organization of SV80 cells (green) seeded on PDMS micropillar arrays of various stiffness stamped with FN (blue): (a) 11,6 kPa, (b) 47,2 kPa, (c) 137 kPa. Related to Figure 3.5.

Bibliography

[1] K.W. Zimmermann. « Der feinere bau der blutcapillares ». In: *Z. Anat. Entwickl.* 68 (1923), pp. 3–109.

[2] Annika Armulik, Guillem Genové and Christer Betsholtz. « Pericytes: developmental, physiological, and pathological perspectives, problems, and promises. » In: *Dev. Cell* 21.2 (2011), pp. 193–215. ISSN: 1534-5807.

[3] Dore-Duffy Paula et al. « CNS microvascular pericytes exhibit multipotential stem cell activity. » In: *J. Cereb. Blood Flow Metab.* 26.5 (2006), pp. 613–24. ISSN: 0271-678X.

[4] Robert D Bell et al. « Pericytes control key neurovascular functions and neuronal phenotype in the adult brain and during brain aging. » In: *Neuron* 68.3 (2010), pp. 409–27. ISSN: 0896-6273.

[5] Annika Armulik et al. « Pericytes regulate the blood-brain barrier. » In: *Nature* 468.7323 (2010), pp. 557–61. ISSN: 0028-0836.

[6] Holger Gerhardt, Hartwig Wolburg and Christoph Redies. « N-cadherin mediates pericytic-endothelial interaction during brain angiogenesis in the chicken ». In: *Dev Dyn* 218.3 (2000), pp. 472–479. ISSN: 1097-0177.

[7] Robert A Hill et al. « Regional Blood Flow in the Normal and Ischemic Brain Is Controlled by Arteriolar Smooth Muscle Cell Contractility and Not by Capillary Pericytes. » In: *Neuron* 87.1 (2015), pp. 95–110. ISSN: 0896-6273.

[8] Anusha Mishra et al. « Astrocytes mediate neurovascular signaling to capillary pericytes but not to arterioles. » In: *Nat. Neurosci.* 19.12 (2016), pp. 1619–1627. ISSN: 1097-6256.

[9] YJ Le Beux and J Willemot. « Actin- and myosin-like filaments in rat brain pericytes. » In: *Anat. Rec.* 190.4 (1978), pp. 811–26. ISSN: 0003-276X.

[10] IH Wallow and B Burnside. « Actin filaments in retinal pericytes and endothelial cells. » In: *Invest. Ophthalmol. Vis. Sci.* 19.12 (1980), pp. 1433–41. ISSN: 0146-0404.

[11] NC Joyce, MF Haire and GE Palade. « Contractile proteins in pericytes. I. Immunoperoxidase localization of tropomyosin. » In: *J. Cell Biol.* 100.5 (1985), pp. 1379–86. ISSN: 0021-9525.

[12] NC Joyce, MF Haire and GE Palade. « Contractile proteins in pericytes. II. Immunocytochemical evidence for the presence of two isomyosins in graded concentrations. » In: *J. Cell Biol.* 100.5 (1985), pp. 1387–95. ISSN: 0021-9525.

[13] Nicola B Hamilton, David Attwell and Catherine N Hall. « Pericyte-mediated regulation of capillary diameter: a component of neurovascular coupling in health and disease ». In: *Frontiers in neuroenergetics* 2 (2010).

[14] Claire M Peppiatt et al. « Bidirectional control of CNS capillary diameter by pericytes. » In: *Nature* 443.7112 (2006), pp. 700–4. ISSN: 0028-0836.

[15] Kassandra Kisler et al. « Pericyte degeneration leads to neurovascular uncoupling and limits oxygen supply to brain ». Czech. In: *Nat Neurosci* 20.3 (2017), pp. 406–416. ISSN: 1097-6256.

[16] Catherine N Hall et al. « Capillary pericytes regulate cerebral blood flow in health and disease. » In: *Nature* 508.7494 (2014), pp. 55–60. ISSN: 0028-0836.

[17] Muge Yemisci et al. « Pericyte contraction induced by oxidative-nitrative stress impairs capillary reflow despite successful opening of an occluded cerebral artery. » In: *Nat. Med.* 15.9 (2009), pp. 1031–7. ISSN: 1078-8956.

[18] Anthony P Hall. « Review of the pericyte during angiogenesis and its role in cancer and diabetic retinopathy. » In: *Toxicol Pathol* 34.6 (2006), pp. 763–75. ISSN: 0192-6233.

[19] Katsukuni Fujimoto. « Pericyte-endothelial gap junctions in developing rat cerebral capillaries: A fine structural study ». In: *Anatomical Rec* 242.4 (1995), pp. 562–565. ISSN: 1097-0185.

[20] Emmanuelle Tillet et al. « N-cadherin deficiency impairs pericyte recruitment, and not endothelial differentiation or sprouting, in embryonic stem cell-derived angiogenesis. » In: 310.2 (2005), pp. 392–400. ISSN: 0014-4827.

[21] Amber N Stratman et al. « Pericyte recruitment during vasculogenic tube assembly stimulates endothelial basement membrane matrix formation. » In: *Blood* 114.24 (2009), pp. 5091–101. ISSN: 0006-4971.

[22] Ombretta Salvucci et al. « EphrinB reverse signaling contributes to endothelial and mural cell assembly into vascular structures ». In: *Blood* 114.8 (2009), pp. 1707–1716. ISSN: 0006-4971.

[23] Ombretta Salvucci and Giovanna Tosato. *Essential Roles of EphB Receptors and EphrinB Ligands in Endothelial Cell Function and Angiogenesis*. Vol. 114. sciencedirect, 2012. ISBN: 9780123865038.

[24] Deana M Ferreri et al. « N-cadherin levels in endothelial cells are regulated by monolayer maturity and p120 availability. » In: 15.4 (2008), pp. 333–49. ISSN: 1541-9061.

[25] H Gerhardt et al. « N-cadherin expression in endothelial cells during early angiogenesis in the eye and brain of the chicken: relation to blood-retina and blood-brain barrier development ». In: *Eur J Neurosci* 11.4 (1999), pp. 1191–1201. ISSN: 1460-9568.

[26] Lema F Yousif, Jacopo Russo and Lydia Sorokin. « Laminin isoforms in endothelial and perivascular basement membranes ». In: 7.1 (2013), p. 101110. ISSN: 1933-6918.

[27] Willi Halfter et al. « The bi-functional organization of human basement membranes. » In: *PLoS ONE* 8.7 (2013), e67660. ISSN: 1932-6203.

[28] PJ Courtoy and J Boyles. « Fibronectin in the microvasculature: localization in the pericyte-endothelial interstitium. » In: *J. Ultrastruct. Res.* 83.3 (1983), pp. 258–73. ISSN: 0022-5320.

[29] Annika Armulik, Alexandra Abramsson and Christer Betsholtz. « Endothelial-pericyte interactions. » In: *Circ. Res.* 97.6 (2005), pp. 512–23. ISSN: 0009-7330.

[30] Ethan A Winkler, Robert D Bell and Berislav V Zlokovic. « Central nervous system pericytes in health and disease ». In: *Nature Neuroscience* 14.11 (2011), pp. 1398–1405. ISSN: 1097-6256.

[31] Valeria V Orlova et al. « Functionality of Endothelial Cells and Pericytes From Human Pluripotent Stem Cells Demonstrated in Cultured Vascular Plexus and Zebrafish Xenografts ». In: *Arteriosclerosis Thrombosis Vasc Biology* 34.1 (2014), pp. 177–186. ISSN: 1079-5642.

[32] Valeria V Orlova et al. « Generation, expansion and functional analysis of endothelial cells and pericytes derived from human pluripotent stem cells. » In: *Nat Protoc* 9.6 (2014), pp. 1514–31. ISSN: 1750-2799.

[33] Hayri Balcioglu et al. « Substrate rigidity modulates the association between traction forces and molecular composition of cell matrix adhesions ». In: *in preparation* ().

[34] Ravi A Desai, Natalia M Rodriguez and Christopher S Chen. « Stamp-off" to micropattern sparse, multicomponent features. » In: *Methods in Cell Biology* 119 (2014), pp. 3–16. ISSN: 0091-679X.

[35] Hedde van Hoorn et al. « The Nanoscale Architecture of Force-Bearing Focal Adhesions ». In: *Nano letters* 14 (2014), pp. 4257–4262.

[36] Olivia du Roure et al. « Force mapping in epithelial cell migration. » In: *Proc. Natl. Acad. Sci. U.S.A.* 102.7 (2005), pp. 2390–5. ISSN: 0027-8424.

[37] Thomas Grevesse et al. « A simple route to functionalize polyacrylamide hydrogels for the independent tuning of mechanotransduction cues. » In: *Lab on a Chip* 13.5 (2013), pp. 777–80. ISSN: 1473-0189.

[38] Xue Jiang et al. « Cell Growth in Response to Mechanical Stiffness is Affected by Neuron- Astroglia Interactions ». In: *The Open Neuroscience Journal* 1.1 (2007), pp. 7–14. ISSN: 1874-0820.

[39] Thomas Grevesse et al. « Opposite rheological properties of neuronal microcompartments predict axonal vulnerability in brain injury ». In: *Scientific Reports* 5 (2015), p. 9475.

[40] John L Tan et al. « Cells lying on a bed of microneedles: an approach to isolate mechanical force. » In: *Proc. Natl. Acad. Sci. U.S.A.* 100.4 (2003), pp. 1484–9. ISSN: 0027-8424.

[41] Jianping Fu et al. « Mechanical regulation of cell function with geometrically modulated elastomeric substrates. » In: *Nat. Methods* 7.9 (2010), pp. 733–6. ISSN: 1548-7091.

[42] HE Balcioglu et al. « The integrin expression profile modulates orientation and dynamics of force transmission at cell-matrix adhesions ». In: *J Cell Sci* 128.7 (2015), pp. 1316–1326. ISSN: 0021-9533.

[43] C. Dambrot et al. « Polycistronic lentivirus induced pluripotent stem cells from skin biopsies after long term storage, blood outgrowth endothelial cells and cells from milk teeth ». In: *Differentiation* 85.3 (2013), pp. 101–109. ISSN: 0301-4681.

[44] Takayuki Okamoto et al. « Gap junction-mediated regulation of endothelial cellular stiffness ». In: *Sci Reports* 7.1 (2017), p. 6134. ISSN: 2045-2322.

[45] Zhongkui Hong et al. « Vascular Smooth Muscle Cell Stiffness and Adhesion to Collagen I Modified by Vasoactive Agonists ». In: *Plos One* 10.3 (2015), e0119533.

[46] Tony Yeung et al. « Effects of substrate stiffness on cell morphology, cytoskeletal structure, and adhesion. » In: *Cell Motil. Cytoskeleton* 60.1 (2005), pp. 24–34. ISSN: 0886-1544.

[47] RJ Pelham and Yl Wang. « Cell locomotion and focal adhesions are regulated by substrate flexibility. » In: *Proc. Natl. Acad. Sci. U.S.A.* 94.25 (1997), pp. 13661–5. ISSN: 0027-8424.

[48] Nathalie Q Balaban et al. « Force and focal adhesion assembly: a close relationship studied using elastic micropatterned substrates ». In: *Nature Cell Biology* 3.5 (2001), pp. 466–472. ISSN: 1465-7392.

[49] Léa Trichet et al. « Evidence of a large-scale mechanosensing mechanism for cellular adaptation to substrate stiffness ». In: *Proc National Acad Sci* 109.18 (2012), pp. 6933–6938. ISSN: 0027-8424.

[50] Colin Grant and Peter Twigg. « Pseudostatic and Dynamic Nanomechanics of the Tunica Adventitia in Elastic Arteries Using Atomic Force Microscopy ». In: *Acs Nano* 7.1 (2013), pp. 456–464. ISSN: 1936-0851.

[51] M Balooch et al. « Viscoelastic properties of demineralized human dentin measured in water with atomic force microscope (AFM)-based indentation. » In: *J. Biomed. Mater. Res.* 40.4 (1998), pp. 539–44. ISSN: 0021-9304.

[52] Ali Hemmasizadeh, Michael Autieri and Kurosh Darvish. « Multilayer material properties of aorta determined from nanoindentation tests. » In: *J Mech Behav Biomed Mater* 15 (2012), pp. 199–207. ISSN: 1878-0180.

[53] Julie C Kohn, Marsha C Lampi and Reinhart-King, Cynthia A. « Age-related vascular stiffening: causes and consequences ». In: *Frontiers In Genetics* 06 (2015). ISSN: 1664-8021.

[54] Xiaoming Zhou et al. « Fibronectin fibrillogenesis regulates three-dimensional neovessel formation ». In: 22.9 (2008), pp. 1231–1243. ISSN: 0890-9369.

[55] S Morikawa et al. « Abnormalities in pericytes on blood vessels and endothelial sprouts in tumors ». In: *The American Journal of Pathology* (2002).

[56] Sophie Dulauroy et al. « Lineage tracing and genetic ablation of ADAM12+ perivascular cells identify a major source of profibrotic cells during acute tissue injury ». In: *Nat Med* 18.8 (2012), p. 1262. ISSN: 1546-170X.

[57] A. Dellavalle et al. « Pericytes resident in postnatal skeletal muscle differentiate into muscle fibres and generate satellite cells ». In: *Nat Commun* 2.1 (2011), p. 499. ISSN: 2041-1723.

[58] Jifan Feng et al. « Dual origin of mesenchymal stem cells contributing to organ growth and repair ». In: *Proc National Acad Sci* 108.16 (2011), pp. 6503–6508. ISSN: 0027-8424.

[59] Elosegui-Artola Alberto, Xavier Trepat and Roca-Cusachs Pere. « Control of Mechanotransduction by Molecular Clutch Dynamics ». In: *Trends Cell Biol* (0). ISSN: 0962-8924.

[60] CE Chan and DJ Odde. « Traction dynamics of filopodia on compliant substrates ». In: *Science* (2008). ISSN: 0036-8075.

[61] BL Bangasser et al. « Shifting the optimal stiffness for cell migration ». In: *Nature* (2017). ISSN: 2041-1723.

[62] Marion Ghibaudo et al. « Traction forces and rigidity sensing regulate cell functions ». In: 4.9 (2008), pp. 1836–1843. ISSN: 1744-683X.

[63] Sangyoon J Han et al. « Decoupling substrate stiffness, spread area, and micropost density: a close spatial relationship between traction forces and focal adhesions. » In: *Biophys. J.* 103.4 (2012), pp. 640–8. ISSN: 0006-3495.

[64] A Elosegui-Artola et al. « Mechanical regulation of a molecular clutch defines force transmission and transduction in response to matrix rigidity ». In: *Nature cell biology* (2016). ISSN: 1465-7392.

[65] Ayelet Dar et al. « Multipotent Vasculogenic Pericytes From Human Pluripotent Stem Cells Promote Recovery of Murine Ischemic Limb ». In: 125.1 (2012), pp. 87–99. ISSN: 0009-7322.

BIBLIOGRAPHY

Chapter 4

Insights into the regulation of α-smooth muscle actin expression in pericytes [1]

abstract

Depending on the location along the microvascular tree pericytes (PCs) have been divided into three subgroups: pre-capillary, mid-capillary and post-capillary PCs. Mid-capillary PCs completely lack α-SMA, while pre- and post-capillary PCs show a gradient in the α-SMA expression levels from low, next to mid-capillaries, to high closer to arterioles and venules where smooth muscle cells (SMCs) come in place. How this gradient is conditioned in the resting vasculature remains unclear.

In this chapter we assessed aspects of the α-SMA expression control in PCs by means of mechanical signals. We investigated whether such parameters like vessel diameter, basement membrane (BM) composition and stiffness can have an effect on the α-SMA recruitment to stress fibers in mural cells, as well as in SMCs. Automatic image data analysis approach was utilized to obtain uncompromised data on the α-SMA fiber formation with a single cell resolution.

Our results showed that α-SMA expression in PCs can be mainly affected by the presence of fibronectin (FN) deposits in the BM of microvessels and less by the stiffness or vessel diameter. In the mean time, SMCs are more dependent on the rigidity and allowed area for spreading

1. This chapter is based on: O. Iendaltseva, V.V. Orlova, C.L. Mummery, E. H. J. Danen and T. Schmidt, Insights into the Regulation of α-Smooth Muscle Actin Expression in Pericytes, *In preparation*

then on the FN arrangement. Notably, PCs could adapt their α-SMA cytoskeletal recruitment in response to the ECM properties. These findings may further help to unveil processes behind maintaining α-SMA expression gradient in PCs and can be used to keep PCs from obtaining contractile phenotype in cell culture.

4.1 Introduction

The important process of the exchange of gases, solvents and solutes between tissues and blood happens in the capillary beds of the circulatory system. These beds consist of the smallest vessels – arterioles, capillaries, and venules, which penetrate all organs and tissues of the human body. From them, capillaries can be further divided into three types: pre-capillaries, mid-capillaries, and post-capillaries [1] (Fig. 4.1). In some tissues arterioles give rise to metarterioles that are either directly connected to venules, or precede capillaries. The mean diameter of microvessels in this region changes from the $\sim$ 30 μm arterioles and $\sim$ 15 μm metarterioles down to $\sim$ 8 μm in diameter mid-capillaries and back up to the $\sim$ 20 μm venules [2]. Vessel tubes are formed by endothelial cells (ECs), while pericytes (PCs) and smooth muscle cells (SMCs) – the mural cells of blood microvessels, localize to the abluminal surface of these tubes. Depending on the location and morphology, PCs have been divided into three subgroups: pre-capillary, mid-capillary, and post-capillary PCs [3]. Mid-capillary PCs have the most prominent difference from the SMCs. They completely lack α-smooth muscle actin (SMA) expression, while SMCs are α-SMA positive. They have long cytoplasmic processes along the vessel with thin, perpendicular to the primary branches, secondary processes, which partially encircle the vessel in contrast to the band-like circumferential phenotype of SMCs (Fig. 4.1). Because of this clear polarity, PCs located on mid-capillaries have been defined as "true" or "approved" PCs [1, 4], while, pre- and post-capillary mural cells – as transitional PCs [3].

Transitional PCs are morphologically heterogeneous and, depending on their location, display a smooth shift from the mid-capillary PC phenotype to SMC. Besides variations in morphology, transitional PCs show a gradient in the α-SMA expression levels from low (close to the mid-capillaries) to high (next to the arterioles or venules) [4, 5] (Fig. 4.1). Due to this gradient, transitional PCs are sometimes mistakenly determined as pre- and post- capillary SMCs [6]. Indeed, distinguishing between PCs, their types and SMCs is challenging, especially in case of *in vitro* cell cultures. There is no clear "border" and no single marker that would be specific for all PCs or any subtype. Yet, the main feature that marks all types of PCs out of SMCs is their ability to support angiogenesis [7]. Recently it has been shown that human pluripotent stem cell (hPSC)-derived immature PC can be specified to either mid-capillary or pre-

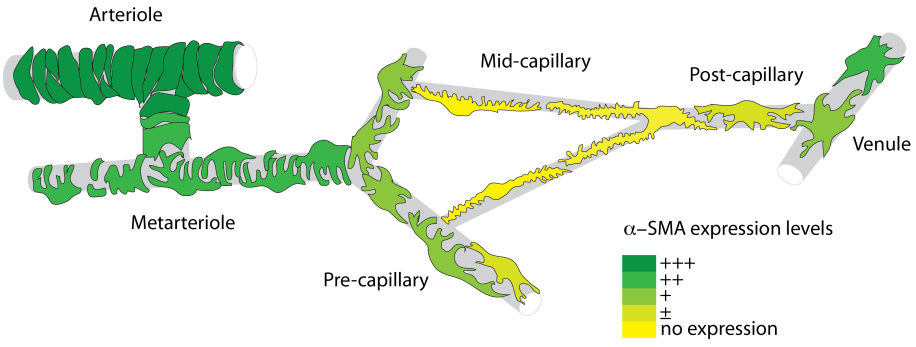


Figure 4.1: Schematic representation of the heterogeneous expression of α-SMA in pericytes of pre-, mid- and post-capillaries (adapted from [4])

capillary PC types by treatment with different combinations of growth factors (GF) [7]. Cell culture media containing platelet-derived growth factor (PDGF)-BB in combination with transforming growth factor-beta (TGF-β) induces α-SMA and Calponin 1 (CNN1)-negative PCs to up-regulate expression of smooth muscle markers like smooth muscle-specific protein 22 (SM22), α-SMA and CNN1[8, 9]. However, *in vivo* PCs expressing α-SMA and PCs lacking α-SMA can be located next to each other and sometimes even on the vessel of the same branch order [4–6]. This raises the question, how the α-SMA expression gradient is conditioned and maintained in the resting vasculature.

Here we investigated a potential influence of the mechanical aspects, such as vessel stiffness, width and spatial organization of the capillary basement membrane (BM) proteins on the regulation of the α-SMA expression and recruitment to stress fibers in PCs. We used the previously described human induced pluripotent stem cell (hiPSC)-derived PCs as a cell model resembling mid-capillary PCs, lacking α-SMA expression [8, 9]. Quantification of the α-SMA immunostaining intensity and distribution allowed us to asses not only the level of the α-SMA expression, but also the degree of its recruitment to cellular stress fibers. Our findings suggest that: i) besides chemical cues the α-SMA expression gradient in PCs is influenced by capillary mechanical properties; ii) FN deposits found in the PC-ECs interstitial layer of the capillary BM [10] may have a major contribution to the conditioning and maintaining of this gradient compared to other mechanical signals.

4.2 Methods

4.2.1 Cell culture

CD31– cells derived from the hiPSC line LUMC06iCTRL-derived (dif31), SV80 human fibroblasts, and HASM human arterial smooth muscle cells (Applied Cell Biology Research Institute, Kirkland, WA) were cultured in Dulbecco's Modified Eagle's Medium (DMEM, Gibco | Thermo Fisher Scientific, USA) supplemented with 10% fetal bovine serum (HyClone, Etten-Leur, The Netherlands), 25 U/ml penicillin and 25 µg/ml streptomycin (Invitrogen/Fisher Scientific). The CD31– cell line was used at passage 7 or 8 and cultured for 3 to 4 days before experiments. For 4 and 24 hours long cell incubation time experiments, cells were seeded at 20,000 cells per sample and for 7 day incubation – at 10,000 cells/sample. Cells were injected directly on top of the substrate area of interest to ensure persistent cell density across experiments. After incubation they were fixed 10' in 4% paraformaldehyde in PBS for further immunostaining. Gelatin and fibronectin (FN) used as cell substrates were obtained from Sigma (g2500 and f1141 respectively).

4.2.2 Immunostaining

Fixed cells were permeabilized for 10' with 0.1% Triton-X in PBS and blocked for 60' with either 1% bovine serum albumin (BSA) (Sigma, a2153), or 1% or 5% goat serum (GS) (Sigma, G6767) in PBS. α-SMA was immunostained, first, with a mouse monoclonal (clone 1A4) primary antibody against α-SMA (Sigma, A2547) in a blocking buffer o/n, followed by 3 washing steps in PBS 10' each under a gentle rocking. Secondly, the Alexa 532 conjugated secondary antibody against mouse IgG (Thermo Fisher Scientific, a11002) was applied in a blocking buffer for 2 hours. The antibody was subsequently removed with 3X 10' in PBS washing steps under rocking. Additionally, F-actin cytoskeleton of cells in a number of experiments was stained with Alexa 647 phalloidin (Thermo Fisher Scientific, a22287) of a 1:1000 concentration in PBS.

4.2.3 Microscopy

Confocal imaging was performed on a home-built setup based on an Axiovert200 microscope body (Zeiss), spinning disk unit (CSU-X1, Yokogawa) and an emCCD camera (iXon 897, Andor). IQ-software

enabled setup-control and data acquisition. Lasers of 405 nm (CrystaLaser), 488 nm (Coherent), 514 nm, 561 nm (Cobolt) and 642 nm (Spectra Physics) wavelength were coupled into the CSU via polarization maintaining single-mode fiber. Spacers on the sides of micropillar arrays allowed placing them upside down onto #0 coverslips (Menzel Glaser) with adhered cells facing down. This approach ensured reproducible cell observation within the limited working distance of a high-NA objective on an inverted microscope. For PDMS or glass 2D assays parafilm spacers were made directly on top of the glass coverslips.

4.2.4 Image analysis

The level of the α-SMA expression and the degree of it's recruitment to cellular stress fibers was assessed with the help of quantification of the α-SMA staining intensity and distribution. The quantification was done automatically with the help of a particularly designed Matlab script, comprising a call to FIJI/ImageJ (NIH, Maryland, USA) image analysis software plug-in – OrientationJ (EPFL, Switzerland)[11]. The acquired images were split into the original channels and the plug-in was used to find the orientation within the local features of the α-SMA staining distribution in the corresponding channel (Example fig. 4.2a, 4.2b). This was done by computing the so-called structure tensor for each pixel with the help of a cubic spline interpolation in the sliding over the entire image Gaussian analysis window. This window we have chosen to be 2 pixels in size for images taken with the 40x magnification objective having NA= 1.3 or 1.5 pixels for – 100x magnification and NA= 1.4 objective. The change in the window size is reasoned by the difference in the minimal diameter of the fluorophore airy pattern that can be acquired with NA= 1.3 and NA= 1.4 objectives. From the structure tensor the "coherency" value (from 0 to 1) as a ratio between the difference and the sum of the maximum and minimum tensor eigenvalues was obtained to distinguish between the isotropic and uniform regions of the image.

The picture coherency map built by the FIJI plug-in (Example fig.4.2c, 4.2d) was further processed in Matlab to find a common coherency background level outside the cell across all images that would characterize uniform regions of the image (Example 3D histograms of the coherency values distribution vs corresponding intensity per pixel for the first cell 4.2e and the second 4.2f). To mask out the cell we used an image channel of the cell F-actin. The global threshold for the channel was found

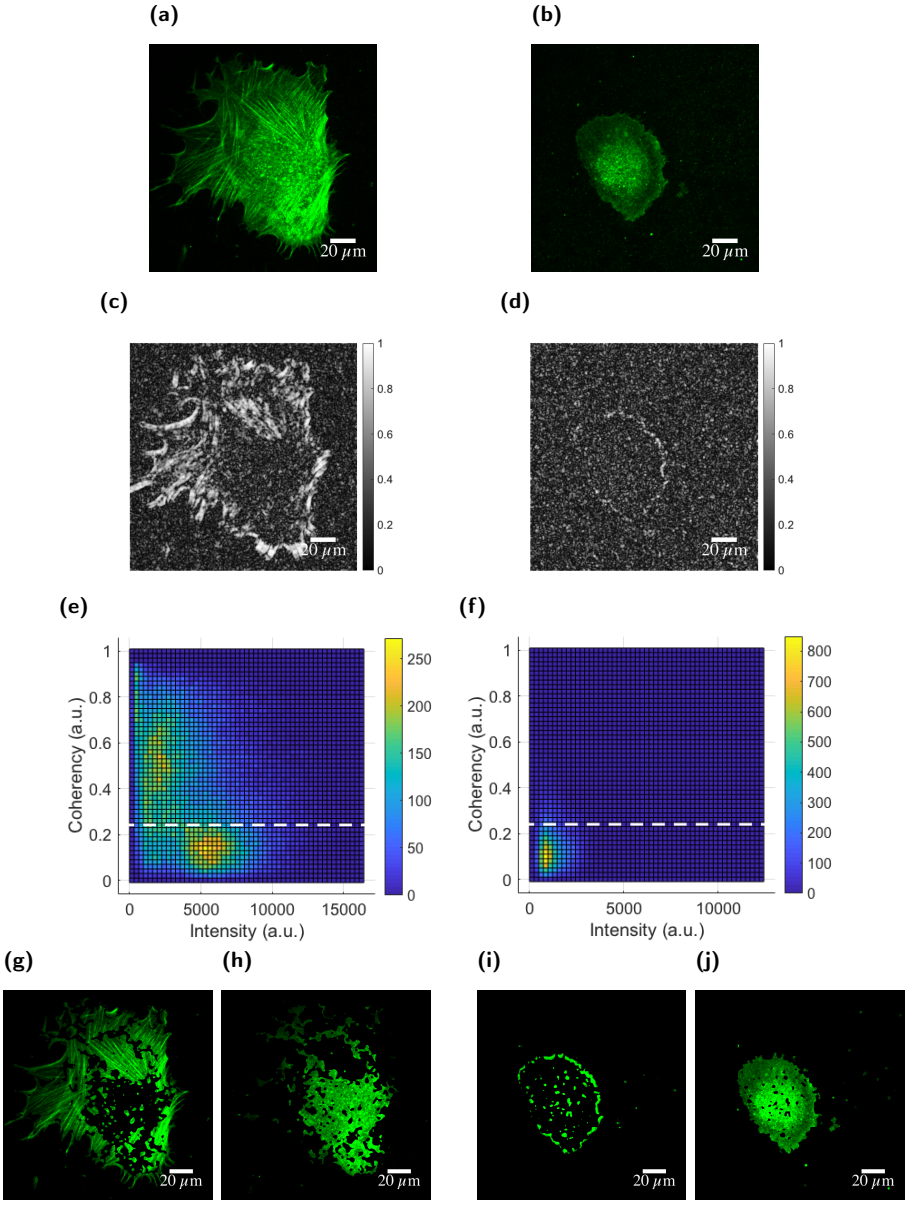


Figure 4.2: Representative images for coherency evaluation. (a, b) HASM cells with α-SMA (shown in green) recruited and not recruited to stress fibers. (c, d) Coherency maps built by the FIJI plug-in for the (a) and (b) respectively. (e, f) 3D histograms of the coherency values distribution vs corresponding intensity per pixel for the (a) and (b) respectively. (g, i) "coherent" (higher then 0,25 a.u. – dashed line on (e) and (f)) and (h, j) "non-coherent" (lower then 0,25 a.u.) areas of the α-SMA staining within the cell.

with an algorithm based on the earlier described triangle method [12]. This algorithm comprised an opportunity to manually tune the image intensity histogram offset to ensure a correct mask correlation with the cell. After the subsequent background subtraction and edges detection an image dilation and hole filling algorithms were implemented. The obtained cell mask was used to delete the cell coherency values and leave the background.

Quantified average level of maximal background values (0.25 a.u.) was further used to separate "coherent" (with fibers) (Fig. 4.2g, 4.2i) and "non-coherent" (without fibers) (Fig. 4.2h, 4.2j) regions of the α-SMA staining within the cell. Finally, the box plot graphs displaying the distribution of medians of the coherency values per cell were built. These coherency values were taken from the "coherent" regions (higher then 0.25 a.u.) of the cell. Additionally, the distributions of the percentage of these regions from the total cell area were shown. This graphs allowed us to compare the degree of α-SMA recruitment to the cell stress fibers, while the box plots showing the variation in the median values of the total α-SMA immunostaining intensity per cell could be used to estimate the level of α-SMA general expression.

4.2.5 Statistical analysis

To assess significance of the difference between two conditions, the Wilco-xon rank sum test in the Matlab program was used. This test is an equivalent to a Mann-Whitney U test.

4.3 Results

4.3.1 α-SMA expression and recruitment to stress fibers quantified by orientation analysis.

First, we investigated whether the level of α-SMA expression and the cell extracellular matrix (ECM) may influence the degree of the α-SMA recruitment to cell stress fibers during the spreading. We used SV80 human fibroblasts as an α-SMA negative control and HASM human aorta smooth muscle cells as an α-SMA positive control. As a source for PCs we used hiPSC line LUMC06iCTRL-derived PCs (CD31–) [9, 13] of an early passage that expressed very little to no α-SMA and very little SMC

markers such as (SM)22 and Calponin (CNN1), distinguishing them from SMCs.

Cells were placed on gelatin or fibronectin (FN) covered coverslips for 4 hours, fixed and stained with anti-α-SMA antibody followed by staining with an Alexa-532-coupled secondary antibody. Collected confocal images of the α-SMA fluorescent staining were used to identify the presence and the level of orientation within local features of the α-SMA staining distribution that we quantified as coherency (see Methods section). Only those areas were taken into account and considered "coherent" that had values higher then the average coherency background ($\sim$0.25 a.u.). Additionally we quantified a percentage of the "coherent" cell area from the total cell area that was analyzed (A_{coh}/A_{tot} (%)) to get a better overview of the degree of α-SMA recruitment to stress fibers.

CD31– cells on coverslips coated with gelatin had a comparable level and percentage of coherency to fibroblasts (Fig. 4.3d) (Fig. 4.3f). This level was close to the overall image background pointing on the absence of oriented features and isotropic distribution of the anti-α-SMA antibody staining inside cells (Example figures. 4.3a, b). HASM cells, in turn, had more α-SMA staining organized in fibers (Fig. 4.3c) that was also reflected in a higher level of coherency as well as the percentage of the coherent area compared to SV80 or CD31– cells (Fig. 4.3d, 4.3f). On FN coated glass coverslips overall levels of coherency both of CD31– (median value =0.33 a.u.) and SV80 (median value =0.3 a.u.) were higher then on gelatin (median value CD31– =0.31 a.u., SV80 =0.295 a.u.)(significance of the difference for SV80 cells $p<0.0005$, for CD31– $p=0.0029$)(Fig. 4.3g). Similar effect was found for the percentage of the cell coherent area (Fig. 4.3g). Notably, the level of coherency quantified for CD31– cells seeded on FN was comparable with the coherency of HASM cells seeded on gelatin (median value =0.33 a.u.) (significance of the difference $p=0.44$). However, the percentage of the coherent area within the cell quantified for SV80 and CD31– cells was similar (Fig. 4.3g).

Together, we showed that our image analysis tool for quantification of the α-SMA expression and recruitment conforms with the known data about the α-SMA expression in the tested cell lines. Interestingly, on the FN covered substrate CD31– cells showed an increased α-SMA recruitment to the F-actin cytoskeleton. This suggests a heterogeneous α-SMA expression within the PCs that can be modulated by ECM attachment.

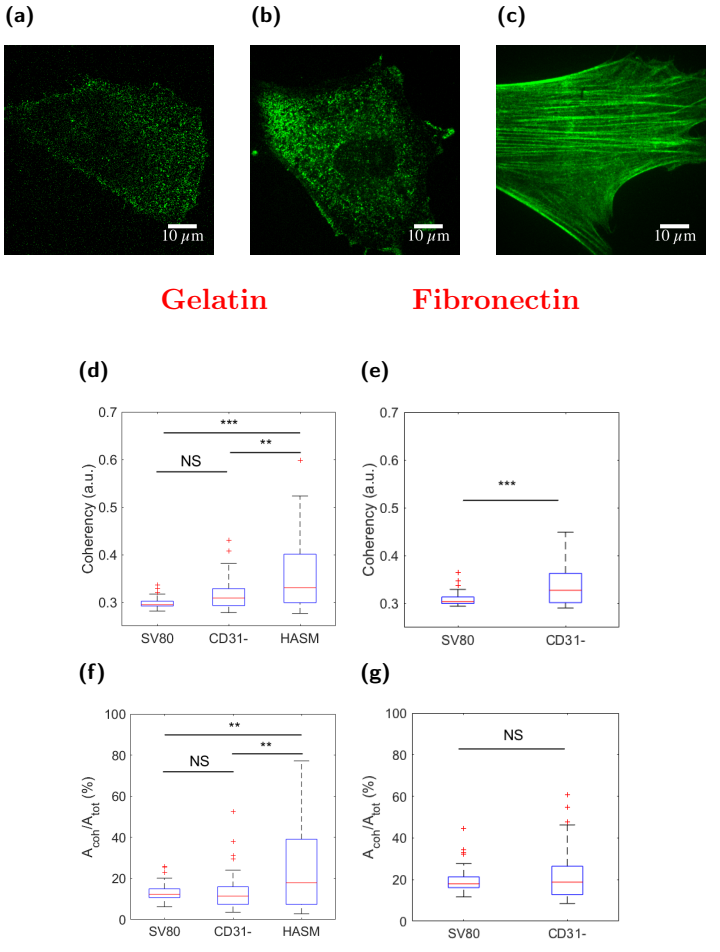


Figure 4.3: Representative images of the α-SMA immunostaining of the (a) SV80, (b) CD31– and (c) HASM cell lines seeded on gelatin coating. (d) Coherency comparison of three different human cell lines seeded on gelatin coating. (e) Coherency comparison of two different human cell lines seeded on FN coating (f, g) Respective medians of the percentage of the cell "coherent" area. Results are derived from three independent experiments performed in minimum two replicates. NS, P>0.05; *P<0.05; **P<0.005; ***P<0.0005 according to Mann - Whitney test.

4.3.2 Changes in α-SMA recruitment to stress fibers of PCs driven by growth factors.

We further investigated whether growth factors (GFs) that either induce or inhibit α-SMA expression in PCs may also influence the rate and the degree of it's recruitment to stress fibers. Additionally, we studied a potential effect from the cell ECM properties on the α-SMA recruitment in PCs treated with GFs. We used TGF-β and FGF2 in relation to two different ECM protein substrates on which the cells were placed. TGF-β is known to induce α-SMA expression [14], while FGF2 was shown to inhibit α-SMA expression in PCs [15, 16]. As substrates for CD31– cell adhesion we used FN and gelatin coatings. According to our previous findings (see Chapter 3) PC have a strong affinity towards FN, while gelatin is a recommended substrate for culturing PCs or SMCs.

The effect of GF treatment on α-SMA recruitment to stress fibers in CD31– cells was studied in two set-ups. In the first set-up CD31– cells were seeded on top of the coverslips covered with either gelatin or FN for 24 hours in either normal media, or a media containing two different amounts of TGF-β (1ng/ml and 10ng/ml), or a media with 5ng/ml concentration of FGF2 (Fig. 4.4a). After incubation cells were fixed and immunostained with the anti-α-SMA antibody, followed by imaging and coherency analysis of the image data (Fig. 4.4). In the second set-up CD31– cells were, first, incubated in a petridish with gelatin or FN coating for four days in a media containing either 1ng/ml concentration of TGF-β, or 10ng/ml – TGF-β, or 5ng/ml FGF2, as well as, in a normal media. After these four days cells from the gelatin coated petridishes were trypsinized and seeded for 4 hours in normal media on coverslips coated with gelatin, and cells from the FN coated petridishes – on coverslips coated with FN (Fig. 4.5a). Subsequently CD31– cells were fixed and the coherency of anti-α-SMA immunostaing distribution was quantified (Fig. 4.5). This approach allowed us to study: (i) the influence of the ECM on the PC response to treatment with GFs for a short term; (ii) the change in the speed of α-SMA recruitment to the stress fibers after prolonged exposure to GFs.

Local coherency quantification results obtained from the CD31– cells incubated with GFs for 24 hours didn't show a significant difference from the control sample on gelatin (Fig. 4.4b)(control=0.314 a.u., 1ng/ml TGF-β=0.316 a.u., 10ng/ml TGF-β=0.36 a.u., FGF2=0.33 a.u. with the significance of the difference $p>0.05$ for all samples) as well as on

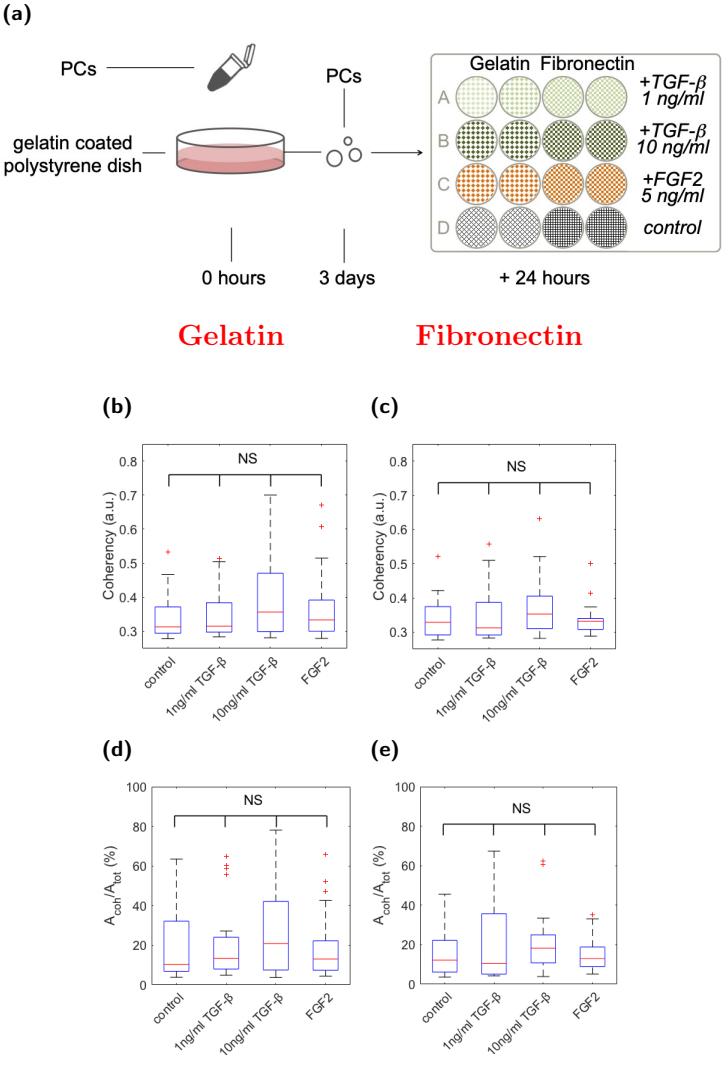


Figure 4.4: (a) Schematic representation of the experiment setup. (b, c) Coherency quantification results of CD31– cells incubated with GFs for 24 hours on gelatin (b) and FN (c). (d, e) Respective medians of the "coherent" area percentage within the total cell area of CD31– cells incubated on gelatin (d) or FN (e). Results are derived from two independent experiments performed in minimum three replicates. NS, P>0.05; *P<0.05; **P<0.005; ***P<0.0005 according to Mann - Whitney test.

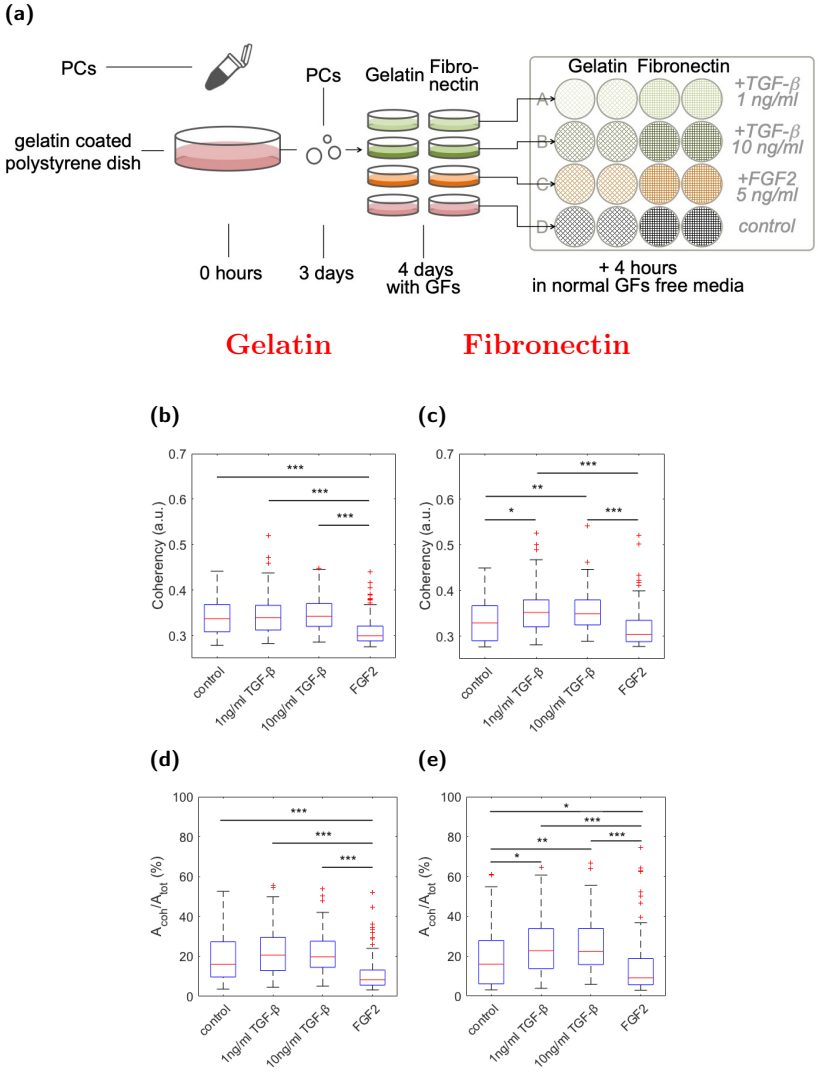


Figure 4.5: (a) Schematic representation of the experiment setup. (b, c) Coherency quantification results of CD31– cells treated with GFs for 4 days and fixed after 4 hours incubation in full media on gelatin (b) and FN (c). (d, e) Respective medians of the "coherent" area percentage within the total cell area of CD31– cells incubated on gelatin (d) or FN (e). Results are derived from two independent experiments performed in minimum three replicates. NS, P>0.05; *P<0.05; **P<0.005; ***P<0.0005 according to Mann - Whitney test.

FN substrates (Fig. 4.4c) (control=0.33 a.u., 1ng/ml TGF-β=0.312 a.u., 10ng/ml TGF-β=0.35 a.u., FGF2=0.33 a.u. with the significance of the difference p>0.05 for all samples). Also, coherency quantification results on gelatin were not significantly different from the results on FN in any GF condition. This data suggests a low or no influence from the short treatment with GFs on the recruitment of α-SMA to the F-actin cytoskeleton of CD31– cells both on gelatin or on FN.

Nevertheless, prolonged treatment with GFs affected the recruitment of α-SMA in CD31– cells (Fig. 4.5). Four days of incubation with TGF-β resulted in increased coherency levels of CD31– cells seeded on FN compared to the control sample and decreased – for CD31– cells treated with FGF2 (Fig. 4.5c) (control=0.33 a.u., 1ng/ml TGF-β=0.35 a.u., 10ng/ml TGF-β=0.35 a.u., FGF2=0.3 a.u.). This was also reflected in the quantification of the respective coherent area of CD31– cells seeded on FN (Fig. 4.5e). However, on gelatin only the treatment with FGF2 resulted in coherency levels different from the control sample (Fig. 4.5b) (control=0.337 a.u., 1ng/ml TGF-β=0.34 a.u., 10ng/ml TGF-β=0.34 a.u., FGF2=0.29 a.u. with the significance of the difference p>0.05 for TGF-β treated samples compared to the control). Treatment with TGF-β failed to increase the recruitment rate of α-SMA in CD31– cells incubated on gelatin (Fig. 4.5b). The same situation was observed from the percentage quantification of the coherent area from the total cell area of CD31– cells seeded on gelatin (Fig. 4.5c). Nevertheless, coherency quantification results obtained on gelatin were not significantly different from the results on FN in any GF condition. The coherency quantification results obtained for the samples treated for 24 hours or 4 days with 1 ng/ml TGF-β were not different form those treated with 10 ng/ml TGF-β both on FN or gelatin (Fig. 4.4, 4.5).

Taken together, we showed that prolonged treatment with GFs affects not only the expression of α-SMA in CD31– cells, but also the rate of it's recruitment to stress fibers of cells. Notably, CD31– cells treated with FGF2 for four days either on FN or gelatin both showed a decrease in the coherency values (Fig. 4.5c, b) to the level obtained earlier for human fibroblasts (Fig. 4.3), confirming an inhibitory action of the FGF2 on the α-SMA.

4.3.3 Inhibition of the time dependent increase in the α-SMA expression and recruitment to stress fibers in PCs on patterned FN substrates.

Here we investigated further the effect from the ECM properties on PCs expression and recruitment of the α-SMA. PCs bind and can apply forces on capillaries through BM proteins (Chapter 3). The interstitial layer of the BM in between PCs and ECs comprises LM and FN. FN is organized in small patches embedded into the LM layer and these patches may play a role of adhesion points for PCs (see Chapter 3) [10, 17, 18] (Fig. 1.1). We have seen that PCs are able to sense the variation in the stiffness of FN patches and respond by changing, sometimes dramatically, their traction forces, spreading area and the size of cell matrix adhesions. Thus, we studied whether the gradient of the α-SMA expression in PCs observed on the different parts of the microvasculature can be mediated by the diameter of the microvessel, the stiffness of it's BM and the presence of FN patches in the interstitial layer of the BM.

First, we examined whether FN organized in patches in the BM can influence the α-SMA expression and recruitment to stress fibers in CD31– cells. We compared CD31– cells seeded on the monolayer of FN vs CD31– cells seeded on our model of the PC-EC interstitial layer of the BM where FN was exposed to cells in a form of 2 μm diameter spots surrounded by LM (see Chapter 2, Fig. 2.2c). We tracked changes in the morphology of the early passage (passage 7) CD31– cells plated on a gelatin coated polystyrene dish over four days after thawing. As can be seen from the representative images obtained after 24 hours and 4 days of incubation (Fig. 4.6a), CD31– cells became larger and changed their rhomboid shape to a more typical for SMCs morphology with longer aligned cell bodies. These CD31– cells were further splitted and seeded either on a PDMS flat surface prepared in the ratio 1:10 crosslinker:base and stamped with FN monolayer or with an earlier described pattern of FN dots surrounded by LM (Fig. 2.2c). Subsequently, one sample of CD31– cells seeded on the FN monolayer was fixed after 24 hours and the second one – after 7 days. Cd31– cells seeded on the patterned PDMS substrate were fixed after 7 days of incubation (Fig. 4.6a – the scheme of the experiment). All samples were further simultaneously permeabilized and immunostained with anti-α-SMA antibody.

Local coherency quantification results (Fig. 4.6b) revealed CD31– cells that undertook the SMCs like morphology have got a higher level

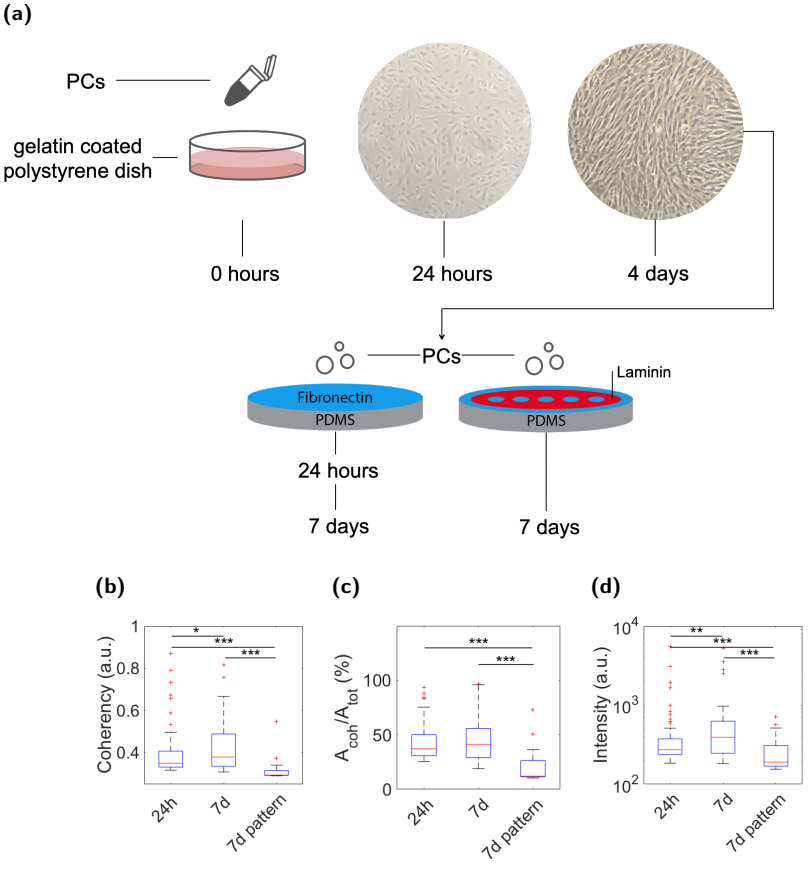


Figure 4.6: (a) Schematic representation of the experiment setup and the CD31– cell morphology after 24 hours of incubation on gelatin coated polystyrene dishes and 4 days. (b) Coherency quantification results for CD31– used after 4 days of incubation in a polystyrene dish and placed on either FN glass coverslips covered with FN monolayer for 24 hours and 7 days or on a PDMS flat surface for 7 days prepared in the ratio 1:10 crosslinker:base and stamped with an earlier described pattern of FN dots surrounded by LM (Fig. 2.2c). (c) Respective medians of the percentage of the cell "coherent" area. (d) Supportive median values of the α-SMA immunostaining intensities obtained from the total cell area that was analyzed per image for each condition. Results are derived from one experiment performed in two replicates. NS, P>0.05; *P<0.05; **P<0.005; ***P<0.0005 according to Mann - Whitney test.

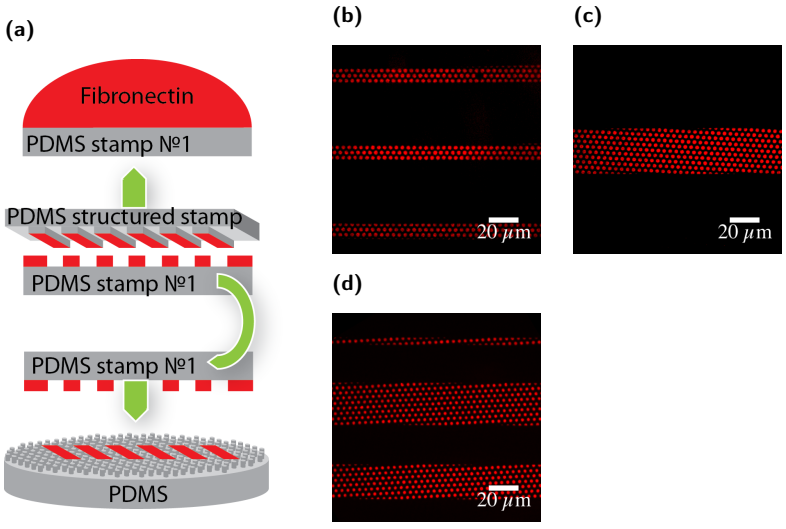


Figure 4.7: FN line pattern generation on top of the PDMS micropillar arrays. (a) A FN line microcontact printing scheme. (b – d) representative images of the different width FN (red) line stamping results on top of the micropillar arrays

of coherency (median value =0.35 a.u.) after 24 hours of incubation on FN, compared to the aforementioned result obtained from CD31– cells that were used before the change in their morphology (median value =0.33 a.u.) (significance of the difference p=0.003) (Fig. 4.4c). The coherency level appeared even higher in CD31– cells fixed after 7 days of incubation on a FN monolayer (Fig. 4.6b). Notably, CD31– cells plated on the PDMS surface patterned with FN dots embedded into LM after 7 days of incubation showed much lower level of coherency (median value =0.294) then the same cells plated on a FN monolayer (Fig. 4.6b). This value was comparable to the earlier obtained result for the α-SMA negative fibroblast cell line – SV80 (Fig. 4.3d, e). A similar effect was observed in the percentage evaluation of the coherent area within the cells (Fig. 4.6c). CD31– cells seeded on a pattern of FN dots surrounded by LM showed a lower percentage of the coherent area then CD31– cells on FN monolayer after 7 days of incubation, telling that lower amount of α-SMA fibers was formed. This data suggests an inhibitory effect from the FN organized in patches in the capillary BM on the α-SMA recruitment to the F-actin cytoskeleton of PCs.

Further, we studied a possible influence of the capillary stiffness or diameter on the α-SMA expression levels in PCs on different parts of the microvascular tree. PDMS micropillar arrays of three different stiffness (11.6 kPa, 47.2 kPa and 137 kPa) were developed and stamped with tree different patterns of FN: homogeneous layer, 30 μm wide FN lines and 10 μm wide FN lines (Fig. 4.7). This allowed us to introduce such parameters like varying substrate stiffness and restricted area for the cell adhesion into our system, representing the capillary rigidity and diameter variation. The pillars had the same diameter and arrangement as FN spots surrounded by LM on the PDMS flat surface in the previous experiment. CD31– cells were seeded onto PDMS micropillar arrays and fixed after either 4 hours of incubation or 7 days. As a control cell line for the immunostaining results we used HASM cells that were allowed to spread on PDMS micropillar arrays for 7 days. All samples were permeabilized and immunostained with anti-α-SMA antibody simultaneously. The coherency analysis revealed a low level of orientation within the CD31– cells local anti-α-SMA staining distribution on all stiffness. This effect was observed in all samples fixed after 4 hours as well as after 7 days of incubation (Fig. 4.8, 4.9, 4.10). A slight drop in the coherency level of CD31– cells was observed after 7 days of incubation on 137 kPa micropillar arrays with homogeneous stamping (from median value 0.31 to 0.306 with the significance of the difference p=0.0042) (Fig. 4.8a vs 4.8b), on 11.6 kPa arrays with 30 μm wide line stamping (from median value 0.306 to 0.303 with the significance of the difference p=0.012) (Fig. 4.9a vs 4.9b) and on 11.6 kPa and 47.2 kPa stiff arrays with 10 μm wide FN line stamping (from median value 0.31 to 0.308 with the significance of the difference p=0.010 and from – 0.304 to 0.29 with the significance of the difference p=0.022 respectively) (Fig. 4.10a vs 4.10b), compared to the results obtained after 4 hours of incubation. Notably, coherency levels were always the highest for CD31– cells incubated for 4 hours on 137 kPa micropillar arrays (Fig. 4.8a, 4.9a, 4.10a), but the difference became less prominent after 7 days of incubation (Fig. 4.8b, 4.9b, 4.10b). Nevertheless, HASM cells in total showed higher levels of coherency, obtained after 7 days of incubation, than CD31– cells after 4 hours or 7 days. The same was observed from the quantification of the coherent area persentage within cells. On avarage after 7 days of incubation CD31– cells had a lower amount of α-SMA fibers than HASM cells (Fig. 4.8e vs 4.8f, 4.9e vs 4.9f, 4.10e vs 4.10f). Interestingly, on 47.2 kPa

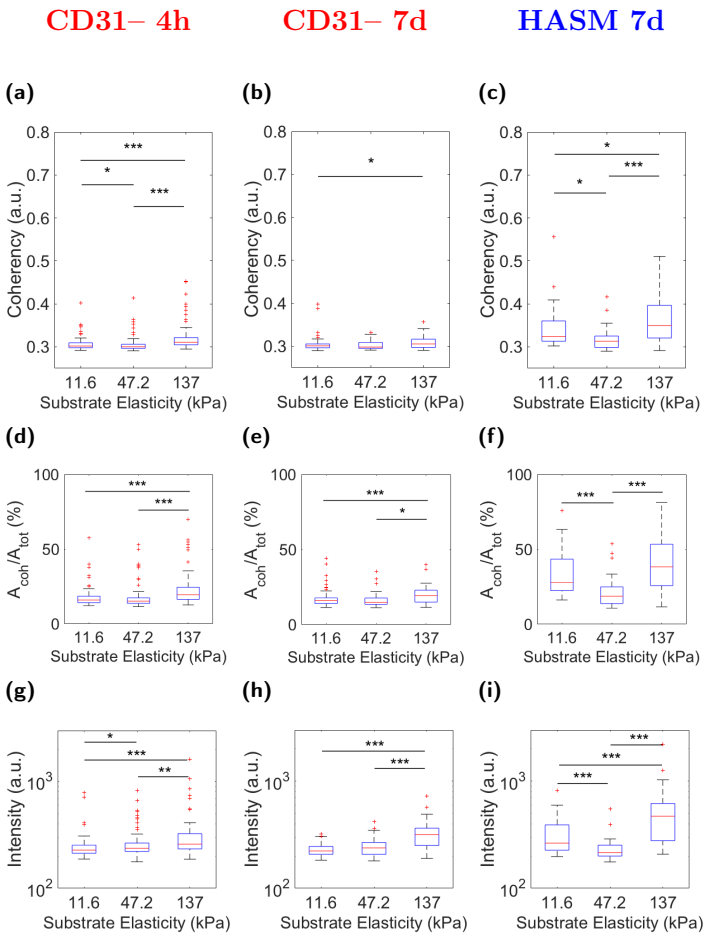


Figure 4.8: (a – b) Coherency quantification results of CD31– seeded for 4 hours (a) and for 7 days (b) on PDMS micropillar arrays of three different rigidities with homogeneous FN stamping, compared to the results of the α-SMA positive control cell line – HASM (c) after 7 days of incubation. (d – f) Respective medians of the "coherent" area percentage within the total cell area of CD31– (d, e) and HASM cells (f). (g – h) Supportive median values of the α-SMA immunostaining intensities obtained from the total cell area that was analyzed per image for each condition. Results are derived from one experiment performed in two replicates. NS, P>0.05; *P<0.05; **P<0.005; ***P<0.0005 according to Mann - Whitney test.

stiff pillars the local orientation values of the anti-α-SMA staining distribution in HASM cells were lower than on 11.6 kPa or 137 kPa arrays, indicating an overall lower α-SMA recruitment degree to the stress fibers

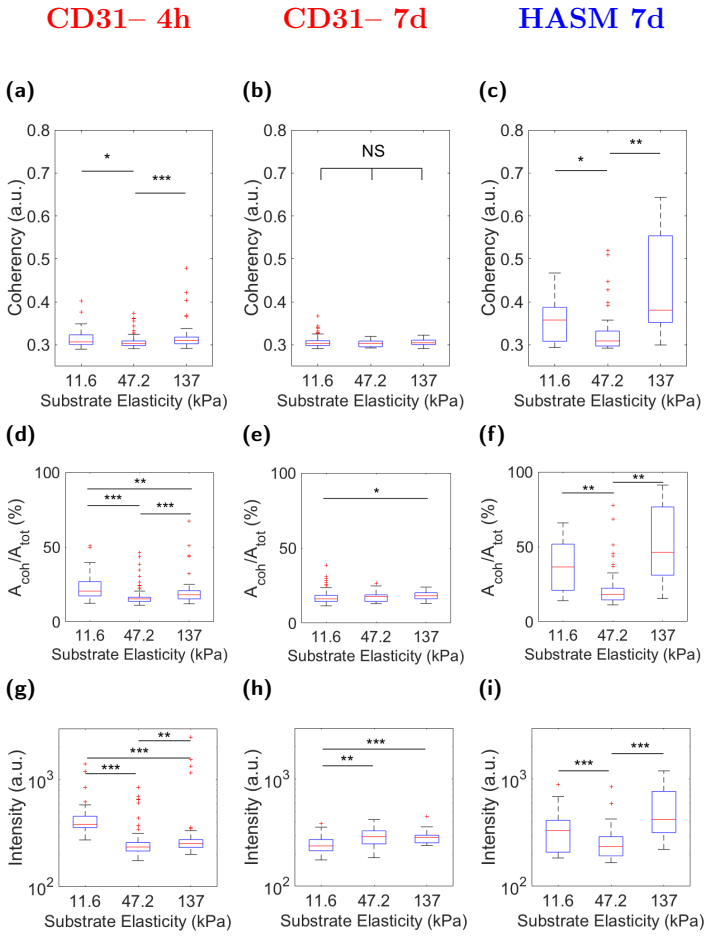


Figure 4.9: (a – b) Coherency quantification results of CD31– seeded for 4 hours (a) and for 7 days (b) on PDMS micropillar arrays of three different rigidities with 30 μm line FN stamping, compared to the results of the α-SMA positive control cell line – HASM (c) after 7 days of incubation. (d – f) Respective medians of the "coherent" area percentage within the total cell area of CD31– (d, e) and HASM cells (f). (g – h) Supportive median values of the α-SMA immunostaining intensities obtained from the total cell areas that were analyzed per image for each condition. Results are derived from one experiment performed in two replicates. NS, P>0.05; *P<0.05; **P<0.005; ***P<0.0005 according to Mann - Whitney test.

on this intermediate stiffness (47.5 kPa) than on soft (11.6 kPa) or stiff (137 kPa) substrates (Fig. 4.8c, 4.9c, 4.10c).

This data shows that the presence of FN deposits in the BM of ca-

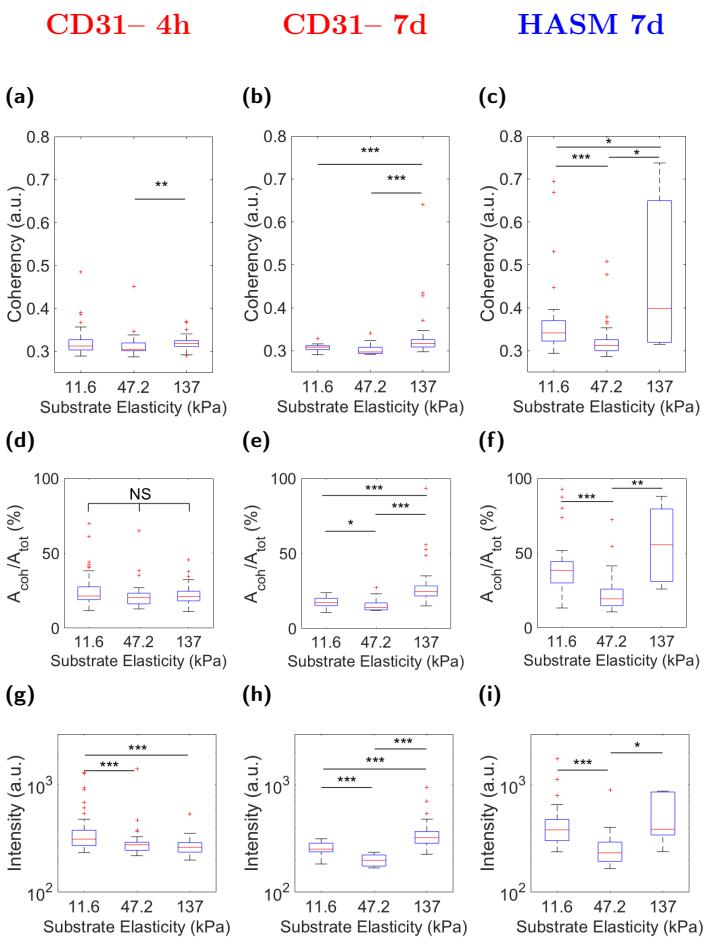


Figure 4.10: (a – b) Coherency quantification results of CD31– seeded for 4 hours (a) and for 7 days (b) on PDMS micropillar arrays of three different rigidities with 10 μm line FN stamping, compared to the results of the α-SMA positive control cell line – HASM (c) after 7 days of incubation. (d – f) Respective medians of the "coherent" area percentage within the total cell area of CD31– (d, e) and HASM cells (f). (g – h) Supportive median values of the α-SMA immunostaining intensities obtained from the total cell areas that were analyzed per image for each condition. Results are derived from one experiment performed in two replicates. NS, P>0.05; *P<0.05; **P<0.005; ***P<0.0005 according to Mann - Whitney test.

pillaries has an α-SMA inhibitory effect on PCs and less on SMCs cells. Taken together our results suggest an adaptable expression/cytoskeletal recruitment of α-SMA in PCs, which can be modulated by the ECM

properties. In the presence of FN deposits restricted to the 2 μm spot size, CD31– cells maintain a low level of localized α-SMA expression in stress fibers of and the influence from the capillary stiffness or diameter appears to be minor. By contrast, HASM cells induced α-SMA localization in stress fibers on stiff substrates irrespective of patterning.

4.4 Discussion

PCs show different levels of α-SMA expression depending on their location along the vascular tree [4–6]. *In vivo* and *in vitro* studies on PCs and other cell types show that α-SMA expression is largely affected by soluble factors, but also can be attenuated by mechanical stimuli like substrate stiffness and ECM. Taking into the account that the change of the capillary order is accompanied by the change in it's diameter, inside blood pressure, BM thickness and protein composition, PCs experience different mechanical signals on different parts of the microvascular tree and this may have an influence on the α-SMA expression. Earlier findings already pointed on a special role of ECM mechanical properties in the α-SMA regulation in myofibroblasts [19] as well as in mesenchymal stem cells [20]. Whether and how do these factors combine to condition α-SMA expression gradient in PCs in the resting vasculature remains unclear.

The main soluble factor inducing α-SMA expression in PCs is TGF-β. It has been shown to be essential for mural cell maturation into vascular SMCs [17]. PCs and ECs both express TGF-β and have TGF-β receptors on them. However, its activation from a latent proform happens when the two cell types come into contact with each other [1, 21]. How the effect from TGF-β activation is further balanced out in PCs to result in gradual increase of the α-SMA on different parts of the vascular tree is not well defined. Here we tested whether deviating levels of the α-SMA in PCs could be a consequence of TGF-β gradient in vasculature. Obtained data showed that treatment with various concentrations of TGF-β did not result in a deviating expression or recruitment rate of the α-SMA to stress fibers in PCs. Same result was obtained when two different treatment times were compared suggesting that growth factor control may not be sufficient for fine-tuning the α-SMA expression levels. Nevertheless, we noticed that the effect from the TGF-β treatment was dependent on the ECM protein coating of the substrate on which PCs

were placed. Treatment was more effective on FN, resulting in a higher levels of α-SMA recruitment rate to stress fibers. Similar observation was made by Chen and Hinz for mesenchymal stem cells [22]. They admitted that FN substrate coating in general favored α-SMA fibrogenesis in comparison to gelatin or pronectin. Kim and Gumbiner in turn reported that cell adhesion to FN promotes YAP nuclear accumulation through negative regulation of Hippo signaling pathway [23]. This can partially explain our results, taking into the account a direct relation between YAP/TAZ nuclear translocation and α-SMA expression reported earlier for mesenchymal stem cells and fibroblasts [20, 24].

FN is present in small amounts in the capillary BM, distributed in micron-sized deposits around the LM rich PC-EC interstitia. When PCs and ECs come into contact, PCs noticeably downregulate their FN expression levels, while ECs upregulate [25]. In 3D cell culture it has been shown that activated TGF-β from the PC-EC contact induces ECM production by ECs, yet, not the FN expression [26]. Limiting the amount of FN in the BM can be a key to the control over the α-SMA expression in PCs. Here we showed that α-SMA was upregulated over time in PCs originally α-SMA negative, placed on a stiff substrate of the culture dish with a FN monolayer. However, α-SMA levels were maintained or even downregulated by placing PCs on a pattern of 2 μm FN dots embedded into the LM monolayer. In the previous chapter we also showed a strong preference of PCs towards FN over LM. PCs mainly formed their cell-matrix contacts on FN dots and not on LM, when cultured on a patterned substrate. This behavior resulted in a limited size of their focal adhesions in comparison to a protein monolayer. Similar dependence between limited focal adhesion size and a low α-SMA recruitment to stress fibers was reported earlier for myofibroblasts. Authors could inhibit α-SMA recruitment by restricting cell focal adhesions to a size of printed ECM dots [19]. Taken together, there is an evidence that α-SMA recruitment to stress fibers in PCs can be affected by the amount of available FN and by its spatial arrangement.

Notably, in the presence of FN dot pattern, created by the functionalization of PDMS micropillars, CD31– failed to develop α-SMA fibers and didn't show a prominent dependence on the variation in substrate stiffness or available area for spreading. In contrast, HASMs maintained the ability to form α-SMA fibers on micropillar arrays and responded to the deviating stiffness and available area for spreading with different α-SMA

recruitment rates, yet higher then in PCs. This data demonstrates that after full maturation of PCs into SMCs they loose the ability to adjust α-SMA expression levels in response to the FN arrangement in the BM and become more dependent instead on vessel stiffness and diameter.

In this study we showed that our data analysis approach gives a benefit of gaining an uncompromised quantification information not only on the general α-SMA expression levels in cells, but also on the α-SMA recruitment degree to stress fibers, rate and total ratio with a single cell resolution. Such approach also can come into help when limited amount of cells is available, or when two conditions are being compared on the same sample, or when a dynamic live cell data needs to be assessed. Our findings may help to unveil processes behind maintaining α-SMA expression gradient in PCs and can be used to keep PCs from obtaining contractile phenotype in cell culture.

Bibliography

[1] Annika Armulik, Guillem Genové and Christer Betsholtz. « Pericytes: developmental, physiological, and pathological perspectives, problems, and promises. » In: *Dev. Cell* 21.2 (2011), pp. 193–215. ISSN: 1534-5807.

[2] Bruce M Koeppen. *Berne & Levy Physiology*. 6th ed., updated ed. Philadelphia, PA: Mosby/Elsevier, 2009. ISBN: 9780323278669.

[3] K.W. Zimmermann. « Der feinere bau der blutcapillares ». In: *Z. Anat. Entwickl.* 68 (1923), pp. 3–109.

[4] V Nehls and D Drenckhahn. « Heterogeneity of microvascular pericytes for smooth muscle type alpha-actin. » In: *JCB* 113.1 (1991), pp. 147–154. ISSN: 0021-9525.

[5] Roger Grant et al. « Organizational hierarchy and structural diversity of microvascular pericytes in adult mouse cortex ». In: *J Cereb Blood Flow Metabolism* 39.3 (2017), pp. 411–425. ISSN: 0271-678X.

[6] Robert A Hill et al. « Regional Blood Flow in the Normal and Ischemic Brain Is Controlled by Arteriolar Smooth Muscle Cell Contractility and Not by Capillary Pericytes. » In: *Neuron* 87.1 (2015), pp. 95–110. ISSN: 0896-6273.

[7] Akhilesh Kumar et al. « Specification and Diversification of Pericytes and Smooth Muscle Cells from Mesenchymoangioblasts ». In: *Cell Reports* 19.9 (2017), pp. 1902–1916. ISSN: 2211-1247.

[8] Valeria V Orlova et al. « Functionality of Endothelial Cells and Pericytes From Human Pluripotent Stem Cells Demonstrated in Cultured Vascular Plexus and Zebrafish Xenografts ». In: *Arteriosclerosis Thrombosis Vasc Biology* 34.1 (2014), pp. 177–186. ISSN: 1079-5642.

[9] Valeria V Orlova et al. « Generation, expansion and functional analysis of endothelial cells and pericytes derived from human pluripotent stem cells. » In: *Nat Protoc* 9.6 (2014), pp. 1514–31. ISSN: 1750-2799.

[10] PJ Courtoy and J Boyles. « Fibronectin in the microvasculature: localization in the pericyte-endothelial interstitium. » In: *J. Ultrastruct. Res.* 83.3 (1983), pp. 258–73. ISSN: 0022-5320.

[11] Z. Püspöki et al. « Transforms and Operators for Directional Bioimage Analysis: A Survey ». In: *Focus on Bio-Image Informatics*. Ed. by W.H. De Vos, S. Munck and J.-P. Timmermans. Vol. 219. Advances in Anatomy, Embryology and Cell Biology. Springer International Publishing, May 2016. Chap. 3, pp. 69–93.

[12] GW Zack, WE Rogers and SA Latt. « Automatic measurement of sister chromatid exchange frequency. » In: *J. Histochem. Cytochem.* 25.7 (1977), pp. 741–53. ISSN: 0022-1554.

[13] C. Dambrot et al. « Polycistronic lentivirus induced pluripotent stem cells from skin biopsies after long term storage, blood outgrowth endothelial cells and cells from milk teeth ». In: *Differentiation* 85.3 (2013), pp. 101–109. ISSN: 0301-4681.

[14] MM Verbeek et al. « Induction of alpha-smooth muscle actin expression in cultured human brain pericytes by transforming growth factor-beta 1. » In: *Am. J. Pathol.* 144.2 (1994), pp. 372–82. ISSN: 0002-9440.

[15] Michael Papetti et al. « FGF-2 antagonizes the TGF-beta1-mediated induction of pericyte alpha-smooth muscle actin expression: a role for myf-5 and Smad-mediated signaling pathways. » In: *Invest. Ophthalmol. Vis. Sci.* 44.11 (2003), pp. 4994–5005. ISSN: 0146-0404.

[16] Gregory J Sieczkiewicz and Ira M Herman. « TGF-β signaling controls retinal pericyte contractile protein expression ». In: *Microvascular research* 66.3 (2003), pp. 190–196. ISSN: 0026-2862.

[17] Annika Armulik, Alexandra Abramsson and Christer Betsholtz. « Endothelial-pericyte interactions. » In: *Circ. Res.* 97.6 (2005), pp. 512–23. ISSN: 0009-7330.

[18] Ethan A Winkler, Robert D Bell and Berislav V Zlokovic. « Central nervous system pericytes in health and disease ». In: *Nature Neuroscience* 14.11 (2011), pp. 1398–1405. ISSN: 1097-6256.

[19] Jérôme M Goffin et al. « Focal adhesion size controls tension-depen-dent recruitment of α-smooth muscle actin to stress fibers ». In: *JCB* 172.2 (2006). ISSN: 0021-9525.

[20] Nilesh P Talele et al. « Expression of α-Smooth Muscle Actin Determines the Fate of Mesenchymal Stromal Cells ». In: 4.6 (2015), pp. 1016–1030. ISSN: 2213-6711.

[21] Y Sato. « Inhibition of endothelial cell movement by pericytes and smooth muscle cells: activation of a latent transforming growth factor-beta 1-like molecule by plasmin during co-culture ». In: 109.1 (1989), pp. 309–315. ISSN: 0021-9525.

[22] Chen Li et al. « MicroRNA-21 preserves the fibrotic mechanical memory of mesenchymal stem cells ». In: 16.3 (2016), pp. 379–389. ISSN: 1476-1122.

[23] Nam-Gyun Kim and Barry M Gumbiner. « Adhesion to fibronectin regulates Hippo signaling via the FAK-Src-PI3K pathway ». In: *JCB* 210.3 (2015), pp. 503–515. ISSN: 0021-9525.

[24] Fei Liu et al. « Mechanosignaling through YAP and TAZ drives fibroblast activation and fibrosis ». In: *Am J Physiol-lung C* 308.4 (2015), pp. L344–L357. ISSN: 1040-0605.

[25] Amber N Stratman et al. « Pericyte recruitment during vasculogenic tube assembly stimulates endothelial basement membrane matrix formation. » In: *Blood* 114.24 (2009), pp. 5091–101. ISSN: 0006-4971.

[26] JA Madri. « Phenotypic modulation of endothelial cells by transforming growth factor-beta depends upon the composition and organization of the extracellular matrix ». In: 106.4 (1988), pp. 1375–1384. ISSN: 0021-9525.

BIBLIOGRAPHY

Chapter 5

Pericyte force generation in *in vitro* Hypoxia and Ischemia conditions [1]

abstract

Pericytes (PCs) are contractile cells that align blood microvessels. Their contractility plays an important role in physiology and pathology. For example in Ischemia, PCs have been shown to die shortly after they constrict capillaries in response to compromised oxygen and glucose supply. Consequently, capillaries are blocked by dead, constricted PCs further reinforcing the diseased condition leading to large-area brain damage after a stroke.

The essential cells involved in Ischemia are mid-capillary PCs that are difficult to study specifically as of the absence of unique markers, hence studies are limited to *in vivo*, post-event investigations. In particular the constriction model is difficult to asses since it is not possible to measure directly the forces PCs apply at a high level of control over the experimental conditions *in vivo*.

Here we developed and described a novel approach that allows to accurately monitor cellular forces and morphology, while rapidly changing microenvironmental conditions. By integrating PDMS micropillar arrays inside of fluid-flow channels and using human induced pluripotent stem cell (hiPSC)-derived PCs, we brought *in vitro* experiments closer

1. This chapter is based on: O. Iendaltseva, V.V. Orlova, C.L. Mummery, E. H. J. Danen and T. Schmidt, Pericyte Force Generation in *In Vitro* Hypoxia and Ischemia Conditions, *In preparation*

to *in vivo* studies on Ischemia. The developed methodology does create an opportunity to track PC mechanoresponse to changes in oxygen and glucose supply in a real-time setting for future applications.

5.1 Introduction

Pericytes (PC) are mural cells of blood microvessels. They are isolated contractile cells involved in regulation of vascular morphogenesis and function in health and disease [1]. Among others, PCs are involved in Hypoxia induced angiogenesis in physiology (e.g. embryo development), and in pathology (e.g. tumour or tissue injury) [2]. Additionally, despite some contradictory results, they have been reported to participate in regulation of cerebral blood flow and promote brain damage in Ischemia in mice *in vivo* [3–5]. PCs have been shown to die shortly after they constrict capillaries in response to Ischemia, thus preventing renewal of the blood flow through capillary bed and damage of the neurons after stroke. Nevertheless, there is no direct evidence in terms of direct mechanical measurements of whether PCs are able to block capillary blood flow in Ischemia or not.

Therefore we first assessed the contractility of PCs in *in vitro* Hypoxia and Ischemia conditions, and compared those to the normal conditions.

Metazoan organisms use oxygen (O_2) for adenosine triphosphate (ATP) production. It is necessary to maintain O_2 homeostasis for proper organism development, physiology and function. A decrease in O_2 supply results in a condition called Hypoxia [6]. A subsequent response to Hypoxia in cells and tissues is regulated by the family of Hypoxia-inducible factor (HIF) transcription factors. HIFs are heterodimeric proteins composed of two subunits: one α (HIF-1α, HIF-2α, HIF-3α) and one β (HIF-β/ARNT). HIF-1α and HIF-2α play a central role in cellular response to Hypoxia [7]. O_2 deprivation stabilizes transcription factor HIF-1α and HIF-2α, which in turn regulate the expression of hundreds of genes to maintain O_2 homeostasis. This includes: glucose metabolism, cell proliferation, migration, cytoskeletal structure, metastasis, apoptosis, angiogenesis, extracellular matrix formation and remodeling, etc. Under normoxia conditions HIF-α is continuously produced and degraded by binding of the von Hippel-Lindau tumor suppressor protein (VHL) that interacts with the protein Elongin C, recruiting an E3 ubiquitin-protein ligase complex leading to HIF-α ubiquitination and degradation by the 26S proteasome. While in Hypoxia conditions, HIF-α degradation is inhibited due to the lack of oxygen. The protein accumulates, binds to HIF-β, translocates to the nucleus and activates Hypoxia-response gene transcription [2, 8].

Compromised blood supply in tissue leads to a decreased oxygen

and nutrients delivery, and results in a condition called Ischemia. In Ischemia, cells switch from aerobic to anaerobic metabolism that leads to a reduction of cell pH, high inflow of sodium ions into cells, depletion of cellular ATP and inactivation of ATPases, inhibition of Ca^{2+} outflow and intracellular calcium overload, opening of the mitochondrial permeability transition (MPT) pore and further impairment of ATP production. The degree of tissue injury depends on the organ, the level and duration of blood supply reduction [9].

To avoid heterogenity in PC cell culture, present in *in vivo* studies, we used human induced pluripotent stem cell (hiPSC)-derived PCs, that have been previously described and characterized in detail [10, 11]. The cells lack α-SMA expression and resemble "true" PCs, which have been found on mid-capillaries.

For simulation of Hypoxia and Ischemia conditions we used a chemical mimetic. Cells were treated with an indirect HIF-inhibitor DMOG that switches cells into a Hypoxia state, and we used glucose deprivation to switch cells to their starvation and Ischemia state. Indeed we were able to define a mechanical response that was specific to the different treatments.

However, our results showed that this static approach does not allow to accurately measure the fast response of PCs that occurs during the acute medical condition. To better simulate rapid changes in oxygen and glucose levels during Hypoxia and Ischemia, and to get our experiments closer to the aforementioned *in vivo* studies, we further developed and characterized a new experimental design. In this new design PDMS micropillar arrays are mounted inside commercially available fluid-flow channels. Cells are seeded on top of the micropillar arrays. Our novel approach allows to constantly track cellular forces and morphology while dynamically changing the environmental conditions such as: the temperature, the composition of the cell culture medium, and the oxygen concentration.

The novel approach presented in this chapter, is a ubiquitous design that permits the study of PCs behaviour during hypoxia and ischemia. It also can be applied to any other cells for which the environmental conditions needs to be changed, and where response in cell force application and morphology are questioned.

5.2 Methods

5.2.1 Cell culture

hiPSC line LUMC06iCTRL-derived CD31– (dif31), cell line was cultured in Dulbecco's Modified Eagle's Medium (DMEM, Gibco|Thermo Fisher Scientific, USA) supplemented with 10% fetal bovine serum (HyClone, Etten-Leur, The Netherlands), 25 U/ml penicillin and 25 µg/ml streptomycin (Invitrogen/Fisher Scientific). CD31– cell line was used on the passage 7 or 8 and was kept in culture for 3 to 4 days before the experiment to avoid changes in the cell morphology. Cells were seeded at 20 000 cells per dish. Cells were injected directly on top of the PDMS microropillar area of interest to ensure persistent cell density across experiments. After incubation they were fixed for 10' in 4% paraformaldehyde in PBS for further immunostaining.

Simulated Hypoxia

Hypoxia was simulated by chemical stabilization of HIF-α. CD31– cells were, first, incubated for 40 hours with dimethyloxalylglycine (DMOG, Sigma-Aldrich, d3695) added to the full culture media at 1 mM concentration. Then, they were detached from the culture dish using PBS and Trypsin with 1 mM DMOG. Finally, CD31– cells were seeded on top of the PDMS micropillar arrays in culture media containing 1 mM DMOG and 4.5 g/l D-glucose concentrations and fixed after 8.5 hours of spreading.

Simulated Ischemia

Ischemia was simulated by simultaneous chemical stabilization of HIF-α together with glucose deprivation from the culture media. CD31– cells were, first, incubated for 40 hours with dimethyloxalylglycine (DMOG, Sigma-Aldrich, d3695) added to the full culture media (DMEM, Gibco| Thermo Fisher Scientific, USA) at 1 mM concentration. Then, they were detached from the culture dish using PBS and Trypsin with 1 mM DMOG. Finally, CD31– cells were seeded on top of the PDMS micropillar arrays in the full cell culture media containing 1 mM DMOG for 7 hours. After 7 hours the media was exchanged with a low 1 g/l D-glucose cell culture medium (DMEM, Gibco | Thermo Fisher Scientific,

USA) containing 1 mM DMOG concentration and fixed after 1.5 hours of spreading in Ischemia conditions.

Starvation

Cell starvation was simulated by using low glucose culture media. CD31– cells were, first, incubated for 40 hours in full high glucose (4,5 g/l) media. Then, they were detached from the culture dish and placed on top of the PDMS micropillars arrays in a culture media containing low 1 g/l D-glucose. After 8.5 hours of incubation cells were fixed.

5.2.2 PDMS micropillar array preparation

PDMS micropillar arrays were prepared as was described before [12, 13]. Briefly, SI mold was made by two-step Deep Reactive Ion Etching (DRIE) process. This yielded a 10×10 mm hexagonal array of 2 μm diameter holes with 2 μm spacing and varying depth, flanked by two 50 μm deep 10×2 mm tranches. After mold passivation with trichloro silane (Sigma), PDMS 1:10 was poured over it and cured for 20 hours at 110°C. The peeled off PDMS had a negative of the mold shape with micropillar array and 50 μm high spacers on the sides of it. This array was functionalized with the help of PDMS 1:30 stamp and dried protein of interest on top of it. A 40 μl drop of FN or LM-111 mixture in water was incubated for 60' on the PDMS 1:30 stamp, then washed and dried under laminar flow. This stamp was then genly loaded onto UV-ozone activated PDMS micropillar array for 10'. Finally, stamped array was blocked with 0.2% Pluronic (F-127, Sigma) in PBS for 60' at room temperature and washed with PBS.

5.2.3 Immunostaining

Fixed cells were permeabilized for 10' with 0.1% Triton-X in PBS and blocked for 60' with 1% bovine serum albumin (BSA) (Sigma, a2153) in PBS. F-actin cytoskeleton of cells was stained for 1 hour with Alexa 532 phalloidin (Thermo Fisher Scientific, a22282) of a 1:1000 concentration in PBS. Cell nuclei were stained for 1 hour using 300 nM solution of 4',6-diamidino-2-phenylindole (DAPI, Sigma-Aldrich, d8417) in PBS. Each immunostaining step was followed by 3 washing steps in PBS 10' each under a gentle rocking.

5.2.4 Microscopy

Confocal imaging was performed on a home-built setup based on an Axiovert200 microscope body (Zeiss), spinning disk unit (CSU-X1, Yokogawa) and an emCCD camera (iXon 897, Andor). IQ-software enabled setup-control and data acquisition. Lasers of 405 nm (CrystaLaser), 488 nm (Coherent), 514 nm, 561 nm (Cobolt) and 642 nm (Spectra Physics) wavelength were coupled into the CSU via polarization maintaining single-mode fiber. Spacers on the sides of micropillar arrays allowed placing them upside down onto #0 coverslips (Menzel Glaser) with adhered cells facing down. This approach ensured reproducible cell observation within the limited working distance of a high-NA objective on an inverted microscope. For PDMS or glass 2D assays parafilm spacers were made directly on top of the glass coverslips.

5.2.5 Image analysis

Cell spreading area and nucleus size were quantified by using FIJI software. First the background was subtracted by adjusting the threshold level, followed by the cell/nucleus edge selection with a tracing tool. Finally mean values for at least 30 cells per condition were calculated.

Cell traction forces were measured by using micropillar array technology [13–15] and quantified as previously described [12]. Micropillar tops were functionalized with fluorescently labeled FN or with LM that was labeled subsequently bu immunostaining. This allowed us to detect deflections with ∼30 nm accuracy corresponding to 500 pN for soft and 2 nN for stiff pillars force precision by using a specifically designed Matlab script.

5.2.6 Preparation of flow channels with encapsulated PDMS micropillar arrays

First, the Si mold with one 10 × 10 mm hexagonal array of 2 µm diameter holes with 2 µm spacing and varying depth, flanked by two 50 µm deep 10×2 mm tranches was passivated with trichloro silane (Sigma). Then a titanium mold with ∼350 µm deep 20 × 20 mm square recess was also passivated with trichloro silane (Sigma). The two molds were brought into contact and fixed against each other (Fig. 5.4a). PDMS 1:10 was poured over SI mold via the one of the two holes in the titanium mold with the help of a pipette (Fig. 5.4b), degassed for 1 hour and

cured for 20 hours at 110°C (Fig. 5.4c). After curing the titanium mold was gently removed (Fig. 5.4d) and PDMS was peeled off the SI mold (Fig. 5.4e). All excess of PDMS was cut off to leave only a 10×10 micropillar array and 50 μm high spacers (Fig. 5.4f). Further, the PDMS micropillar array was divided into two halves along the long side (Fig. 5.4g). From each half of the micropillar array a middle third of spaces was deleted to make sure fluid can pass through (Fig. 5.4h, i). To make sure no flow was present on the side of the PDMS micropillar arrays a small amount of PDMS 1:30 was spread with the help of a pipette inside fluid flow channels of the Ibidi slide (Ibidi, 80608) (Fig. 5.5a). The so prepared micropillar arrays were immediately placed inside the channels and cured for 30' at 60°C (Fig. 5.5b). The two halves of a micropillar array were further functionalized with the help of PDMS 1:30 stamps and FN on top of them. A 40 μl drop of FN mixture in water was incubated for 60' on PDMS 1:30 stamps, then washed and dried in a laminar flow (Fig. 5.5c). The stamps were then gently loaded onto UV-ozone activated PDMS micropillar array halves for 10' (Fig. 5.5d-e). Finally, the flow channels were closed with the help of a #0 coverslip applied to the sticky bottom of the Ibidi slide (Fig. 5.5g). The stamped arrays were subsequently blocked with 0.2% Pluronic (F-127, Sigma) in PBS for 60' at room temperature and washed with PBS.

5.2.7 Seeding cells on top of PDMS micropillar arrays inside flow channels

Before seeding hiPSC line LUMC06iCTRL-derived CD31– (dif31) cells, a Ibidi slide with PDMS micropillar arrays inside was washed with PBS (Fig. 5.6a). Then, Dulbecco's Modified Eagle's Medium (DMEM, Gibco|Thermo Fisher Scientific, USA) supplemented with 10% fetal bovine serum (HyClone, Etten-Leur, The Netherlands), 25 U/ml penicillin and 25 μg/ml streptomycin (Invitrogen/Fisher Scientific) containing 20 000 CD31– cells per sample was injected into each flow channel with the help of a pipette (Fig. 5.6b). Channels were finally closed with a lid provided together with the Ibidi slide (Fig. 5.6c). The slide was further controlled under the microscope for homogeneous cell distribution inside each flow channel, flipped over for the coverslip to face upwards and placed in an incubator for 1 hour for cells to adhere to PDMS micropillars (Fig. 5.6d). After cell attachment the slide was imaged in the INUBGE2E-ZILCS (TokiaHit, Japan) that allows to change CO_2 level

(Fig. 5.6e).

5.3 Results

5.3.1 Pericyte force generation and spreading in starvation, Hypoxia and Ischemia conditions

First we assessed PC force generation and spreading in static, chemically simulated Hypoxia, starvation and Ischemia conditions. Starvation was simulated by incubating PCs in a cell culture media containing low 1 g/l D-glucose. Hypoxia was simulated by treating PCs with 1 mM dimethyloxalylglycine (DMOG), which inhibits prolyl hydroxylases (PHDs) and stabilises HIF-1. Ischemia was simulated by combing DMOG treatment with incubation in a low glucose media.

To investigate an effect of the cell culture media with a low glucose concentration on PC force application we run a starvation experiment. First, PCs were seeded on top of the 47.2 kPa stiff PDMS micropillar arrays and allowed to attach and spread for 7 hours in a full media. Then, cell culture media was replaced with a low glucose media. After 1.5 hours in a low glucose media PCs were fixed and stained for F-actin.

For the simulation of Hypoxia, we first identified the DMOG concentrations that were not cytotoxic for PCs. We evaluated PCs viability for DMOG concentrations of 0.125, 0.5, 1.0, 1.5, 2.0, and 3.0 mM. Our results showed that DMOG concentrations above 1 mM were cytotoxic for PCs. For our further experiments we chose DMOG concentration of 1 mM. Our viability results corroborate findings of earlier studies [16–18].

PCs were incubated for 40 hours in a cell culture medium with 1 mM DMOG to stabilize HIF-1. Then, PCs were detached from the culture dish using PBS and trypsin with 1 mM DMOG concentration to make sure HIF-1 accumulation in the nucleus is not disturbed. Finally, PCs were seeded on top of the 47.2 kPa stiff PDMS micropillar arrays in a cell culture media containing 1 mM DMOG and incubated for 8.5 hours before fixation. After fixation, PCs were immunostained for F-actin.

To test PCs force response in Ischemia conditions PCs were prepared in a similar way as for Hypoxia experiment. They were treated, first, with 1 mM DMOG for 40 hours. Then, seeded on top of the 47.2 kPa stiff PDMS micropillar arrays using PBS and Trypsin with 1 mM DMOG concentration. After 7 hours of incubation in a full cell culture media

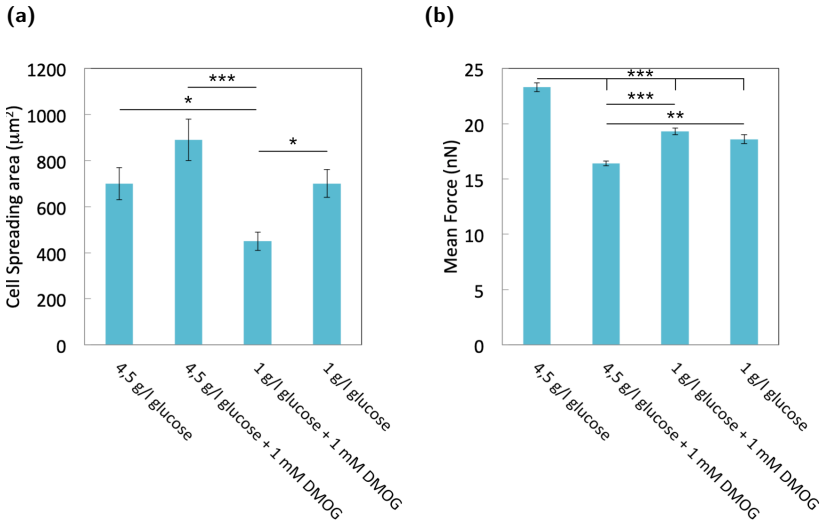


Figure 5.1: Average cell spreading area and force application of PCs. (a) – Average cell spreading area of PCs in normoxia (4.5 g/l glucose), Hypoxia (4.5 g/l glucose + 1 mM DMOG), Ischemia (1 g/l glucose + 1 mM DMOG) and starvation (1 g/l glucose) conditions. (b) – Average fore application of PCs in normoxia, Hypoxia, Ischemia and starvation (1 g/l glucose) conditions. Results are derived from three experiments performed in two replicates. NS, $P>0.05$; *$P<0.05$; **$P<0.005$; ***$P<0.0005$ according to T-test.

containing 1 mM DMOG PC were placed in Ischemia conditions by changing cell culture media to a low 1 g/l D-glucose media containing 1 mM DMOG. Finally, PCs were fixed after 1.5 hours in Ischemia conditions and stained for F-actin.

For control samples PCs were incubated on top of the 47.2 kPa stiff PDMS micropillar arrays in a full cell culture media for 8.5 hours, then fixed and immunostained for F-actin cytoskeleton.

Our results showed an about 20% larger cell spreading area, and an about 30% lower force application of PCs placed in simulated Hypoxia conditions (4.5 g/l glucose + 1 mM DMOG) as compared to the control sample (4.5 g/l glucose) (Fig. 5.1a, 5.1b). After 1.5 hours in Ischemia conditions (1 g/l glucose + 1 mM DMOG) PCs showed the lowest spreading area compared to control, Hypoxia and starvation (1 g/l glucose) samples (Fig. 5.1a). Force application of PCs in Ischemia conditions rapidly increased by $\sim$ 15% compared to PCs in Hypoxia (Fig. 5.1b. Many dead cells were found after 1.5 hours in Ischemia conditions.

In starvation cell spreading area of PCs was comparable to the control sample (Fig. 5.1a), while force application slightly decreased (Fig. 5.1b).

As can be seen from our data, the behavior of PCs changes rapidly (within 1.5 hours) when cells are placed in Ischemia conditions. Unfortunately, Ischemia can't be simulated as an immediate event using the described chemical inhibition method that requires a long pre-treatment with DMOG. Thus, for short-term experiments, that reflects the situation in medical condition, we needeeded to develop another approach that would allow us to constantly monitor the cellular forces, while cells are challenged by deprivation of oxygen and glucose.

5.3.2 Micropillar array technology does not allow fast liquid exchange in the area with cells

The PDMS micropillar array technology developed by us, which permits to study cellular mechanotransduction on a high-resolution microscope, required that micropillar arrays to be flipped upside down to face the objective of a microscope. In this way a precise measurement of cellular forces is achieved [12]. Here we tested whether it was feasible to rapidly change cell culture media located in the 50 μm space between the micropillar arrays and the coverslip in a rapid and reliable manner.

We first analyzed whether the liquid on top of the micropillar arrays could be homogenized by diffusion. Given the size of the arrays, $A = (10 \times 10)mm^2$, and given a typical diffusion constant of $D = 100\ \mu m^2/s$ for a small molecule like a fluorescence dye, it will take, $t = A/(4D) \approx 70\ h$. Hence, a fast medium exchange cannot rely on diffusion.

This prediction was corroborated in experiments. A micropillar array was flipped and fixed against a coverslip of the commercially available dish with a glass bottom. The dish was filled with a PBS solution containing a fluorophore. Under constant monitoring, the PBS solution was replaced with a new – fluorophore-free PBS. The sample was then monitored for a change in the fluorophore signal between pillars and the coverslip. We found that days were required for the new PBS solution to diffuse under the array. This was due to the tiny opening $< 50\ \mu m$ between the micropillars and the coverslip provided by spacers flanking the array and the absence of any fluid flow. Interchange of liquid is solely driven by diffusion.

Thus, it is not possible to rapidly exchange cell culture media surrounding PCs on micropillars and constantly monitor cellular forces in a

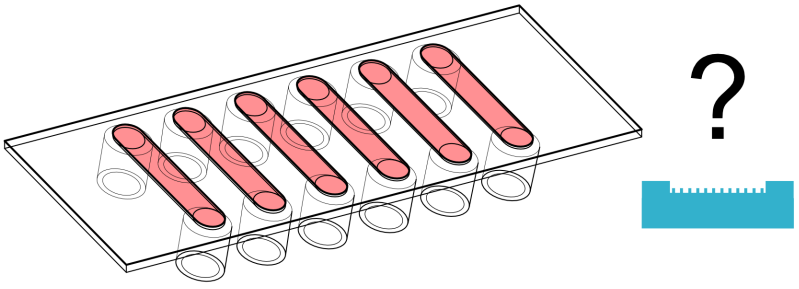


Figure 5.2: Combining micropillar array technology with fluid flow channels would allow to monitor cellular forces and morphology under dynamically changing conditions.

given setup in the envisioned timescale of several minutes. In particular such approach does not fit the requirements of Hypoxia and Ischemia experiments and a new method needed to be developed to permit fast exchange of the cell culture media between micropillars and the coverslip.

5.3.3 Design of a microfluidic channel to track cellular response in rapidly changing conditions

Commercially available slides with fluid flow channels allow cell monitoring under changing conditions, but not cell force measurements. Combining micropillar array technology with fluid flow channels would allow to monitor cellular forces and morphology and simultaneously change cell culture media content. Additionally, micropillar arrays of different stiffness could be used for such experiments (Fig. 5.2). Here we combined two technologies to get a tool that can be used to track fast response of PCs to ischemia conditions *in vitro*.

Requirements

We started by defining requirements for the new design. It had to resemble benefits and functionalities of both techniques. The requirements identified were: (i) the micropillar arrays had to be fitted in a given fluid flow channel, (ii) the design had to allow the fluid to flow in between pillars and a coverslip only, as to make sure that media is effectively replaced in the volume around cells, (iii) the distance from the coverslip

to the pillars had to stay $\sim 50\ \mu m$ to allow high-resolution force measurements, (iv) the fluid flow channel had to allow using #0 coverslips to facilitate imaging with high numerical aperture (NA) objectives.

Design decisions

We chose to use commercially available slides with six fluid flow channels 0.4 mm deep, 17 mm long and 3.8 mm wide, and a self-adhesive side to mount own coverslips. Due to an open design these slides allowed us to put pillars inside and close channels with #0 coverslips to satisfy requirements (i) and (iv).

We decided to cut micropillar arrays in half along the long edge to fill in two channels at a time and keep 50 μm spacers to provide a fixed distance between a coverslip and pillars. This decision was taken to satisfy requirement (iii).

To have a fluid flow between pillars and a coverslip we chose to make an $\sim 1.7\ mm$ opening in the spacers on both sides of a micropillar array. To satisfy requirement (ii) we decided to create an additional mold to prepare micropillar arrays of a fixed thickness corresponding the depth of the prefabricated channels – 0.4 mm.

A schematic drawing of a final design is given in figure 5.3.

5.3.4 Channel preparation

The mold

First, we started to prepare a mold to produce micropillar arrays of a fixed thickness to fit inside fluid flow channels. A new mold had to be applied on top of a silicon wafer containing $10 \times 10\ mm$ hexagonal array of 2 μm diameter holes with 2 μm spacing and varying depth, flanked by two 50 μm deep $10 \times 2\ mm$ tranches – a negative of a PDMS micropillar array. Taking into account the 0.4 mm deep fluid flow channels and the 50 μm high micropillar array spacers the new mold needed to have a 0.35 mm deep recess such that arrays may fit in the channel (Fig. 5.4a). Additionally, the mold had to contain openings to insert PDMS after fixing the mold and a silicon wafer against each other (Fig. 5.4b).

We tested a number of different designs and materials for the mold (Fig. 5.11). Finally, we produced a mold made of a titanium. Titanium is resistant to chloride ions and other chemicals used during PDMS micropillar array production. A square $40 \times 40\ mm$ mold was produced

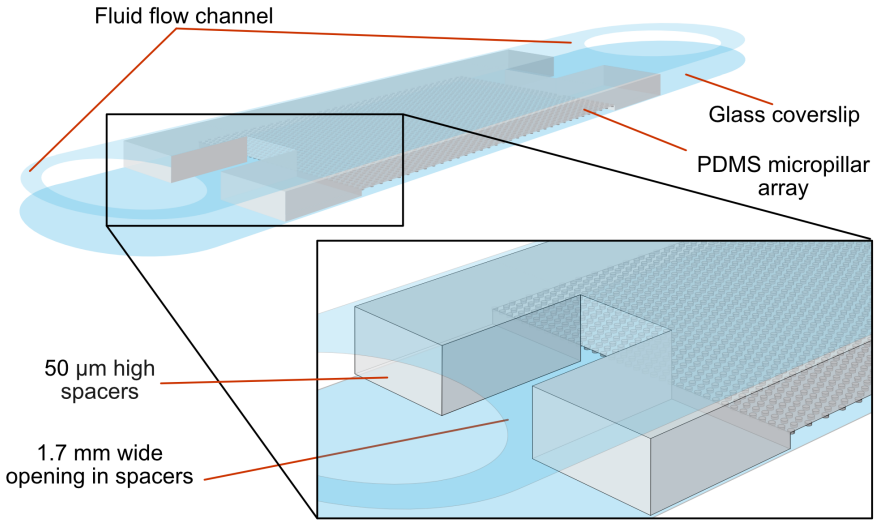


Figure 5.3: A schematic representation of a fluid flow channel design with a micropillar array inside

with a 20×20 mm, 0.35 mm deep recess. The mold was passivated and fixed against a silicon wafer with the clamp. The titanium mold was not prone to deformations or leaks, and yielded PDMS micropillar arrays of a consistent geometry over all experiments (Fig. 5.11d).

PDMS micropillar arrays for fluid flow channels

Subsequently we established the production of PDMS micropillar arrays that met earlier described requirements. Briefly, the titanium mold and the silicon wafer were passivated and brought into contact. The two parts were fixed with a clamp (Fig. 5.4a). PDMS, that was previously degassed, was pressed into one of the two openings of the mold using a pipette (Fig 5.4b). The whole assembly was degassed in a vacuum chamber to avoid air bubbles on top of the wafer. Subsequently the PDMS was cured for 20 hours at 110°C (Fig. 5.4c). The mold was detached from the wafer (Fig. 5.4d), and the PDMS micropillar array was pealed off the silicon wafer (Fig. 5.4e). Excess PDMS was cut off with a sharp blade to leave a 10×10 micropillar array flanked by two 10×2 mm, 50 μm high spacers (Fig. 5.4f). The micropillar array was subsequently divided into two halves along the long side (Fig. 5.4g). The middle

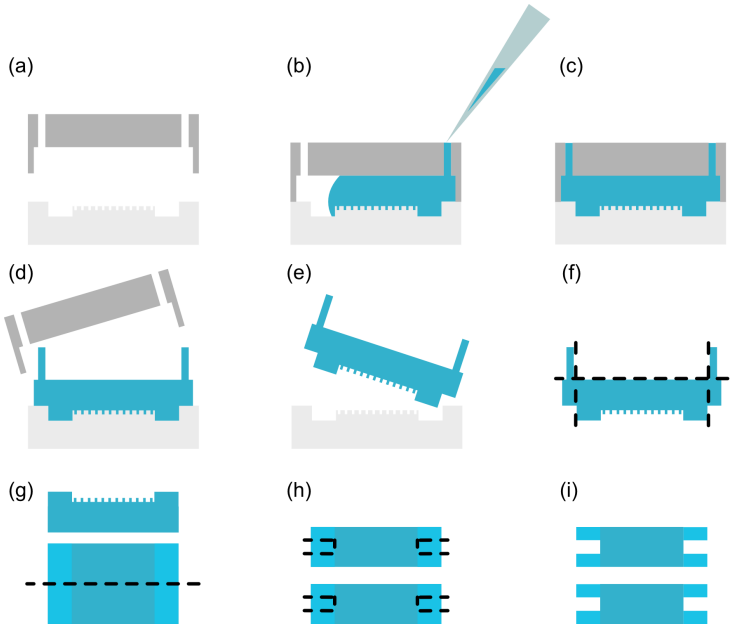


Figure 5.4: A schematic representation of how PDMS micropillar arrays have to be prepared to fit in fluid flow channels. (a) First step is to passivate and fix the mold and a silicon wafer against each other. (b) Second step is to degas PDMS and insert it into the mold. (c) Third step is to degas PDMS in the mold and cure for 20 hours under 110°C. (d, e) Fourth step is to detach the mold from the wafer and pill off the PDMS micropillar array. (f) Fifth step is to cut excess of PDMS and leave only micropillar array with flanking spacers. (g) Sixth step is to divide PDMS micropillar array in two halves. (h, i) Seventh step is to cut off the middle parts from spacers

parts of the spacers $\sim 1.7\ mm$ wide were cut out to allow fluid flow to pass through (Fig. 5.4h, i). In this way two micropillar arrays for two channels were prepared in one step.

Subsequently all parts were assembled and tested. Additional PDMS was added to the bottom of the micropillar arrays to "glue" them inside the channels. For assembly a small amount of PDMS with a 1:30 crosslinker-base ratio was spread inside each channel of the slide (Fig. 5.5a). The PDMS micropillar arrays were placed on top of the spread PDMS. Pressure was applied to the spacers to make sure arrays were properly deepened in the channels (Fig. 5.5b). The slide was further cured at 60°C for 30 minutes. Then, micropillar arrays were functional-

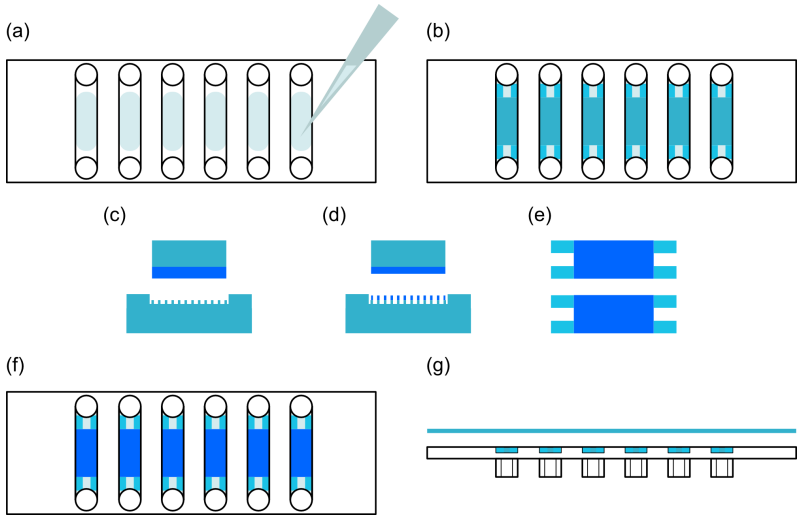


Figure 5.5: A schematic representation of fluid flow channels assembling with micropillar arrays. (a) First step is to spread a small amount of 1:30 PDMS in channels. (b) Second step is to put prepared PDMS micropillar array inside the channels and cure for 30 min at 60°C. (c-f) Third step is to functionalize micropillar arrays with a fluorescently labeled protein of interest. (g) Fourth step is to close channels with a coverslip, passivate micropillar arrays and wash channels with PBS.

ized with the help of PDMS stamps with fluorescently labeled fibronectin on top of them (Fig. 5.5c-f). Finally, channels were closed off with a coverslip (Fig. 5.5g). The whole assembly was passivated and washed with PBS. Tests using colored water showed that the assembly was tight, and that a continous fluid flow could be supported (Fig. 5.12).

Seeding cells on micropillar arrays inside fluid flow channels

Further the work flow for seeding cells on PDMS micropillar arrays inside the closed fluid flow channels was designed but not tested. Channels will be washed with PBS (Fig. 5.6a). Then, approximately 20000 cells will be flushed via the channel entrances into the chamber (Fig. 5.6b). Channels are closed with the lids provided. The distribution of cells on the PDMS micropillar arrays would be analysed using a microscope (Fig. 5.6c). If the cell density is satisfying, the slide with the channels can be flipped over to allow cells to sink to the top of the mi-

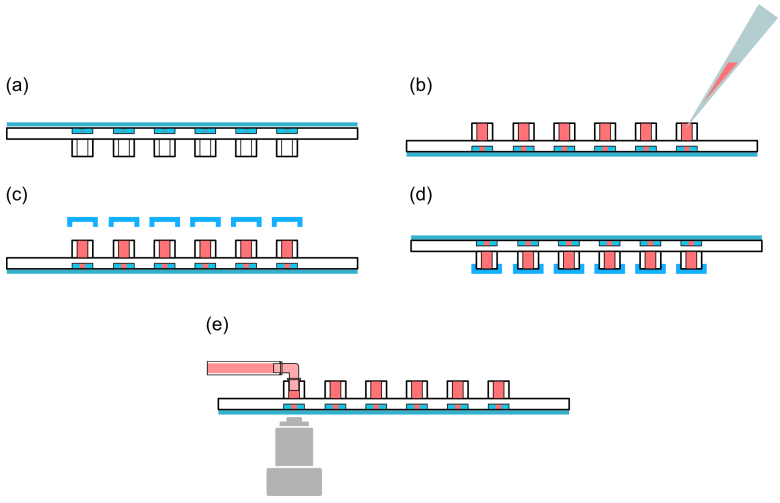


Figure 5.6: A schematic representation of seeding and imaging cells inside fluid flow channels. (a) An earlier prepared slide with PDMS micropillar arrays shall be washed with PBS. (b) A cell culture media containing 20000 cells per sample shall be inserted via channel openings. (c) Fluid flow channels have to be closed with provided lids and cell distribution shall be checked under the microscope (d) The slide has to be inverted to allow cells sink on top of the micropillar arrays. (e) After 1 hour incubation cells can be imaged with a connected fluid flow system

cropillar arrays (Fig. 5.6d). After 1 hour of incubation the slide can be flipped back and imaged under the microscope with a connected fluid flow system (Fig. 5.6e).

5.3.5 Fluid flow in a microchannel with pillars

Finally, we determined the properties of the fluid flow in the channel with micropillar arrays mounted. We required that fluid flow to be laminar, as described by it's Reynolds number. The Reynolds number for the channel was calculated for water at 37 °C in a range of fluid volumetric flow rates (Q) from 0 ml/min to 100 ml/min (Fig. 5.7). The Reynolds number is the ratio between the inertial forces in a fluid and the viscous forces, characterizing the boundary between laminar flow (here desired) and turbulent flow (to be avoided). The Reynolds number, Re is given by [19]:

$$Re = \frac{QD_H\rho}{\mu A}$$

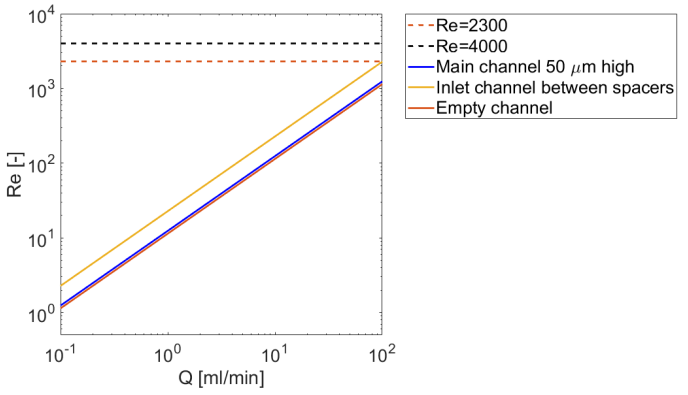


Figure 5.7: Reynolds number in different parts of the channel plotted for water at 37°C over volumetric flow rate.

where Q is the fluid volumetric flow rate, D_H the hydraulic diameter, ρ the density of the fluid, μ the dynamic viscosity, and A the cross sectional area of the channel. For noncircular pipes or channels the hydraulic diameter D_H is given by [19]:

$$D_H = \frac{4A}{P} = \frac{4ab}{2(a+b)} = \frac{2ab}{a+b}$$

where A is the cross sectional area of the channel, P the wetted perimeter, a the hight, and b the width of the channel.

Our calculations showed that fluid flow is laminar in all parts of the channel, given the envisioned flow rates and the design parameter: in the part without micropillar array, in between the spacers, and in the area with the pillars 0 μm high (Fig. 5.7). We performed this analysis for arrays of 3.8 μm (Fig. 5.8a) and 12 μm high pillars (Fig. 5.8b). As can be seen from the graphs, the Reynolds number stays low, hence the flow stays laminar using micropillars of different heights at volumetric flow rates of $0 - 100$ ml/min. At those flow rates the volume below the pillars can be exchanged as fast as 30 ms for the highest flow-rates.

Further, we determined the hydrodynamic entry length of liquid at 37°C inside the channel, i.e. between 0 μm, 3.8 μm and 12 μm high (Fig. 5.9). The entry length describes the distance from the entrance of the channel where the wall shear stress and friction factor reach about 2% of the fully developed value. It therefore describes the spreading of the laminar flow over the full channel diameter after entering a volume. It

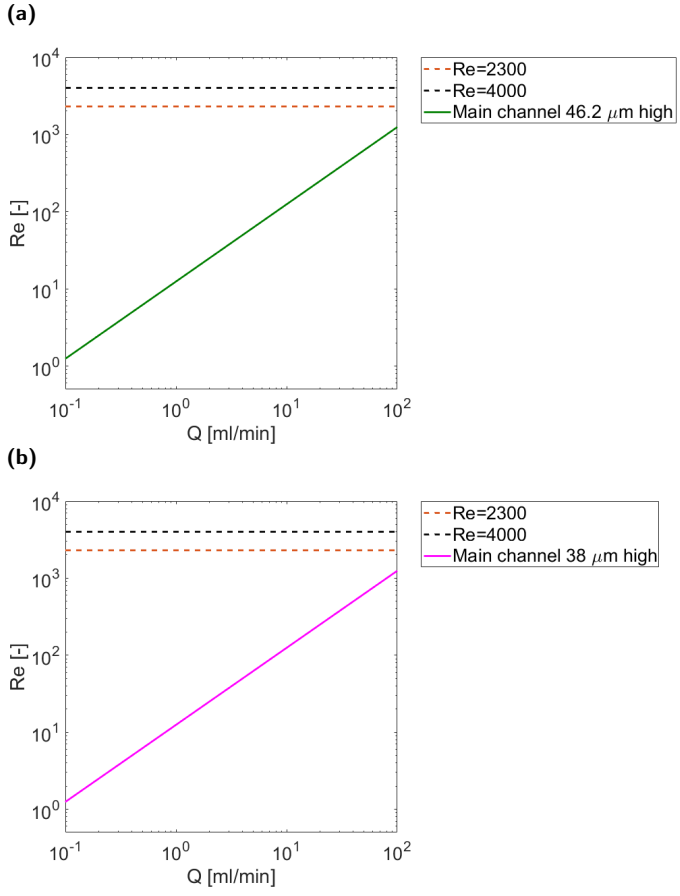


Figure 5.8: Reynolds number for a channel with micropillars (a) 3.8 μm high and (b) 12 μm high plotted over volumetric flow rate

is important for our experiments that the hydrodynamic entry length is small in comparison to the length of the micropillar arrays, being 10 mm. For a laminar flow the hydrodynamic entry length is given by [19]:

$$L_{h,laminar} \cong 0.05\ Re\ D_H$$

The calculations for our channel design shows that entry length will reach half of the channel with micropillars at about 80 ml/min volumetric flow rate and higher (Fig. 5.9).

Finally, we estimated the volumetric flow rate of liquid at 37°C at which the shear stress exerted on the channel wall with pillars will be

in a physiological for cells range – between 0 and 1 Pa [20, 21]. For Newtonian fluids shear stress is expressed as

$$\tau = \mu \frac{dU}{dh}$$

where μ – dynamic viscosity, $\frac{dU}{dh}$ – velocity gradient [19]. Taking into the account that fluid velocity between two plates is

$$\frac{U}{U_{max}} = 1 - (\frac{2h}{H})^2$$

where U_{max} – maximum velocity, which occurs at the centreline, H – channel hight, h – distance from the centreline [19]. Dependency of the shear stress and the volumetric flow rate can be expressed as

$$Q = \frac{AU_{max}}{2} = \frac{ab\tau H^2}{\mu 16h}$$

Our results suggest that shear stress will reach 1 Pa in a channel without pillars at a volumetric flow rate of $\sim 100\ \mu m/min$ (Fig. 5.10). At this flow rate the Reynolds number and the hydrodynamic entry length are negligible for water at 37 °C inside the 50 μm high channel – 1.243 and $6,134\ \mu m$ respectively. Thus, cellular forces can be reliably measured over $\sim 99,87$ % of the micropillar array area.

5.4 Discussion

Currently, the mechanical properties of pericytes (PCs), although of significant importance to their biological function, can only be inferred from (post mortem) *in vivo* imaging. The main reason for this lack of acessibility is the difficulty of generating homogeneous cell culture of primary mid-capillary PCs, as they show differences in phenotype and expression of proteins depending on their location on the capillary tree and don't have unique markers [22–24]. Additionally, "true" or "approved" PCs are located on mid-capillaries that show the most clear differences from smooth muscle cells (SMCs) [1, 22]. PCs located on pre- or post-capillaries have been defined as "transitional" PCs [24]. Thus, generating a cell culture of "true", mid-capillary, primary PCs that don't show expression of α-SMA and support angiogenesis is nearly impossible. As

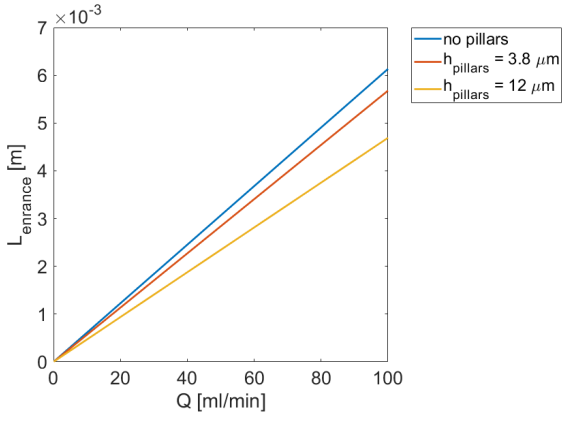


Figure 5.9: Hydrodynamic entry length of water at 37°C inside the channel part with micropillars 0 μm, 3.8 μm and 12 μm high

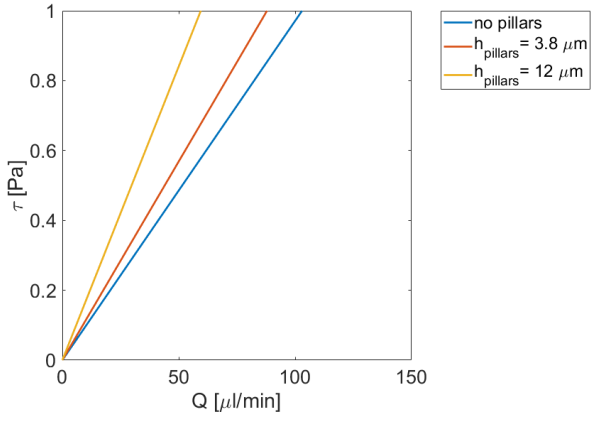


Figure 5.10: Shear stress of water on the wall at 37°C inside the channel part with micropillars 0 μm, 3.8 μm and 12 μm high

a confirmation, there are no such commercially available primary PCs present.

In vivo experiments lack the level of control of experimental conditions and don't support direct cell force measurements in contrast to *in vitro* studies. In the case of PCs it is particularly unfortunate, as their contractility was spotted to be involved, among others, in regulation of capillary diameter, cerebral blood flow or promote brain damage in ischemia [3–5].

Here, we made an attempt to close this gap by using hiPSC-derived PCs that resemble "true" PCs located on mid-capillaries, characterized by lack α-SMA and that support angiogenesis [10, 11]. In combination with PDMS micropillar array technology we performed *in vitro* cell force measurements of PCs in reproducible hypoxia and ischemia conditions. Hypoxic oxygen deprivation was initially simulated with the help of DMOG. By additional subtraction of glucose from the cell culture media we reproduced ischemia conditions.

Our results showed that PCs in starvation condition, retained their morphology and spreading behavior in comparison to the control condition, yet displayed a somewhat lower force application. Thus starvation had only a minor effect on the cell's mechanical properties. Hypoxia was paralleled by an increase of cell spreading and simultaneous significant decrease in cellular force generation. In ischemia cell spreading area decreased significantly, while cellar force application partially recovered.

Those results only in part follow the predicted behavior. As described in literature [3], PCs will constrict and die in ischemic conditions after one hour. Hence, we hypothesized that PCs had a higher force application and a smaller cell spreading area in ischemic condition. While the first expectation was confirmed by our data, the latter does not. We do suspect that this result is due to the way we simulated ischemia which first needed a long incubation step with DMOG leading to hypoxia, followed by the final low-glucose situation. The increase of force exertion compared with hypoxia might be in agreement with this hypothesis.

Our results showed that this method doesn't allow to register fast changes in the behaviour of PCs and mimic ischemia as an immediate event in time. To perform live cell force measurements the in house designed micropillar arrays had to be flipped over [12]. However, our investigation revealed that liquid exchange under the array is not sufficiently fast. Due to the small opening between the coverslip and mi-

cropillars (50 μm) that is required for high resolution measurements of cellular forces the liquid exchange depends only on diffusion.

Therefore, we designed and characterized a new approach that allows us to constantly monitor cellular forces during rapidly exchange of cell culture media to expose cells to different conditions. Our approach combines commercially available fluid flow channels with the in house designed micropillar arrays. The fluid flow properties inside this channel with integrated micropillar array, showed that cellular forces can be reliably measured over $\sim 99,87$ % of the micropillar array area at a physiological for cells shear stress during the liquid exchange.

Taken together, our approach can complement *in vivo* studies on PC behaviour in hypoxia and ischemia conditions and be used for other applications where cell mechanobiology under changing fluid flow or cell media composition is of interest.

5.5 Apendix

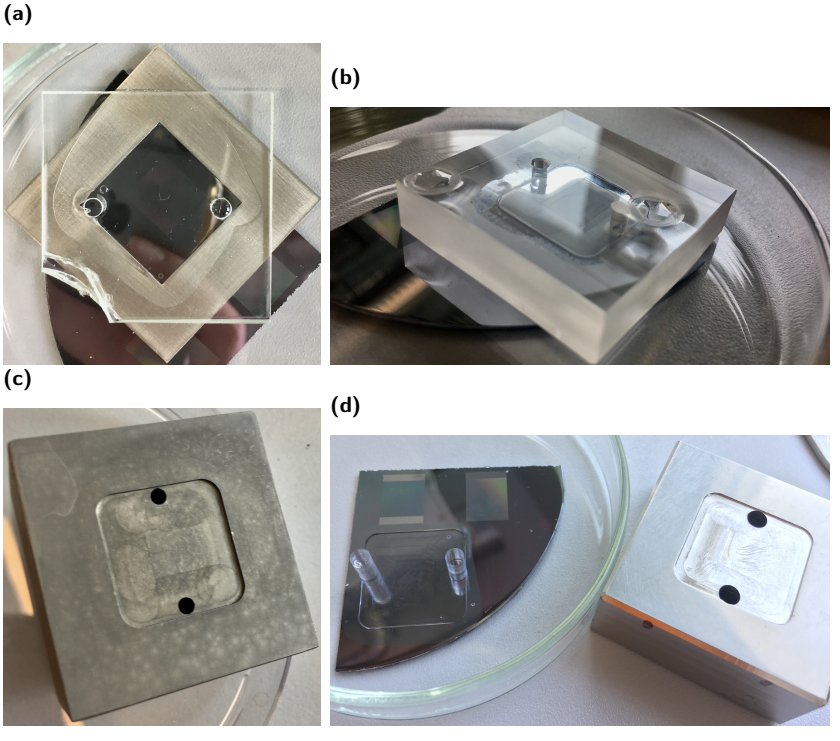


Figure 5.11: Additional molds for PDMS micropillar arrays after testing.(a) Mold made of a combination of glass slide and stainless still frame was prone to PDMS leaks. (b) Mold made of a poly(methyl methacrylate) (PMMA) got deformations after curing at 110°C in places were clamp was attached. (c) Stainless still frame got signs of corrosion after passivation with trichlorosilane. (d) Titanium mold showed overall good results

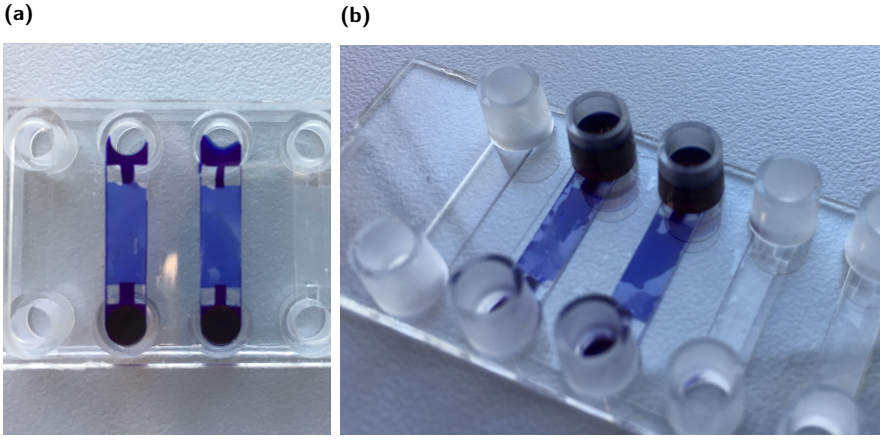


Figure 5.12: Test of the fluid flow channels with PDMS micropillar arrays inside. (a) μQ water coloured with a dye inside fluid flow channels with PDMS micropillar arrays - slide bottom view. (b) Slide top view shows water passing not only between micropillars and a coverslip, but also under the bottom of the micropillar arrays

Bibliography

[1] Annika Armulik, Guillem Genové and Christer Betsholtz. « Pericytes: developmental, physiological, and pathological perspectives, problems, and promises. » In: *Dev. Cell* 21.2 (2011), pp. 193–215. ISSN: 1534-5807.

[2] Bryan L. Krock, Nicolas Skuli and M. Celeste Simon. « Hypoxia-Induced Angiogenesis Good and Evil ». In: *Genes & Cancer* 2.12 (2011), pp. 1117–1133. ISSN: 1947-6019.

[3] Catherine N Hall et al. « Capillary pericytes regulate cerebral blood flow in health and disease. » In: *Nature* 508.7494 (2014), pp. 55–60. ISSN: 0028-0836.

[4] Anusha Mishra et al. « Astrocytes mediate neurovascular signaling to capillary pericytes but not to arterioles. » In: *Nat. Neurosci.* 19.12 (2016), pp. 1619–1627. ISSN: 1097-6256.

[5] Robert A Hill et al. « Regional Blood Flow in the Normal and Ischemic Brain Is Controlled by Arteriolar Smooth Muscle Cell Contractility and Not by Capillary Pericytes. » In: *Neuron* 87.1 (2015), pp. 95–110. ISSN: 0896-6273.

[6] Gregg L. Semenza. « Life with Oxygen ». In: *Science* 318.5847 (2007), pp. 62–64. ISSN: 0036-8075.

[7] Agnieszka Loboda, Alicja Jozkowicz and Jozef Dulak. « HIF-1 versus HIF-2 – Is one more important than the other? » In: *Vascular Pharmacology* 56.5-6 (2012), pp. 245–251. ISSN: 1537-1891.

[8] Frédéric Dayan et al. « Gene regulation in response to graded hypoxia: the non-redundant roles of the oxygen sensors PHD and FIH in the HIF pathway. » In: *Journal of theoretical biology* 259.2 (2009), pp. 304–16. ISSN: 0022-5193.

[9] Theodore Kalogeris et al. « Chapter Six Cell Biology of Ischemia / Reperfusion Injury ». In: *International Review of Cell and Molecular Biology* 298 (2012), pp. 229–317. ISSN: 1937-6448.

[10] Akhilesh Kumar et al. « Specification and Diversification of Pericytes and Smooth Muscle Cells from Mesenchymoangioblasts ». In: *Cell Reports* 19.9 (2017), pp. 1902–1916. ISSN: 2211-1247.

[11] Valeria V Orlova et al. « Functionality of Endothelial Cells and Pericytes From Human Pluripotent Stem Cells Demonstrated in Cultured Vascular Plexus and Zebrafish Xenografts ». In: *Arteriosclerosis Thrombosis Vasc Biology* 34.1 (2014), pp. 177–186. ISSN: 1079-5642.

[12] Hedde van Hoorn et al. « The Nanoscale Architecture of Force-Bearing Focal Adhesions ». In: *Nano letters* 14 (2014), pp. 4257–4262.

[13] Olivia du Roure et al. « Force mapping in epithelial cell migration. » In: *Proc. Natl. Acad. Sci. U.S.A.* 102.7 (2005), pp. 2390–5. ISSN: 0027-8424.

[14] John L Tan et al. « Cells lying on a bed of microneedles: an approach to isolate mechanical force. » In: *Proc. Natl. Acad. Sci. U.S.A.* 100.4 (2003), pp. 1484–9. ISSN: 0027-8424.

[15] Jianping Fu et al. « Mechanical regulation of cell function with geometrically modulated elastomeric substrates. » In: *Nat. Methods* 7.9 (2010), pp. 733–6. ISSN: 1548-7091.

[16] YA Minamishima, J Moslehi and RF Padera. « A feedback loop involving the Phd3 prolyl hydroxylase tunes the mammalian hypoxic response in vivo ». In: (2009).

[17] Alexander Weidemann et al. « HIF-1α activation results in actin cytoskeleton reorganization and modulation of Rac-1 signaling in endothelial cells ». In: *Cell Communication and Signaling* 11.1 (2013), p. 80.

[18] Xian-Bao Liu et al. « Prolyl hydroxylase inhibitor dimethyloxalylglycine enhances mesenchymal stem cell survival ». In: *Journal of Cellular Biochemistry* 106.5 (2009), pp. 903–911. ISSN: 1097-4644.

[19] Yunus A. Çengel and John M. Cimbala. *Fluid Mechanics: Fundamentals and Applications*. English. 4th ed. New York: McGraw-Hill Education, 2017. ISBN: 9781259696534.

[20] James N. Topper and Michael A. Gimbrone Jr. « Blood flow and vascular gene expression: fluid shear stress as a modulator of endothelial phenotype ». In: *Molecular Medicine Today* 5.1 (1999), pp. 40–46. ISSN: 1357-4310.

[21] Cara F Buchanan et al. « Flow shear stress regulates endothelial barrier function and expression of angiogenic factors in a 3D microfluidic tumor vascular model ». In: *Cell Adhesion & Migration* 8.5 (2015), pp. 517–524. ISSN: 1933-6918.

[22] V Nehls and D Drenckhahn. « Heterogeneity of microvascular pericytes for smooth muscle type alpha-actin. » In: *JCB* 113.1 (1991), pp. 147–154. ISSN: 0021-9525.

[23] Roger Grant et al. « Organizational hierarchy and structural diversity of microvascular pericytes in adult mouse cortex ». In: *J Cereb Blood Flow Metabolism* 39.3 (2017), pp. 411–425. ISSN: 0271-678X.

[24] K.W. Zimmermann. « Der feinere bau der blutcapillares ». In: *Z. Anat. Entwickl.* 68 (1923), pp. 3–109.

General Summary and Discussion

Pericytes, the mural cells of blood microvessels, have been described for the first time in 1873 by the French scientist Charles-Marie Benjamin Rouget as a subset of contractile cells surrounding microvessels [1]. In 1923 Zimmerman introduced a new term "pericytes" to connect to their close location to the endothelial cells that form vessel tubes [2]. Pericytes cover the majority of all capillaries and over the years have emerged as important regulators of vascular morphogenesis and function. Despite extensive studies, there are remaining important unsolved questions related to the mechanobiology of pericytes [3] with one of the most intriguing parts of them – the control of the vascular blood flow [4–8].

Currently, the mechanical behaviour of pericytes, although of significant importance to their biological function, can only be inferred from (post mortem) *in vivo* imaging. The main reason for this lack of accessibility is the difficulty of generating homogeneous cell culture of primary mid-capillary pericytes, as they show differences in phenotype and expression of proteins depending on their location on the capillary tree and don't have unique markers [2, 9, 10]. Additionally, "true" or "approved" pericytes are located on mid-capillaries that show the most clear differences from smooth muscle cells [9, 11]. Pericytes located on pre- or post-capillaries have been defined as "transitional" pericytes [2]. Thus, generating a cell culture of "true", mid-capillary, primary pericytes that don't show expression of α-smooth muscle actin (α-SMA) and support angiogenesis is nearly impossible. As a confirmation, there are no such commercially available primary pericytes present. *In vivo* experiments lack the level of control of experimental conditions and don't support direct cell force measurements in contrast to *in vitro* studies.

In this thesis an attempt was made to push boundaries and develop approaches to study pericyte mechanobiology *in vitro*. First, by us-

ing human induced pluripotent stem cell-derived pericytes that resemble "true" pericytes located on mid-capillaries, characterized by the lack of α-smooth muscle actin and supporting angiogenesis [12, 13]. Pericytes have a complicated biochemical and spatial organization of extracellular matrix proteins around them on the capillaries, combined with changing stiffness, accompanying changes in the blood pressure. These factors generally have implications for cell behavior and pericytes are not an exception [14–16]. It is important to combine all these factors in order to accurately reproduce the cell microenvironment *in vitro*. In **chapter 2** the existing knowledge about the structure and properties of the pericyte extracellular matrix have been utilized to identify most appropriate methods to re-create the mechanical microenvironment of pericytes *in vitro* that open new opportunities to study their mechanobiology.

Pericytes are embedded within the capillary basement membrane made of the three main components – collagen IV, laminin-411/511 and fibronectin that are used for attachment of cells in the capillary wall [17–20]. Recent findings revealed that laminin and type IV collagen are not organized into one homogeneous network, but form two layers, allowing fibroblasts to interact with collagen on one side and endothelial cells to interact with laminin on the other side of the basement membrane [21]. Pericytes turned out to be located "under" the collagen layer close to endothelial cells with a thin laminin rich layer in the pericyte-endothelial cell interstitia. Moreover, by electron microscopy it was found that this laminin layer contains small deposits of fibronectin [17, 20, 22]. While endothelial cells attach mainly to laminin, for pericytes this is less well understood. The *in vitro* model of the basement membrane structure in the pericyte-endothelial cell interstitia of the mid-capillary region that I developed allowed to show in **chapter 3** that pericytes prefer fibronectin over the laminin, pointing to a potential role of these fibronectin deposits as main anchoring points for mechanical attachment of pericytes to capillaries. This role was originally proposed by Courtoy in 1983 and now I was able to confirm in an *in vitro* experiment, using the recent advances in the extracellular matrix modeling approaches.

I showed that pericytes respond to the variation in fibronectin-patterned substrate stiffness with changes in force application, spreading, and cell-matrix adhesions size in a not linear manner as, for example, human or mouse fibroblasts, where cellular traction forces together with spreading and cell matrix adhesions size gradually increase with increasing

substrate stiffness [23–25]. Pericytes show optimal spreading and cell-matrix adhesions size on intermediate substrate stiffness and suppressed on both soft and stiff substrates. The forces applied by pericytes do not follow the same trend and are vice versa lower on intermediate substrate stiffness and higher on soft and stiff. The stiffness range supporting optimal pericyte spreading appeared to be close to that for endothelial cells and smooth muscle cells determined by atomic-force microscopy [26, 27], indicating that this stiffness range represents a response in a physiologically relevant stiffness regime. Behavior of pericytes observed in this study gives an insight on the way pericytes distinguish deviations of the microvessel stiffness from the normal tissue and react by increasing contractile forces to provide a mechanical support for microvessel walls, preventing excessive dilation.

As aforementioned, depending on the location along the microvascular tree pericytes have been divided into three subgroups: pre-capillary, mid-capillary and post-capillary pericytes. Mid-capillary pericytes completely lack α-smooth muscle actin, while pre- and post-capillary pericytes show a gradient in the α-smooth muscle actin expression levels from low, next to mid-capillaries, to high closer to arterioles and venules where smooth muscle cells come in place [5, 9, 10]. *In vivo* and *in vitro* studies on pericytes and other cell types show that α-SMA expression is largely affected by soluble factors, but also can be attenuated by mechanical stimuli like substrate stiffness and extracellular matrix. Taking into account that the change of the capillary order is accompanied by the change in it's diameter, inside blood pressure, basement membrane thickness and protein composition, pericytes experience different mechanical signals on different parts of the microvascular tree and this may have an influence on α-SMA protein expression that leads to contractility. Earlier findings already pointed on a special role of extracellular matrix mechanical properties in the α-SMA regulation in myofibroblasts [28] as well as in mesenchymal stem cells [29]. Whether and how do these factors combine to condition α-SMA expression gradient in pericytes in the resting vasculature remains unclear.

In **chapter 4** our *in vitro* approach to study pericyte mechanobiology allowed to investigate whether such parameters like vessel diameter, basement membrane composition and stiffness can have an effect on the α-SMA recruitment to stress fibers in pericytes. An image analysis approach was utilized to obtain uncompromised data on the α-SMA fiber

formation with a single cell resolution. It was observed that pericytes seeded on fibronectin dots surrounded by laminin, showed a lower percentage of α-SMA recruitment to stress fibers than pericytes seeded on a monolayer of fibronectin. The first pattern resembles protein organization in the mid-capillary pericyte-endothelial cell interstitia and the second is more common for arteriole and venule regions of a microvasculature tree. This data suggests an inhibitory effect from the fibronectin organized in patches in the capillary basement membrane on the α-SMA recruitment to the F-actin cytoskeleton of pericytes. Likewise, pericytes showed low to no additional correlation of the α-SMA recruitment with the stiffness or vessel diameter in the presence of fibronectin organized in a dotted pattern. In contrast, human smooth muscle cells maintained the ability to form α-SMA fibers on such a patten and responded to the deviating stiffness and available area for spreading with different α-SMA recruitment rates, yet higher then in pericytes. This data demonstrates that after full maturation of pericytes into smooth muscle cells they loose the ability to adjust α-SMA expression levels in response to the fibronectin arrangement in the basement membrane and become more dependent instead on vessel stiffness and diameter. These findings may further help to unveil processes behind maintaining α-SMA expression gradient in pericytes, and can be used to keep them from obtaining contractile phenotype in cell culture.

The contractility of pericytes, despite some contradictory results, was reported to be involved in regulation of the cerebral blood flow and promote brain damage in ischemia in mice *in vivo* [4, 5, 8]. Nevertheless, there is no direct evidence in terms of direct mechanical measurements. In **chapter 5** a new approach was designed and characterized that allows to constantly monitor cellular forces during a rapid exchange of cell culture media to expose cells to different environmental conditions such as: the temperature, the composition of the cell culture medium, and the oxygen concentration. This approach permits the study of the behaviour of pericytes during hypoxia and ischemia. It also can be applied to any other cells for which the environmental conditions need to be changed, and where responses in cell force application and morphology are questioned.

Taken together, the approaches developed in this thesis to study pericyte behaviour *in vitro* and the obtained results show novel opportunities to investigate pericyte mechanobiology and provide insight, better

understanding and proof to processes that were impossible in *in vivo* experiments.

Bibliography

[1] Charles Rouget. « Memoire sur le developpement, la structure et les proprietes physiologiques des capillaires sanguins ». In: *Archives Physiol Normale Pathol* 5 (1873), pp. 603–61.

[2] K.W. Zimmermann. « Der feinere bau der blutcapillares ». In: *Z. Anat. Entwickl.* 68 (1923), pp. 3–109.

[3] Claire A. Dessalles, Avin Babataheri and Abdul I. Barakat. « Pericyte mechanics and mechanobiology ». In: *Journal of Cell Science* 134.6 (2021), jcs240226. ISSN: 0021-9533.

[4] Catherine N Hall et al. « Capillary pericytes regulate cerebral blood flow in health and disease. » In: *Nature* 508.7494 (2014), pp. 55–60. ISSN: 0028-0836.

[5] Robert A Hill et al. « Regional Blood Flow in the Normal and Ischemic Brain Is Controlled by Arteriolar Smooth Muscle Cell Contractility and Not by Capillary Pericytes. » In: *Neuron* 87.1 (2015), pp. 95–110. ISSN: 0896-6273.

[6] Claire M Peppiatt et al. « Bidirectional control of CNS capillary diameter by pericytes. » In: *Nature* 443.7112 (2006), pp. 700–4. ISSN: 0028-0836.

[7] Nicola B Hamilton, David Attwell and Catherine N Hall. « Pericyte-mediated regulation of capillary diameter: a component of neurovascular coupling in health and disease ». In: *Frontiers in neuroenergetics* 2 (2010).

[8] Anusha Mishra et al. « Astrocytes mediate neurovascular signaling to capillary pericytes but not to arterioles. » In: *Nat. Neurosci.* 19.12 (2016), pp. 1619–1627. ISSN: 1097-6256.

[9] V Nehls and D Drenckhahn. « Heterogeneity of microvascular pericytes for smooth muscle type alpha-actin. » In: *JCB* 113.1 (1991), pp. 147–154. ISSN: 0021-9525.

[10] Roger Grant et al. « Organizational hierarchy and structural diversity of microvascular pericytes in adult mouse cortex ». In: *J Cereb Blood Flow Metabolism* 39.3 (2017), pp. 411–425. ISSN: 0271-678X.

[11] Annika Armulik, Guillem Genové and Christer Betsholtz. « Pericytes: developmental, physiological, and pathological perspectives, problems, and promises. » In: *Dev. Cell* 21.2 (2011), pp. 193–215. ISSN: 1534-5807.

[12] Akhilesh Kumar et al. « Specification and Diversification of Pericytes and Smooth Muscle Cells from Mesenchymoangioblasts ». In: *Cell Reports* 19.9 (2017), pp. 1902–1916. ISSN: 2211-1247.

[13] Valeria V Orlova et al. « Functionality of Endothelial Cells and Pericytes From Human Pluripotent Stem Cells Demonstrated in Cultured Vascular Plexus and Zebrafish Xenografts ». In: *Arteriosclerosis Thrombosis Vasc Biology* 34.1 (2014), pp. 177–186. ISSN: 1079-5642.

[14] Richard O Hynes. « The extracellular matrix: not just pretty fibrils ». In: *Science* 326.5957 (2009), pp. 1216–1219.

[15] Fiona M Watt and Wilhelm TS Huck. « Role of the extracellular matrix in regulating stem cell fate. » In: *Nature Reviews* 14.8 (2013), pp. 467–73. ISSN: 1471-0072.

[16] Christian Frantz, Kathleen M Stewart and Valerie M Weaver. « The extracellular matrix at a glance. » In: *J. Cell. Sci.* 123.Pt 24 (2010), pp. 4195–200. ISSN: 0021-9533.

[17] Annika Armulik, Alexandra Abramsson and Christer Betsholtz. « Endothelial-pericyte interactions. » In: *Circ. Res.* 97.6 (2005), pp. 512–23. ISSN: 0009-7330.

[18] Raghu Kalluri. « Basement membranes: structure, assembly and role in tumour angiogenesis ». In: *Nature Reviews Cancer* 3.6 (2003), pp. 422–433. ISSN: 1474-175X.

[19] Rupert Hallmann et al. « Expression and Function of Laminins in the Embryonic and Mature Vasculature ». In: *Physiol Rev.* 85.3 (2005), pp. 979–1000. ISSN: 0031-9333.

[20] PJ Courtoy and J Boyles. « Fibronectin in the microvasculature: localization in the pericyte-endothelial interstitium. » In: *J. Ultrastruct. Res.* 83.3 (1983), pp. 258–73. ISSN: 0022-5320.

[21] Willi Halfter et al. « The bi-functional organization of human basement membranes. » In: *PLoS ONE* 8.7 (2013), e67660. ISSN: 1932-6203.

[22] Ethan A Winkler, Robert D Bell and Berislav V Zlokovic. « Central nervous system pericytes in health and disease ». In: *Nature Neuroscience* 14.11 (2011), pp. 1398–1405. ISSN: 1097-6256.

[23] Marion Ghibaudo et al. « Traction forces and rigidity sensing regulate cell functions ». In: 4.9 (2008), pp. 1836–1843. ISSN: 1744-683X.

[24] Sangyoon J Han et al. « Decoupling substrate stiffness, spread area, and micropost density: a close spatial relationship between traction forces and focal adhesions. » In: *Biophys. J.* 103.4 (2012), pp. 640–8. ISSN: 0006-3495.

[25] Hedde van Hoorn et al. « The Nanoscale Architecture of Force-Bearing Focal Adhesions ». In: *Nano letters* 14 (2014), pp. 4257–4262.

[26] Takayuki Okamoto et al. « Gap junction-mediated regulation of endothelial cellular stiffness ». In: *Sci Reports* 7.1 (2017), p. 6134. ISSN: 2045-2322.

[27] Zhongkui Hong et al. « Vascular Smooth Muscle Cell Stiffness and Adhesion to Collagen I Modified by Vasoactive Agonists ». In: *Plos One* 10.3 (2015), e0119533.

[28] Jérôme M Goffin et al. « Focal adhesion size controls tension-depen-dent recruitment of α-smooth muscle actin to stress fibers ». In: *JCB* 172.2 (2006). ISSN: 0021-9525.

[29] Nilesh P Talele et al. « Expression of α-Smooth Muscle Actin Determines the Fate of Mesenchymal Stromal Cells ». In: 4.6 (2015), pp. 1016–1030. ISSN: 2213-6711.

Samenvatting

Pericyten, de wandcellen van bloedmicrovaten, werden voor het eerst beschreven in 1873 door de Franse wetenschapper Charles-Marie Benjamin Rouget als een subset van contractiele cellen rondom microvaten [1]. In 1923 introduceerde Zimmerman een nieuwe term "pericyten" om aan te sluiten bij hun ligging dicht bij de endotheelcellen die vaatbuizen vormen [2]. Pericyten bedekken de meerderheid van alle haarvaten en zijn in de loop der jaren naar voren gekomen als belangrijke regulatoren van vasculaire morfogenese en functie. Ondanks uitgebreide studies zijn er nog belangrijke onopgeloste vragen in verband met de mechanobiologie van pericyten [3], waarvan één van de meest intrigerende de controle van de vasculaire bloedstroom is [4–8].

Momenteel kan het mechanische gedrag van pericyten, hoewel van groot belang voor hun biologische functie, alleen worden afgeleid uit (post mortem) beeldvorming. De belangrijkste reden voor dit gebrek aan toegankelijkheid is de moeilijkheid om homogene cellen van primaire mid-capillaire pericyten te genereren, aangezien ze verschillen in fenotype en expressie van eiwitten vertonen die afhankelijk zijn van hun locatie op de capillaire boom, en zij geen unieke markers hebben [2, 9, 10]. Daarnaast bevinden zich "echte" of "goedgekeurde" pericyten op middencapillairen welke de meest duidelijke verschillen met gladde spiercellen vertonen [9, 11]. Pericyten op pre- of post-capillairen zijn gedefinieerd als "transitionele" pericyten [2]. Het genereren van een celcultuur van "echte", midden-capillaire, primaire pericyten die geen expressie van α-gladde spier actine (α-SMA) vertonen en angiogenese ondersteunen is dus vrij-wel onmogelijk. Ter bevestiging, er zijn geen dergelijke, in de handel verkrijgbare, primaire pericyten te koop. *In vivo* experimenten missen de mate van controle over de experimentele omstandigheden en ondersteunen geen directe celkrachtmetingen, in tegenstelling tot *in vitro* studies.

Samenvatting

In dit proefschrift is een poging gedaan om grenzen te verleggen en benaderingen te ontwikkelen om de mechanobiologie van pericyten *in vitro* te bestuderen. Ten eerste, door gebruik te maken van menselijke geïnduceerd pluripotente stamcellen-afgeleide pericyten die lijken op "echte" pericyten in middencapillairen. Deze zijn gekenmerkt door het ontbreken van α-SMA en het ondersteunen van angiogenese [12, 13]. Pericyten hebben een ingewikkelde biochemische en ruimtelijke organisatie van extracellulaire matrix eiwitten op de haarvaten, gecombineerd met veranderende stijfheid, bij veranderingen in de bloeddruk. Deze factoren hebben over het algemeen gevolgen voor het gedrag van de cellen en pericyten vormen daarop geen uitzondering [14–16]. Het is belangrijk om al deze factoren te combineren om de celmicro-omgeving nauwkeurig *in vitro* na te bootsen. In **hoofdstuk 2** is de bestaande kennis over de structuur en eigenschappen van de extracellulaire matrix van pericyten gebruikt om de meest geschikte methoden te identificeren de mechanische micro-omgeving van pericyten *in vitro* na te bootsen. Die ontwikkeling biedt nieuwe mogelijkheden om hun mechanobiologie te bestuderen.

Pericyten zijn ingebed in het capillaire basaalmembraan dat bestaat uit de drie hoofdbestanddelen – collageen IV, laminine-411/511 en fibronectine – die door cellen kunnen worden gebruikt voor hechting in de capillaire wand [17–20]. Recente bevindingen toonden aan dat laminine en type IV collageen niet georganiseerd zijn in één homogeen netwerk, maar twee lagen vormen, waardoor fibroblasten aan de ene kant kunnen interacteren met collageen en endotheelcellen aan de andere kant van het basaalmembraan met laminine [21]. Pericyten bleken zich "onder" de collageenlaag dicht bij endotheelcellen te bevinden met een dunne lamininerijke laag in de pericyte-endotheelcel interstitia. Bovendien bleek met elektronenmicroscopie dat deze lamininelaag kleine eilanden van fibronectine bevat [17, 20, 22]. Terwijl endotheelcellen zich voornamelijk hechten aan laminine, is dit voor pericyten onbekend. Het *in vitro* model van de basaalmembraan in de pericyte-endotheliale celinterstitia van het midden-capillaire gebied dat ik heb ontwikkeld, maakte het mogelijk in **hoofdstuk 3** aan te tonen dat pericyten fibronectine prefereren boven laminine. Dit wijst op een mogelijke rol van deze fibronectine-afzettingen als voornaamste verankeringspunten voor de mechanische hechting van pericyten aan haarvaten. Deze rol werd oorspronkelijk voorgesteld door Courtoy in 1983. Ik heb deze hypothese nu met een *in vitro* experiment kunnen bevestigen, met behulp van de recente vooruitgang in de

modellering van de extracellulaire matrix.

Ik heb verder aangetoond dat pericyten reageren op een variatie in fibronectine patroonstijfheid met veranderingen in kracht, spreiding en cel-matrix adhesie. Dit gebeurt op een niet lineaire wijze zoals bijvoorbeeld in menselijke of muizenfibroblasten waar de cellulaire trekkrachten samen met de cel spreiding en de grootte van cel-matrix adhesie structuren geleidelijk toenemen met toenemende substraatstijfheid [23–25]. Pericyten vertonen optimale spreiding en cel-matrix adhesie grootte op intermediaire substraatstijfheid. De door pericyten uitgeoefende krachten zijn juist omgekeerd lager op intermediaire substraatstijfheid en hoger op heel zachte en heel stijve substraten. Het stijfheidsbereik dat optimale pericytenspreiding ondersteunt, bleek dicht bij dat voor endotheelcellen en gladde spiercellen te liggen [26, 27]. Dit wijst erop dat het gevonden stijfheidsbereik een respons in een fysiologisch relevant stijfheidsregime vertegenwoordigt. Het in deze studie waargenomen gedrag van pericyten geeft inzicht in de manier waarop pericyten afwijkingen van de stijfheid van de microvaten onderscheiden van het normale weefsel, hoe zij reageren door de contractiele krachten te verhogen om een mechanische ondersteuning te bieden aan de wanden van de microvaten, waardoor overmatige dilatatie wordt voorkomen.

Zoals hierboven vermeld zijn pericyten, afhankelijk van de locatie langs de microvasculaire boom, onderverdeeld in drie subgroepen: precapillaire, midden-capillaire en post-capillaire pericyten. Mid-capillaire pericyten missen volledig α-SMA, terwijl pre- en post-capillaire pericyten een gradiënt vertonen in de α-SMA expressie van laag, naast midcapillairen, naar hoog bij arteriolen en venulen waar gladde spiercellen aanwezig zijn [5, 9, 10]. Uit het *in vivo* en *in vitro* onderzoek aan pericyten en andere celtypes blijkt dat de expressie van α-SMA grotendeels wordt beïnvloed door oplosbare factoren, maar ook door mechanische prikkels zoals de stijfheid van het substraat en de extracellulaire matrix. Aangezien de verandering van de volgorde van de capillairen gepaard gaat met veranderingen in diameter, inwendige bloeddruk, dikte van het basaalmembraan en eiwitsamenstelling, ervaren pericyten verschillende mechanische signalen op verschillende delen van de microvasculaire boom. Dit kan invloed hebben op de expressie van α-SMA dat leidt tot contractiliteit. Eerdere bevindingen wezen al op een bijzondere rol van de mechanische eigenschappen van de extracellulaire matrix bij de regulering van α-SMA in myofibroblasten [28] en in mesenchymale stamcellen

[29]. Of en hoe deze factoren bij elkaar genomen de expressiegradiënt van α-SMA in pericyten in de rustende vasculatuur conditioneren blijft onduidelijk.

In **hoofdstuk 4** werd onze *in vitro* benadering van de mechanobiologie van pericyten gebruikt om te onderzoeken of parameters als vaatdiameter, basaal membraansamenstelling en stijfheid een effect kunnen hebben op de rekrutering van α-SMA in spanningsvezels in pericyten. Met behulp van beeldanalyse werden gegevens verkregen over de vorming van α-SMA-vezels met een resolutie van één cel. Er werd geconstateerd dat pericyten die op fibronectinestippen omgeven door laminine groeiden, een lager percentage rekrutering van α-SMA aan spanningsvezels vertoonden dan pericyten die op een monolaag van fibronectine groeiden. Het eerste patroon lijkt op de eiwitorganisatie in de interstitia tussen pericyten en endotheelcellen in het midden van de haarvaten, terwijl het tweede patroon meer voorkomt in arteriole- en venulegebieden van een microvasculatuur boom. Deze gegevens suggereren een remmend effect van het fibronectine dat in patches in het capillaire basaalmembraan is georganiseerd op de rekrutering van α-SMA aan het F-actine cytoskelet van pericyten. Ook vertoonden pericyten weinig tot geen correlatie tussen de rekrutering van α-SMA en de stijfheid of vaatdiameter in aanwezigheid van fibronectine, georganiseerd in een stippelpatroon. Daarentegen behielden menselijke gladde spiercellen het vermogen om α-SMA-vezels te vormen op een dergelijk patroon en reageerden zij op de afwijkende stijfheid en het beschikbare gebied voor verspreiding met verschillende α-SMA-recrutering snelheden, die echter hoger waren dan bij pericyten. Deze gegevens tonen aan dat na volledige rijping van pericyten tot gladde spiercellen zij het vermogen verliezen om het expressieniveau van α-SMA aan te passen in reactie op de fibronectine organisatie in het basaalmembraan en in plaats daarvan meer afhankelijk worden van de stijfheid en de diameter van het bloedvat. Deze bevindingen kunnen verder helpen bij het onderzoeken van de processen achter het handhaven van de α-SMA expressiegradiënt in pericyten en kunnen worden gebruikt om te voorkomen dat zij in celkweek een contractiel fenotype krijgen.

De contractiliteit van pericyten is, ondanks enkele tegenstrijdige resultaten, gerapporteerd als betrokken bij de regulering van de cerebrale bloedstroom en bij hersenschade na ischemie bij muizen *in vivo* [4, 5, 8]. Toch is er geen direct bewijs in termen van directe mechanistische metingen. In **hoofdstuk 5** werd een nieuwe benadering ontworpen en

gekarakteriseerd die het mogelijk maakt om voortdurend de krachten van cellen te monitoren tijdens een snelle uitwisseling van celkweekmedia om cellen bloot te stellen aan verschillende omgevingscondities zoals: de temperatuur, de samenstelling van het celkweekmedium en de zuurstofconcentratie. Met deze aanpak kan het gedrag van pericyten tijdens hypoxie en ischemie worden bestudeerd. De techniek kan ook worden toegepast op alle andere cellen waarvoor de omgevingsomstandigheden moeten worden gewijzigd en waarbij reacties in celkrachttoepassing en morfologie worden gevolgd.

Samengevat, de in dit proefschrift ontwikkelde methodes en benaderingen om het gedrag van pericyten *in vitro* te bestuderen, en de verkregen resultaten, scheppen nieuwe mogelijkheden om de mechanobiologie van pericyten te onderzoeken en inzicht, begrip en bewijs te leveren voor processen die in *in vivo* experimenten onmogelijk waren.

Publications

1. "Fibronectin Patches as Anchoring Points for Force Sensing and Transmission in Human Induced Pluripotent Stem Cell-Derived Pericytes"
   O. Iendaltseva, V.V. Orlova, C.L. Mummery, E.H.J. Danen and T. Schmidt
   Stem Cell Reports (2020)
2. "Insights into the Regulation of α-Smooth Muscle Actin Expression in Pericytes'
   O. Iendaltseva, V.V. Orlova, C.L. Mummery, E.H.J. Danen and T. Schmidt
   in preparation
3. "The mechanical phenotype of Ewing sarcoma cell lines predicts their metastatic niche"
   E. Beletkaia, O. Iendaltseva, H. E. Balcioglu, P.C.W. Hogendoorn, E.H.J. Danen and T. Schmidt
   in preparation
4. "Pericyte Force Generation in *In Vitro* Hypoxia and Ischemia Conditions"
   O. Iendaltseva, V.V. Orlova, C.L. Mummery, E.H.J. Danen and T. Schmidt
   in preparation

Curriculum vitae

Olga Iendaltseva was born on November 18, 1990 in Kharkiv, Ukraine. She did her undergraduate studies at the V. N. Karazin Kharkiv National University specializing in micro- and nanoelectronics and biomedical devices. She performed her pre-diploma and diploma projects at the department of Physical and Biomedical Electronics and Complex Information Technologies under supervision of Prof. dr. N. P. Mustetsov. Within her Bachelor and Master projects she assembled and tested pulmophonography device for automated diagnostics of pneumonia with a low frequency sound. In June 2013, Olga graduated with honors from the V. N. Karazin Kharkiv National University.

In May 2013 she started her 3 months internship under supervision of Prof. dr T. Schmidt and Prof. dr. E. H. J. Danen in Leiden University, The Netherlands. She investigated the effect of diverse substrate stiffnesses on the behaviour of mouse embryonic fibroblasts. In August 2013, Olga continued working in the field of cell mechanobiology as a PhD student in the joint project of Physics of Life Processes and Toxicology groups of Leiden University under supervision of Prof. dr T. Schmidt and Prof. dr. E. H. J. Danen. During her PhD research she focused on studying mechanical behaviour of human induced pluripotent stem cell (hiPSC) – derived pericytes. In order to understand better their reported ability to regulate vascular morphogenesis and capillary diameter she designed different *in vitro* ways to model the mechanical microenvironment of pericytes *in vivo*. She presented results of her work at conferences in the Netherlands, the USA, Spain and the UK. Additionaly, she assisted students with optical tweezers experiments in the course of "Experimental Physics" and guided bachelor projects.

In December 2018, Olga started as industrialization and process engineer in the High Power Drive Laser software controls project at the Development and Engineering department of ASML in Veldhoven. In

January 2021, she became a lead industrialization and process engineer in the High Power Seed module project and in November 2021 started as Machine and Materials Damage Control architect within Machine Conditioning department at ASML.